Alma Mater Studiorum · Università di Bologna

DOTTORATO DI RICERCA IN GEOFISICA
Ciclo XXX

Settore Concorsuale: 02/C1
Settore Scientifico Disciplinare: FIS/06

Retrieval of noise-limited minor atmospheric constituents from satellite emission measurements and determination of atmospheric trends

Presentata da: Massimo Valeri

Coordinatore Dottorato:
Prof.ssa Nadia Pinardi

Supervisore:
Prof. Marco Ridolfi

Tutor:
Dott.ssa Bianca Maria Dinelli

Esame finale anno 2018

Contents

Acronyms

All the acronyms and abbreviations presented throughout this PhD thesis can be found in the following list.

ACE-FTS	Atmospheric Chemistry Experiment – Fourier Transform Spectrometer
AGAGE	Advanced Global Atmospheric Gases Experiment
AILS	Apodised Intrument Line Shape
AK	Averaging Kernel
ASU	Azimuth Scan Unit
ATMOS	Atmospheric Trace MOlecule Spectroscopy
CBA	Calibration Black body Assembly
CCM	Chemistry Climate Model
CCMI	Chemistry Climate Model Initiative
CFC	ChloroFluoroCarbons
DJF	December - January - February
DOF	Degrees Of Freedom
ECD	Electron Capture Detector
ECHAM	European Centre for medium – range weather forecasts – HAMburg
ECMWF	European Centre for Medium – Range Weather Forecast
EMAC	ECHAM / MESSy Atmospheric Chemistry
ENVISAT	ENVIronmental SATellite
ERA	ECMWF Re–Analysis
ESA	European Space Agency
ESRL	Earth System Research Laboratory
ESU	Elevation Scan Unit
FOV	Field Of View
FPS	Focal Plane sub–System

FR	Full Resolution
FWHM	Full Width Half Maximum
GCM	General Circulation Model
GOMOS	Global Ozone Monitoring by Occultation of Stars
GPS	Global Positioning System
HATS	Halocarbons & other Atmospheric Trace Species
HITRAN	HIgh-resolution TRANsmission
HWHM	Half Width Half Maximum
IFOV	Instantaneous Field Of View
IG2	Initial Guess 2
IGAC	International Global Atmospheric Chemistry
IHG	Inter-Hemispheric Gradient
ILS	Instrument Line Shape
JJA	June – July – August
JPL	Jet Propulsion Laboratory
LBL	Line – By – Line
LIDAR	LIght Detection And Ranging
LOS	Line Of Sight
LTE	Local Thermodynamic Equilibrium
LUT	Look–Up Table
MA	Middle Atmosphere
MAM	March – April – May
MECCA	Module Efficiently Calculating the Chemistry of the Atmosphere
MESSy	Modular Earth Submodel System
MIPAS	Michelson Interferometer for Passive Atmospheric Sounding
MIPAS–B	Michelson Interferometer for Passive Atmospheric Sounding – Balloon
MPD	Maximum Path Difference
MSG	METEOSAT Second Generations
MTR	Multi Target Retrieval
MW	MicroWindow
MWMAKE	MicroWindowMAKE
NESR	Noise Equivalent Spectral Radiance
NH	Northern Hemisphere
NOAA	National Oceanic and Atmospheric Administration
NOM	NOMinal
OE	Optimal Estimation
OR	Optimized Resolution
ORM	Optimized Retrieval Model

PSC	Polar Stratospheric Cloud
QBO	Quasi–Biennal Oscillation
QCTM	Quasi Chemistry Transport Model
RADAR	RAdio Detection And Ranging
RMSE	Root Mean Square Error
SCIAMACHY	SCanning Imaging Absorption spectroMeter for Atmospheric CHartographY
SD	Specified Dynamics
SEVIRI	Spinning Enhanced Visible and InfraRed Imager
SH	Southern Hemisphere
SNR	Signal – to – Noise Ratio
SON	September – October – November
SPARC	Stratosphere-troposphere Processes And their Role in Climate
SRF	Solar Radio Flux
TEL	TELescope
UA	Upper Atmosphere
UCI	University of California Irvine
UTLS	Upper Troposphere Lower Stratosphere
UV	UltraViolet
VMR	Volume Mixing Ratio
ZPD	Zero Path Difference

Overview

The Michelson Interferometer for Passive Atmospheric Sounding (MIPAS) is a limb Fourier transform spectrometer that operated onboard the polar-orbiting European Space Agency (ESA) ENVIironmental SATellite (ENVISAT) from July 2002 to April 2012. MIPAS measured atmospheric limb emission in the middle and upper atmosphere (from 6 to 70 km for nominal mode observations) in the spectral range from 4.15 to 14.6 μm (685 - 2410 cm^{-1}). MIPAS spectral range covers almost the complete thermal infrared region in which emission lines of most atmospheric species are present. MIPAS instrument was designed to improve the knowledge of the distribution of the major chemical components, such as *ozone* (O_3), *water vapor* (H_2O), *methane* (CH_4), *nitrous oxide* (N_2O), *nitric acid* (HNO_3) and *nitrogen dioxide* (NO_2), and the dynamics of the middle atmosphere. Furthermore, the polar orbit of ENVISAT and the MIPAS pointing capabilities allow the monitoring of stratospheric O_3 and *chlorofluorocarbons* (CFCs) in the polar regions.

MIPAS measurements were routinely processed by ESA using an online algorithm based on the Optimized Retrieval Model (ORM, [76, 72, 73]). The retrieval was based on the non-linear least squares fit of selected spectral intervals, the so-called MicroWindows (MWs, [19, 104]). The vertical distribution of each geophysical parameter was retrieved simultaneously at all altitudes using the entire MIPAS limb scanning sequence, the so-called global fit approach [9]. The target species were retrieved individually in sequence according to their reciprocal spectral interference. At the beginning of the MIPAS mission, the retrieval sequence included the joint retrieval of pressure and temperature, and the volume mixing ratio (VMR) of the following key atmospheric constituents: H_2O, O_3, HNO_3, CH_4, N_2O and NO_2.

The main target of this PhD thesis is the retrieval and the study of minor constituents of the middle atmosphere using MIPAS measurements. These molecules give a minor contribution to the MIPAS spectra but their retrieval is fundamental to improve the general knowledge of the chemistry of the middle atmosphere. Moreover the retrieval and the study of these minor species allow a better characterization of the already known species due to some possible mutual interferences. Over the years several new molecules, not included in the initial list of retrieved species, have been studied using MIPAS measurements. As a consequence, in the most recent version of MIPAS Level 2 data (Version 7), the list of retrieved molecules has been extended including also *trichlorofluoromethane* (CCl_3F or CFC–11, [45]), *chlorine nitrate* ($ClONO_2$, [40]), *dinitrogen pentoxide* (N_2O_5, [57]), *dichlorodifluoromethane* (CCl_2F_2 or CFC–12, [45]), *carbonyl fluoride* (COF_2, [35]), *carbon tetrachloride* (CCl_4, [100]), *hydrogen cyanide* (HCN, [29]), *carbon tetrafluoride* (CF_4 or CFC–14) and *chlorodifluoromethane* ($CHClF_2$ or HCFC–22, [15]). Other minor atmospheric constituents have been studied but there have not been included in the list of operative products. Some of them are *hydrogen peroxide* (H_2O_2, [63]), *ethane* (C_2H_6, [105]), *formaldehyde* (H_2CO, [94]), *acetylene* (C_2H_2, [64]) and *sulfur dioxide* (SO_2, [38]).

In the first part of this PhD project, we focused on the retrieval of carbonyl chloride ($COCl_2$ or phosgene) and on the study of its distribution in the Upper Troposphere / Lower Stratosphere (UTLS) region [101]. $COCl_2$ is a toxic gas and it was used in the past in the insecticides, pharmaceuticals and herbicides preparation. Due to its high toxicity, its usage has been reduced over the years. In this study $COCl_2$ has been retrieved for the first time using MIPAS measurements and the ORM algorithm with some upgrades needed because of the weak spectral features of the $COCl_2$ and its mutual spectral interference with CFC–11. The main features and the seasonal variations of the $COCl_2$ distribution have been studied and a comparison with Atmospheric Chemistry Experiment – Fourier Transform Spectrometer (ACE-FTS) measurements has been performed.

In the second part of this PhD project, we studied the CCl_4 distribution in the UTLS region using the CCl_4 official ESA Level 2 Version 7 products. CCl_4 is a strong ozone-depleting substance, banned by the Montreal protocol starting from 1996. The interest on this molecule has recently increased as a consequence of the so called "mystery of CCl_4" [93], the

discrepancy between the atmospheric observations and the reported production and consumption. Surface measurements of CCl_4 atmospheric concentrations have demonstrated that its concentration has declined at a rate almost three times smaller than its lifetime-limited rate, suggesting persistent atmospheric emissions despite the ban. We studied the CCl_4 global distribution features and its seasonality. MIPAS CCl_4 measurements have been compared with independent measurements from other satellite (ACE-FTS), balloon-borne remote sounders (MIPAS-Balloon) and data from a Chemistry Climate Model (CCM). MIPAS ESA CCl_4 version 7 product has been produced using the new MIPAS L1B (version 7) which overcome the error caused by the imperfect instrument radiometric calibration using a new time-dependent correction scheme for detector non-linearities. Exploiting this new feature we also evaluated CCl_4 trends as a function of latitude and altitude and compared the results with other satellite trend estimates (ACE-FTS) and other surface global network measurements, as the Advanced Global Atmospheric Gases Experiment (AGAGE, [89, 70, 71]) and the National Oceanic and Atmospheric Administration / Earth System Research Laboratory / Halocarbons & other Atmospheric Trace Species (NOAA / ESRL / HATS, `http://www.esrl.noaa.gov/gmd/hats/`). In order to contribute to the solution of the "mystery of CCl_4", we have also computed the CCl_4 stratospheric lifetime using the tracer-tracer linear correlation approach and compared the results with corresponding results reported in the literature.

The thesis is organized as follows. In Chap. 1 we introduce the main properties of the Earth's atmosphere and the method used to study them. In Chap. 2 we present the main characteristics of the MIPAS instrument. The principal concepts of the radiative transfer model are presented in Chap. 3. In Chap. 4 we discuss the so-called inverse problem and we introduce the main features of the ORM algorithm. The retrieval of $COCl_2$ and the study of its distribution are discussed in Chap. 5. The study of CCl_4 distribution, its properties, trends and lifetime are described in Chap. 6. The conclusions are finally drawn in Chap. 7.

Chapter 1

Observation of the Earth's atmosphere

The atmosphere (from the Greek: *atmos* = vapor and *sphaira* = sphere) is defined as the layer of gas that surrounds a planet. Over the years, a wide variety of apparatus has been used to observe and study atmospheric properties. In order to deeply understand the atmospheric system, we need to obtain useful information regarding its state and evolution with extremely high temporal and spatial resolution and as continuously as possible. Unfortunately this is not completely possible and there is no unique instrument, technique or method of investigation able to provide a complete description of the atmosphere in all its dimensions. The synergy of different, but at the same time complementary, techniques is therefore essential. Here we present the main features of the Earth's atmosphere and the most important techniques used to study its properties.

1.1 Composition and vertical structure of the Earth's atmosphere

The major chemical components of the Earth's atmosphere are molecular *nitrogen* (N_2, 78.1%) and molecular *oxygen* (O_2, 20.9%). These two gases, together with the noble gases, are well mixed below the altitude of approximately 100 km (*omosphere*) due to their long lifetime. The remaining atmospheric volume (less than 1%) is made by the so-called "minor" constituents, such as H_2O, O_3, *carbon dioxide* (CO_2), *carbon monoxide* (CO), CH_4, N_2O, and over twenty "trace" species. Beside all these molecules, the Earth's atmosphere contains also liquid (water droplets) and solid particles (aerosols and ice crystals) whose distribution is highly variable both in space and time. These particles represent only a small part of the total composition of the atmosphere but they play a key role in the absorption and scattering of the solar radiation and in the physics of clouds and precipitation.

Most of the atmospheric constituents are well mixed even if, in general, the atmosphere shows an heterogeneous vertical structure with variations in chemical composition, pressure (density) and temperature. Neglecting sources and sinks, the concentration of the atmospheric constituents can be determined by mixing due to fluid motion and molecular diffusion. The first mechanism is dominant at low altitudes, where the molecular mean free path is relatively small and the molecular diffusion time-scale is many orders of magnitude greater than the turbulence time-scale. By contrast, molecular diffusion becomes predominant in the higher layers of the atmosphere, where the mean free path increases due to the lower density, stratifying the atmosphere as a function of the molecular weight.

As for the chemical composition, the atmospheric pressure varies as a function of the altitude. The vertical distribution of the pressure results from the competition between the molecular kinetic energy and the gravity

$$p = p_{surface} \cdot e^{(-\frac{mgz}{k_B T})} \tag{1.1}$$

where $p_{surface}$ is the pressure at the Earth's surface, m is the mean atmospheric molecular weight, g is the gravitational acceleration, z is the height, k_B is the Boltzmann constant and T is the temperature. Considering that on average $k_B T/mg$ is equal to 7 km, the atmospheric pressure decreases

exponentially with height by a factor 2.7 (e^{-1}) every 7 km.

The temperature distribution in the atmosphere varies both vertically and horizontally. However, the vertical distribution of temperature is qualitatively similar over the whole globe. For this reason the most common classification of the Earth's atmosphere is based on the vertical behaviour of the temperature. The different vertical layers are classified on the basis of the different vertical temperature gradients ($-dT/dz$, also known as *lapse rate*). The thickness and the boundaries of these layers can vary as function of time and location. As an example we report in Fig. 1.1, the U.S. Standard Atmosphere at mid-latitude. As shown in Fig. 1.1 the atmosphere results neatly divided into four layers: *troposphere, stratosphere, mesosphere* and *thermosphere*. These layers are characterized by substantially different chemical and physical processes. The interfaces between the layers are defined as the altitude where the sign of the temperature gradients changes, and they are respectively called *tropopause, stratopause, mesopause* and *thermopause*.

The structure of the temperature profile is related with the dominant processes occurring in the specific sphere. Large part of the radiation emitted by the Sun is in the visible portion of the electromagnetic spectrum. The Earth's atmosphere does not strongly absorb this radiation and therefore large part of the radiation can reach the ground where it is absorbed. The presence of clouds, that are able to reflect back to space part of the radiation, reduces the fraction of energy that reaches the surface. The Earth's surface is heated by the incoming solar radiation, and radiates the absorbed energy as a black-body. Lower atmosphere is heated by the ground causing convection and a decrease in temperature with height due to volume expansion. Several species, such as H_2O, CH_4 and CO_2 (known as *green house gases*), are able to absorb and re-emit part of the outgoing terrestrial radiation in the infrared region, originating the so-called *green house effect*.

The troposphere is the lowermost layer of the atmosphere, directly in contact with the surface. The altitude of the top of the troposphere, the tropopause, varies as a function of the latitude: it is approximately 18 km over the tropics, 12 km at mid-latitudes and from 6 to 8 km at the poles. The mean temperature decreases from the surface up to the tropopause with a typical lapse rate of $6.5°C/km$. Most of the weather phenomena (i.e. storms, clouds, precipitations) take place in this layer basically for two reasons. The

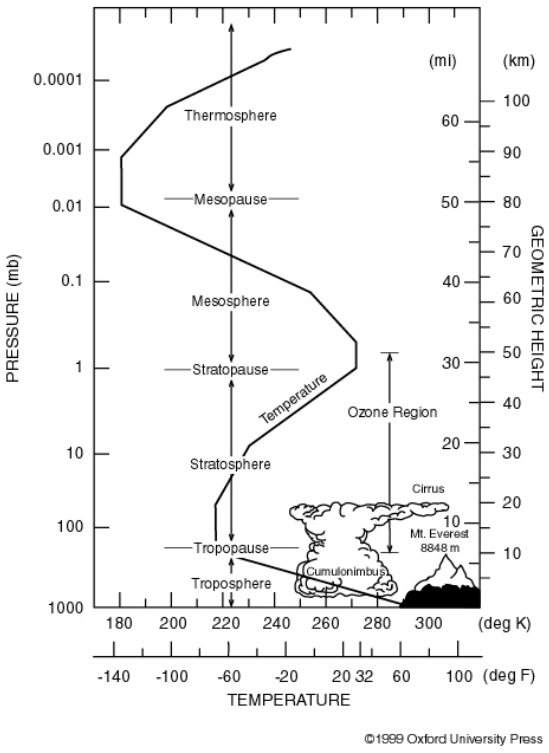

Figure 1.1: Vertical distribution of temperature between the surface and 100 km altitude as defined by the U.S. Standard Atmosphere 1976 model for mid-latitude conditions. The vertical distribution of pressure is shown in the left vertical axis. The nomenclature of the atmospheric regions and corresponding *pause* are shown.

first cause is the strong instability that characterizes the troposphere, due to its vertical thermal structure, that allows significant vertical exchanges of energy and mass. The second one is that this layer contains about 90% of the total atmospheric mass and almost all of the atmospheric water vapor.

In the stratosphere, the layer between the tropopause and about 50 km (the stratopause), the temperature increases with altitude due to ozone and molecular oxygen absorption of the ultraviolet solar radiation [13]. The stratosphere contains approximately 90% of the total atmospheric ozone, with a peak at about 35 km (Fig. 1.2). The *ozone layer* absorbs the largest part of the solar ultraviolet radiation [13]. This process has been fundamental for the development of the life on the Earth reducing the amount of harmful UV radiation that reaches the Earth's surface and contributing to

the maintenance of the Earth heat balance. Because of the negative lapse rate, this atmospheric region is characterized by very stable conditions: vertical motions are inhibited, radiative processes play a dominant role and vertical mass exchanges between the stratosphere and the troposphere are somewhat rare.

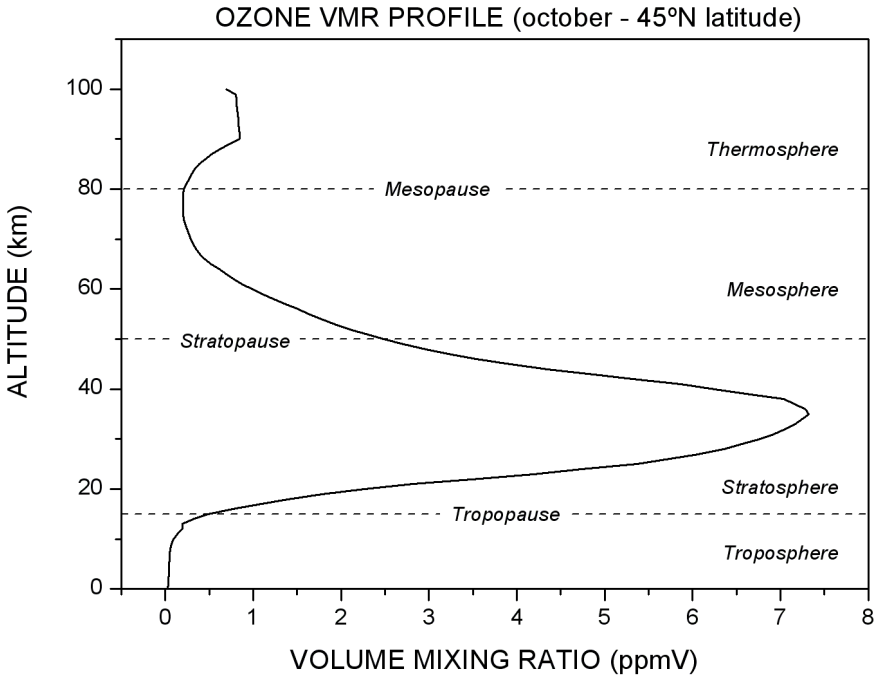

Figure 1.2: Vertical distribution of ozone between the surface and 100 km altitude as given by the IG2 climatology for mid-latitude conditions [74].

In the mesosphere, the layer within about 50 and 90 km, the temperature decreases with altitude with a lapse rate of about $2°C/km$. As in the troposphere, due to the positive lapse rate, dynamical instability and convection characterize this atmospheric region. Ozone concentration in this region is relatively low (Fig. 1.2) and most of the chemical species are in an excited state absorbing ultraviolet radiation from the Sun.

In the outermost layer, the thermosphere, the temperature rises once again strongly depending on the solar activity. In this layer, UV radiation photo-dissociates molecular oxygen and molecular nitrogen into atoms and ions. Dynamical mixing and vertical exchanges become negligible and the

molecular diffusion becomes the dominant process, producing separation of species according to their molecular or atomic weight.

1.2 Observation platforms and geometries

Fig. 1.3 gives a exhaustive representation of the methods, the modes and the geometries presented in this section and, at the same time, gives an idea of the current variety of possibilities to observe the atmosphere.

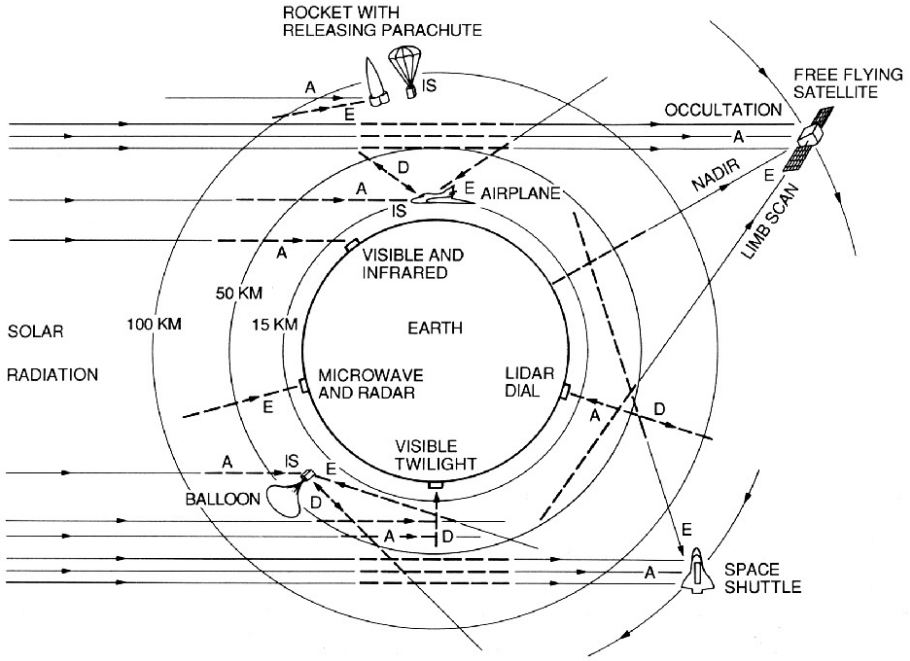

Figure 1.3: Schematic representation of the different platforms (ground based, balloon, rocket and satellite), techniques (letters *A*, *E*, and *D* refer to respectively Absorption-, Emission-, and Diffusion-methods) and observation geometries (limb, zenith and nadir sounding). The acronym *IS* stands for *in situ* and it indicates that also *in situ* studies can be performed.

The first general distinction between the different observation methods can be made on the basis of the location of the instrument with respect the atmospheric regions under investigation. We refer to *in situ* investigations when the instrument is directly into the region where the measurements are performed. By contrast, if the instrument is located at a certain distance from the atmospheric region to be studied we refer to *remote sensing* tech-

niques. The most important advantages of remote sensing techniques with respect to in-situ methods are that they can sound larger atmospheric region and they do not perturb the local state of the region under investigation. For these reasons the remote sensing techniques, especially from space, are the most used solution to achieve global datasets. At the same time remote sensing methods have some limitations in both spatial resolution and short term variability. For this reason the in situ measurements, with their high accuracy are important for more specific and detailed studies and for validation purposes, especially regarding remote sensing missions. Also the in situ methods are suitable for the determination of profiles of gas concentrations as a function of altitude, but they require the positioning of the instrument on mobile platforms, such as airplanes and balloons.

The configuration of the atmospheric measurement can be defined considering also the location of the instrument. Here we describe the most used platforms and their major features, advantages and disadvantages.

Ground based instruments are easily maintainable and they provide long, stable and accurate time series. The spatial coverage is generally poor, depending on the dimension of the network, and the instruments are very sensitive to all the phenomena that occur in the troposphere (clouds, turbulence, and so on).

Balloon instruments are used to profile atmospheric parameters with extremely high vertical resolution up to 35–40 km. The flight track can not be remotely controlled. As for ground based instruments, the geographical coverage is quite poor.

Aircrafts can host onboard several instruments. Compared to the balloons instruments, they are used for controlled flights up to 20 km following different trajectories, and they can provide better coverage with relatively higher spatial resolution. Aircrafts are very helpful for validation of satellite missions and for the analysis of specific events.

Satellites can provide global coverage observations. They can be divided into geo-stationary, polar and equatorial. The first ones are located on an equatorial orbit at an altitude of about 36,000 km, so that the satellite rotates at the same speed of the Earth revolution. Because of this they allow continuous measurements of the same location with extremely high temporal resolution. However they can efficiently monitor only the region between 60° North and South. Polar satellites, that are located on a lower

orbit (600–850 km) sun synchronous and on a plane containing both the Earth's poles, allow near global coverage (up to the polar latitudes) but with a very low time resolution. Typically polar orbiting satellites cross the equator always at the same time and the revisit time of a given geolocation is about 28 days. Equatorial satellites are located at about 300 km on an orbit plane at a small angle with the equatorial plane, they allow a global coverage of the latitudinal regions close to the equator, with a higher time resolution of the polar satellites. Beside the time resolution, one of the disadvantages of the usage of satellites to monitor the atmosphere is their relatively short lifetime (some years) that allows only short time series. A solution could be multi–satellite missions that provide better spatial and temporal coverage and longer time series even if they introduce inter–calibration issues.

Atmospheric measurements classification can be made according the geometry used for the observation, that is the angle between the line of sight (LOS) of the instrument and the vertical to the Earth's surface.

When the LOS is oriented in the vertical direction, we speak of vertical sounding. Vertical sounding can be either in the *zenith* or in the *nadir* directions. The *zenith* soundings imply that the atmosphere is observed from the surface of the Earth, or generally at low altitudes and the instruments looks toward the deep space from below. Since the lowest atmospheric layers are denser and warmer, to reduce the contamination due to water vapor, turbulence, and so on, the instrument can be located on high mountains or on dry sites. In the *nadir* soundings, the instrument is located high up in the atmosphere and looks down to the Earth. *Nadir* observations can be made from satellite, aircrafts and stratospheric balloons. In *nadir* soundings the LOS of the instrument always encounters the surface of the Earth. When the instrument is located at high altitudes and the LOS is oriented so that the Earth's surface never reached, we speak of limb sounding measurements. In this case the measured signal is originated only from the atmospheric layers encountered by the LOS itself. Limb sounders can be located onboard high altitude platforms, such as stratospheric balloons, aircrafts and satellites.

Vertical sounding techniques are characterized by very high geo-spatial resolution and can provide integrated (along the vertical direction) information or, exploiting the pressure dependence of the observed atmospheric spectral features, information as a function of the altitude. Because of the long path of the LOS in the atmosphere, limb sounding techniques have a

relatively high signal-to-noise ratio (SNR) with respect to the vertical sounding and, observing the atmosphere at different zenith angles, they provide vertical distribution of the atmospheric parameters with high vertical resolution. However their geo-spatial resolution is lower with respect to the vertical sounding techniques considering that the major contribution to the measured signal comes from the layer close to the *tangent point* (minimum distance of the optical path from the Earth's surface) where the optical path of the LOS is very long.

1.3 Emission and absorption measurements

Another general classification of atmospheric measurements is related to the type of sensor used (*active* or *passive*). Active sensors propagate their own-produced electromagnetic radiation toward the target to be investigated, such as an atmospheric region, and measure the intensity and the properties of the back-signal. Passive sensors measure the natural atmospheric emission or the interaction of the atmosphere with naturally generated radiation (absorption or diffusion). LIDAR (LIght Detection And Ranging), RADAR (RAdio Detection and Ranging) and GPS (Global Positioning System) are some examples of active systems. An example of passive sensor is the Spinning Enhanced Visible and Infrared Imager (SEVIRI) onboard the METEOSAT Second Generation (MSG) spacecraft. Here we focus on the passive sensors and we briefly describes how the measured radiance is generated.

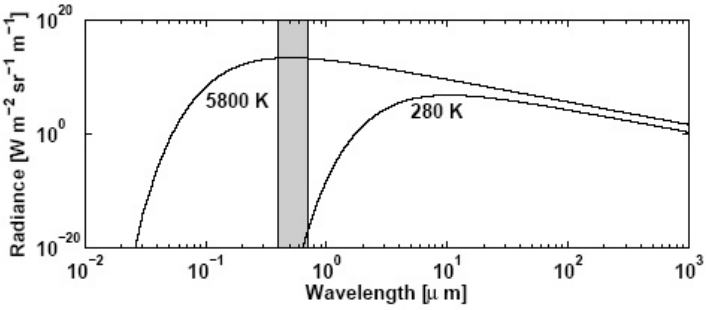

Figure 1.4: Sun (5800 K) and Earth (280 K) black-body distributions. The visible region (0.4–0.7 μm) is shaded in grey.

The Earth and the Sun can be approximately treated as black-bodies,

with typical temperatures of 280 K (250 K considering the Earth–atmosphere system) and 5800 K respectively. As shown in Fig. 1.4 the black-body curve of the Sun peaks at about 0.50 μm and exceeds the Earth's emission curve at all wavelengths. The Earth black-body signal is weaker than the solar one and the wavelength of its intensity peak is at longer wavelengths, at about 10 μm.

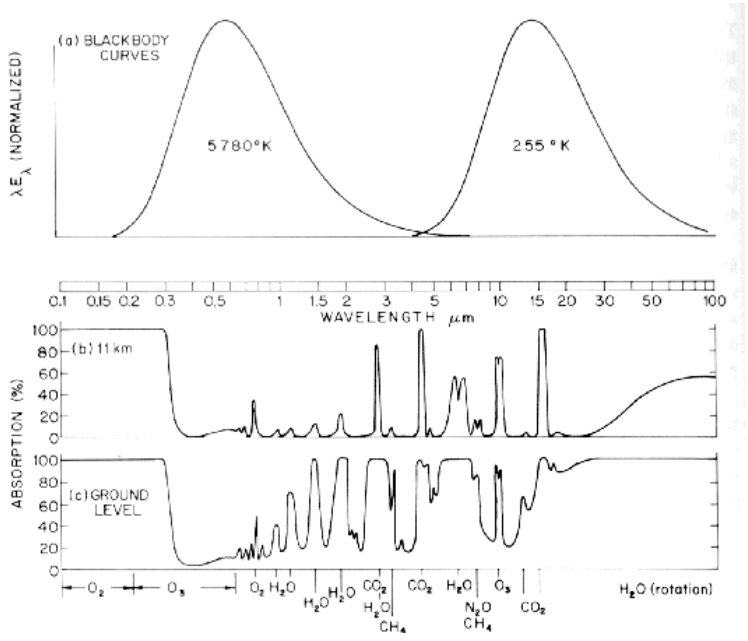

Figure 1.5: Sun ($\sim$ 5800 K) and Earth–Atmosphere system ($\sim$ 250 K) normalized (dividing each curve by its maximum value) black-body distributions (upper panel) and atmospheric attenuation at 11 km (middle panel) and at ground level (lower panel) as function of wavelength. The major absorbing species are also reported in the lower panels. From `https://www.atmos.washington.edu/`.

Nevertheless dividing both curves by their maximum value, we obtain the normalized blackbody curves (upper panel of Fig. 1.5) and only a minor overlap (at about 4 μm) is evident. Therefore we can study the spectrum of the Earth's atmosphere exploiting different processes as a function of the wavelength. Earth black-body emits radiation at wavelengths longer than 4 μm and is usually studied through emission processes, while measurements performed at wavelengths shorter than 4 μm usually exploit the radiation originated from the Sun (or other warm sources like stars) and usually exploit both absorption and scattering processes. Absorption methods have

the main advantage of using a bright source, such as the Sun, providing spectra with high SNR. On the other hand the observations are bounded to the presence of the source in the LOS of the instrument and are possible only at certain times. This aspect can create difficulties thinking about species with day/night variations. The only restriction of emission methods is that the direct source of radiation has usually to be avoided, but measurements can be made at all times and therefore can provide information both day and night and on of time varying species. The atmosphere is a relatively weak source of radiation thus the SNR is in general lower with respect to the absorption techniques. Since the SNR ratio is proportional to the square root of the measurement time, the emission techniques adopt relatively longer measurement time in order to enhance the ratio.

In Fig. 1.5 we can also observe the attenuation of the atmosphere as a function of the wavelength at 11 km (middle panel Fig. 1.5) and at the ground level (lower panel Fig. 1.5). For both altitudes, the atmospheric attenuation is high below 3 μm (about 100 %) and above 20 μm. Within these wavelengths the atmosphere is more transparent and we can observe spectral structures caused by the absorbing species.

Chapter 2

Michelson Interferometer for Passive Atmospheric Sounding

The Michelson Interferometer for Passive Atmopsheric Sounding (MIPAS) is a limb Fourier transform spectrometer that operated onboard the European Space Agency (ESA) polar-orbiting ENVIironmental SATellite (ENVISAT) from July 2002 to April 2012. ENVISAT was a polar-orbiting Earth observation satellite launched on 1 March 2002. Its payload consists of a set of ten instruments that operate over a wide range of the electromagnetic spectrum, from centimeter waves to the ultraviolet. Together with Global Ozone Monitoring by Occultation of Stars (GOMOS) and SCanning Imaging Absorption spectroMeter for Atmospheric CHartographY (SCIAMACHY) MIPAS was one of the three atmospheric chemistry sensors. Full details about MIPAS instrument and mission can be found in [25, 73, 22]

2.1 Mission overview

MIPAS measured the atmospheric limb emission in the middle and upper atmosphere (from 6 to 70 km for nominal mode observations) in the spectral range from 685 to 2410 cm^{-1}(from 14.6 to 4.15 μm). MIPAS spectral range covers almost the complete thermal infrared region in which emission lines of most atmospheric species are present. The primary scientific aims of the MIPAS instrument [25] were:

- an improvement of the knowledge about the chemical composition and dynamics of the middle atmosphere;
- near-real-time, global geophysical measurements of the middle atmosphere components (in particular O_3, H_2O, CH_4, N_2O, HNO_3 and NO_2);
- monitoring of stratospheric O_3 and CFCs.

In the first part of the mission (from July 2002 to March 2004), MIPAS measured, nearly continuously, using the full spectral resolution (FR, 0.025 cm^{-1}). On 26 March 2004, MIPAS operations were interrupted due to an anomaly in the interferometer drive unit. After a detailed analysis of the instrument performances, the mission restarted (9 January 2005) using a shorter interferometric sweep, corresponding to a lower spectral resolution (0.0625 cm^{-1}) and a shorter measurement time. This reduction in the measurement time was exploited to increase, with respect to the first part of the mission, the frequency of the observations both in the altitude and in the horizontal domain (along the orbit). These changes provide an optimized compromise between spectral and spatial resolutions (optimized resolution, OR). MIPAS was operated up to 8 April 2012, when an ENVISAT failure occurred resulting into the loss of communication between ground and the satellite.

The polar orbit of ENVISAT and the MIPAS pointing capabilities allow a global geographical coverage, including the polar regions. The instrument performs measurements in two pointing modes: *sideways* and *rear-ward* (Fig. 2.1). The sideways viewing, across the orbit plane, was used for the study of specific events or atmospheric phenomena (volcano eruptions or trace-gas concentrations above major air traffic routes), whereas the rear-ward viewing was used for routine measurements.

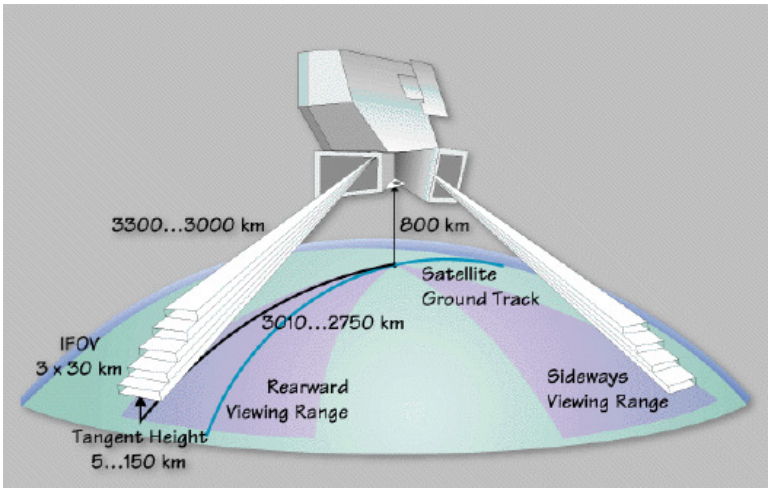

Figure 2.1: Representation of MIPAS observation geometries and main features.

2.2 Measurement principles

The heart of MIPAS is a Fourier transform interferometer offering the possibility to measure infrared emission spectra of the atmosphere with a wide spectral range and an extremely high spectral resolution. The interferometer provides several advantages over the conventional grating spectrometer. In the interferometer the radiation of the full spectrum reaches the detectors for the entire duration of the interferometric sweep (multiplex or Fellgett advantage, [24]). By contrast, a grating spectrometer has to use scanning devices and/or dispersive elements to send the individual spectral elements sequentially to the detector. Another advantage of the Fourier Transform interferometers is that a single detector records a broadband spectrum with high spectral resolution, while for dispersive spectrometers a large array of detectors must be employed. For the same resolution, the energy throughput in an interferometer is higher than in a conventional grating spectrometer, where it is limited by the slits. This throughput (or Jaquinot, [42]) advantage is caused by the circular symmetry of the interferometer. The combination of the throughput and the multiplex advantage leads the ability of the Fourier Transform interferometer to achieve the same SNR as a conventional spectrometer in a much shorter time. The main disadvantage of the interferometer is represented by the high mechanical complexity of

this due to the fact that the output has to be sampled at regular intervals along the optical path.

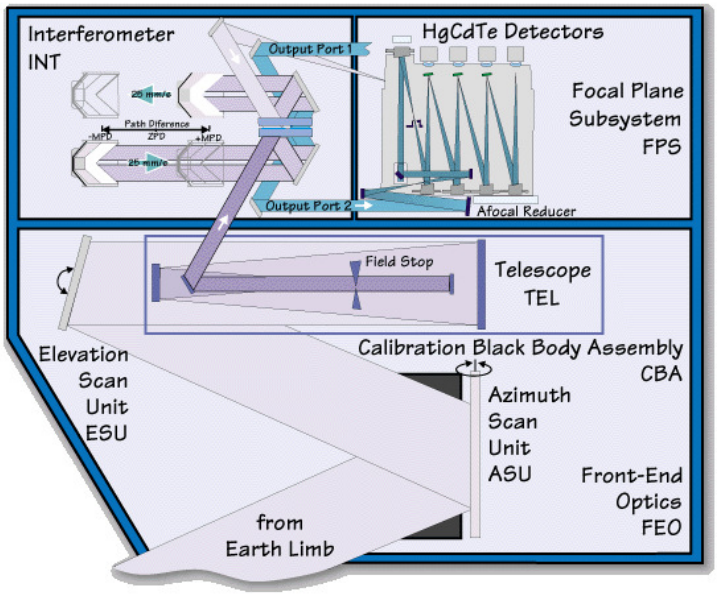

Figure 2.2: Schematic view of the optical layout of MIPAS.

The schematic optical layout of MIPAS and the path of the incoming radiation are shown in Fig. 2.2. The atmospheric radiance enters through the front-end optics. At the entrance, the azimuth scan unit (ASU) allows the selection of the LOS within the two field of view (FOV) directions. Inside the ASU there is an internal black-body source (Calibration Black Body Assembly, CBA) used during the in-flight radiometric gain calibration of the instrument. At the ASU, the light beam is reflected to the elevation scan unit (ESU) that determines the tangent altitude of each measurement. The angle covered by the ESU mirror is less than 3° which is sufficient to encompass limb heights between 5 and 250 km. Although the highest altitude scans by MIPAS is about 170 km, the highest achievable values (and the corresponding altitude of 250 km) were used for measurements of cold space as part of the calibration procedure. After the ESU a reduction of the dimension of the beam is necessary to match the required input dimension of the interferometer. This adaption is made using a telescope (TEL) that also defines the instantaneous field of view (IFOV) using a field stop in the focal plane. The MIPAS IFOV is about 3 km high and 30 km wide (Fig.

2.1). After the TEL the Earth's atmospheric radiance enters the core of MIPAS: the Michelson interferometer.

In order to meet radiometric and instrumental lifetime requirements (initial MIPAS lifetime requirement was 5 years), MIPAS was designed as a symmetrical dual slide interferometer with dual input and output ports. The atmospheric radiance, collected by the front-end optics, enters the interferometer using one of the input port, whereas a second input port is closed with a black-body to suppress disturbing radiance. The output beams of the interferometer are reduced in size by two small telescopes and directed to the focal plane subsystem (FPS) that hosts the Hg-Cd-Te photoconductive detectors. In order to minimize possible thermal emission from the different components, the FPS is maintained at 70 K. Each detector is designed for highest sensitivity in a well-defined spectral band. The entire MIPAS spectral coverage is divided into five spectral bands (Table 2.1). The radiometric sensitivity is expressed by the *Noise Equivalent Spectral Radiance* (NESR), which characterizes the instrument noise on the measurement in terms of incident radiance (see Table 2.1) [73].

MIPAS band	Spectral range (cm^{-1})	FR NESR ($nWcm^{-2}sr^{-1}cm^{-1}$)	OR NESR ($nWcm^{-2}sr^{-1}cm^{-1}$)	Spectrally active molecules
A	685 – 970	30-40	20-25	CO_2, O_3, H_2O, HNO_3, NO_2, CFC-11, CFC-12, $ClONO_2$
AB	1020 – 1170	20	13	O_3, N_2O, CFC-12
B	1215 – 1500	15	9.5	N_2O_5, N_2O, CH_4, H_2O, SO_2, HOCl, $ClONO_2$
C	1570 – 1750	3-5	2-2.5	H_2O, HNO_3, NO_2, $ClONO_2$
D	1820 – 2410	3-5	2-2.5	CO_2, O_3, NO, CO

Table 2.1: MIPAS spectral bands (first column) and corresponding spectral range (second column), NESR of the two phases of the mission (FR and OR, third and fourth columns respectively) and spectrally active retrieved species. Adaption from [73].

At the entrance of the interferometer, the incoming radiation is divided into two beams with the equal intensity by a beam-splitter. These beams are directed towards the two retro-reflectors and come back to the beam-splitter that now works as a beam-combiner. The two reflected beams are now superimposed and interfere with the resulting intensity function of the optical path difference. The interference-modulated output signal, recorded between the start and the end of the mirrors strokes, form an interferogram which is the Fourier Transform of the spectrum of the incoming ra-

diation. Consequently the spectra can be calculated applying an inverse Fourier Transform. The spectral resolution of a Fourier Transform Spectrometer is determined by the Maximum Path Difference (MPD) achievable by the particular interferometer. MIPAS MPD is equal to about 20 cm in the FR part of the mission, and 8 cm in the OR part. Traditional interferometers acquired the interferograms from zero path difference (ZPD) to a maximum length L. Conversely, MIPAS provides double-sided interferograms in which the scan can be on either side of zero from +L to -L. In the MIPAS dual-slide design, the lengths of the two arms of the interferometer are simultaneously modified moving both retro-reflectors at the same time. In order to record a suitable interferogram, the output has to be sampled at extremely regular optical path difference intervals (the MIPAS sampling accuracy is about 30 nm). This is done with the help of a laser beam transmitted in the same optical set up, which is used to trigger the sampling electronics of the detector at very precise path difference positions.

2.3 Measurement modes

During the entire MIPAS mission different measurement modes were used to observe several processes and phenomena in the Earth's atmosphere with either different vertical sampling and different altitude coverage. Due to MIPAS failure in 2004 and the consequent transition to the OR, the original measurement modes were updated to achieve the same scientific objectives by changing the altitude coverage and the altitude sampling grid. The main characteristics and targets of the most used measurement modes are shortly reviewed here and summarize in Tab. 2.2 [73]. For a complete description of all MIPAS measurements modes we refer to `https://earth.esa.int/web/sppa/mission-performance/esa-missions/envisat/mipas/sensor-modes`.

The nominal mode (NOM) represents the standard mode used to study dynamics, chemistry and to provide a database for climatology, trend analyses and near-real-time applications. It covers the upper troposphere, the stratosphere and the lower mesosphere (6–70 km). The NOM mode was used during both mission phases in similar altitude ranges with different vertical samplings (finer for OR phase). The NOM mode was the most used measurement mode in both parts of MIPAS mission.

The upper troposphere / lower stratosphere (UTLS) measurement mode,

Full Resolution (FR, 0.025cm^{-1}) phase (from June 2002 to March 2004)							
Measurement mode	Horizontal sampling	No. of scans	Vertical sampling				
NOM	550 km	17		3 km step 6–42 km	5 km step 42–52 km	8 km step 52–68 km	
Optimized Resolution (OR, 0.0625cm^{-1}) phase (from January 2005 to April 2012)							
Measurement mode	Horizontal sampling	No. of scans	Vertical sampling				
NOM	410 km	27	1.5 km step 6–21 km	2 km step 21–31 km	3 km step 31–46 km	4 km step 46–62 km	4.5 km step 62–71 km
UTLS-1	290 km	19		1.5 km step 8–21.5 km	2 km step 21.5–27.5 km	3 km step 27.5–33.5 km	4.5 km step 33.5–51.5 km
MA	430 km	29			3 km step 18–102 km		
UA	375 km	35		3 km step 42–102 km		5 km step 102–172 km	

Table 2.2: FR (upper part) and OR (lower part) most used measurement modes of MIPAS and their main characteristics. Adaption from [73].

called UTLS-1, is tailored to study atmospheric processes in the UTLS region (including the tropical tropopause layer). The UTLS-1 mode measurements combine a fine vertical sampling in the UTLS (1.5 km step between 8 and 21.5 km) and an altitude coverage that extendes up to about 50 km (with a 3 km vertical step).

In the middle atmosphere (MA) mode the altitude range goes from 18 to 102 km with a 3 km vertical step, covering most of the stratosphere, the mesosphere and the lower thermosphere. This mode focused on observing and studying the linkages between the stratosphere and the upper atmosphere, i.e., the global circulation and transport of NO_X and CO from the mesosphere down to the stratosphere during polar winters. This mode was also used to evaluate and monitor the possible effects of non–local thermodynamic equilibrium (LTE) on the operational retrievals. After MIPAS return to the full duty cycle (December 2007), 1 day of the 10 days measurement cycle was dedicated to MA mode.

The upper atmosphere (UA) mode was dedicated to the measurements of temperature and high-altitude NO. It covers all the mesosphere and the lowest part of the thermosphere (40–170 km). As for MA mode, 1 day of the 10 days cycle was dedicated to UA mode.

2.4 Data processing

Following a detailed procedure, interferometric measurements made by MIPAS are transformed into geolocated and radiometrically calibrated atmospheric limb emission spectra. These spectra are used by an inversion model to produce geo-located vertical profiles of the atmospheric constituents. The

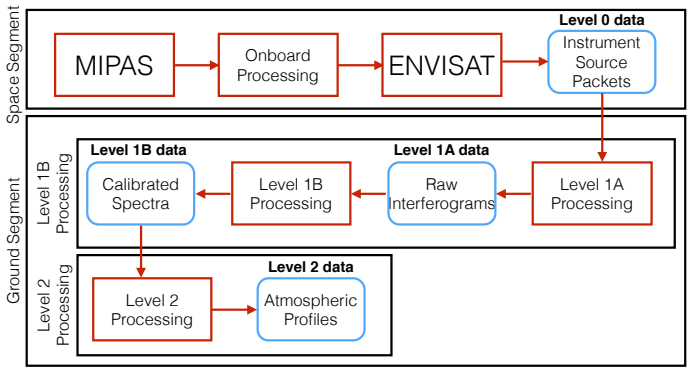

Figure 2.3: Schematic representation of the MIPAS data processing flowchart.

processing chain that leads from the raw measured interferograms to vertical profiles is organized in several steps (Fig. 2.3). This chain is divided in two parts: a *space segment* and a *ground segment*.

The data acquired by the instrument on orbit are transmitted to ESA ground stations where they undergo further stages of processing, resulting in higher level data products. MIPAS **Level 0 data** represent the first step of the processing chain. They correspond to the data stream received directly from the ENVISAT payload without any further processing.

The ground processing consists in two major processing phases: Level 1B and Level 2 processing. Before the Level 1B processing a preliminary step is necessary to reconstruct the interferograms (Level 1A). MIPAS **Level 1A data** are intermediary data, not archived or distributed; they are only used as starting point for the subsequent processing stage.

The goal of the *Level 1B processing* is to decode the instrument source packets and transform the interferograms into calibrated and geolocated spectra of atmospheric radiance. MIPAS **Level 1B data** consist of formatted, geo-located, radiometrically and spectrally calibrated radiance spectra, also annotated with quality indicators.

In the subsequent *level 2 processing* phase, Level 1B data (the calibrated

spectra) are processed to retrieve atmospheric pressure at tangent altitudes, the vertical distribution of temperature and VMR of relevant atmospheric constituents (**Level 2 data**). At the beginning of the MIPAS mission, the near-real-time retrieved species were H_2O, O_3, N_2O, CH_4, HNO_3, and NO_2. The current version of ESA Level 2 data (Version 7) includes 9 additional molecules: CFC–11, $ClONO_2$, N_2O_5, CFC–12, COF_2, CCl_4, HCN, CFC–14, HCFC–22.

Chapter 3

The radiative transfer model

The aim of a radiative transfer model is to simulate the spectra measured by an instrument. The simulation is made starting by some assumptions on the distribution and the properties of the atmospheric constituents. In order to accurately reproduce the measured spectra, a detailed knowledge of the features of the instrument is also crucial. In this section, we focus on the physical, geometric and spectroscopic aspects of a radiative transfer model of a limb-emission sounder, such as MIPAS.

3.1 The radiative transfer model

In the assumption of negligible diffusion processes, to reproduce the measured spectrum for each limb geometry, we have to calculate the following radiative transfer integral

$$S(\sigma, z_g) = \int_{s^b}^{1} B(\sigma, T(s_g))\, d\tau(\sigma, s_g) \tag{3.1}$$

where σ is the wavenumber, z_g is the tangent altitude of the optical path g, s_g is the coordinate along the LOS referred to the optical path g at the tangent altitude z_g, $S(\sigma, z_g)$ is the spectral intensity, $T(s_g)$ is the temperature along the LOS, $B(\sigma, T)$ is the source function, $\tau(\sigma, s_g)$ is the transmission between the point s_g and a generic point s_0 where the observer is located (both points are located on the LOS) and b represents the farthest point that contributes to the signal.

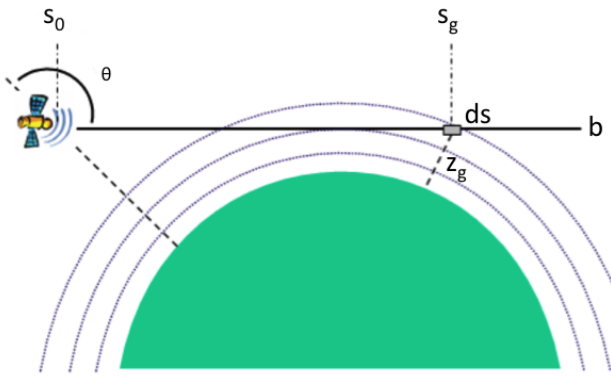

Figure 3.1: Elements defining a limb-scanning observation: s_g is the coordinate along the LOS referred to the optical path g at the tangent altitude z_g, s_0 is the point where the observer is located, and b represents the farthest point that contributes to the signal.

Assuming LTE condition, $B(\sigma, T)$ is the Planck function

$$B(\sigma, T) = \frac{2hc^2\sigma^3}{\exp\left[\frac{hc\sigma}{K_B T}\right] - 1} \tag{3.2}$$

where h is the Planck's constant, c is the light velocity and K_B is the Boltzmann's constant. The transmission $\tau(\sigma, s_g)$ can be represented in terms of s_g

$$\tau(\sigma, s_g) = \exp\left[-\int_{s_0}^{s_g} \overline{k(\sigma, s')}\eta(s')\, ds'\right] \tag{3.3}$$

where $\eta(s_g) = \frac{p(s_g)}{K_B T(s_g)}$ is the number density of the air, and $p(s_g)$ is atmospheric pressure. $\overline{k(\sigma, s')}$ represents the absorption cross sections weighted with the VMR of each absorbing molecules m

$$\overline{k(\sigma, s')} = \sum_{m=1}^{N} k_m(\sigma, s_g) VMR_m(s_g) \tag{3.4}$$

where N is the number of the molecules which absorb in the considered spectral region, $k_m(\sigma, s_g)$ is the absorption cross section of the molecule m, and $VMR_m(s_g)$ is the VMR of the molecule m at point s_g. After these considerations Eq. 3.1 can be rewritten as

$$\begin{aligned} S(\sigma, z_g) &= \int_{s_0}^{s_g^b} B(\sigma, T(s_g)) \frac{d\tau(\sigma, s_g)}{ds_g}\, ds_g = \\ &= \int_{s_0}^{s_g^b} B(\sigma, T(s_g)) \overline{k(\sigma, s_g)} \eta(s_g) \tau(\sigma, s_g)\, ds_g \end{aligned} \tag{3.5}$$

The solution of (Eq. 3.5) needs the knowledge of:

- the optical path and all the variables as $p(s_g)$, $T(s_g)$ and $VMR_m(s_g)$ as a function of s_g, and
- the absorption cross sections $k_m(\sigma, s_g)$ for each absorbing gas m (see Sect. 3.1.2).

3.1.1 The ray tracing

Due to the atmospheric refraction, the ray-path bends towards the Earth and the radiative transfer integral becomes a curvilinear integral along the LOS. The atmospheric refractive index is a function of both temperature and pressure, as the Claussius-Mossotti formula shows:

$$\frac{n^2-1}{n^2+2} = const \cdot \rho(p,T) \tag{3.6}$$

where n is the refractive index and ρ is the density of the air. Bearing in mind that $n-1 \ll 1$, Eq. 3.6 can be rewritten as

$$n = 1 + \alpha_e \cdot \rho(p,T) \tag{3.7}$$

where α_e is an empirical factor. In general, the refractive index is also a function of water vapour content and frequency, however it is possible to show that the dependence on water content and on frequency can be neglected in the MIPAS spectral range with no significant accuracy losses. Assuming a spherical geometry of the Earth and atmospheric layers, we can express the Snell's law using Eq. 3.8

$$n(r) \cdot r \cdot sin(\theta(r)) = \tilde{c} = n(r_t) \cdot r_t \tag{3.8}$$

where r is the sum of the local radius of curvature of the Earth and the altitude of the considered point, r_t is r at the tangent point and θ is the local zenith angle. Using Eq. 3.8 it is possible to calculate the relationship between the tangent height r_r of a refracted beam and the same height r_0 of a non-refracted beam

$$r_r = \frac{r_0}{n} \approx r_0 \cdot (1 - \alpha_e \rho) \tag{3.9}$$

The altitude shift caused by the refraction is about 0.5 – 1.0 km and it increases going through lower altitudes. Considering the relationship $dr = ds \cdot cos(\theta)$ between altitude r, optical path s and local zenith angle θ, Eq.s 3.8 and 3.9 can be combined to obtain

$$ds = \frac{1}{\sqrt{1 - \frac{\tilde{c}^2}{n^2(r) \cdot r^2}}} dr \tag{3.10}$$

To overcome the singularity at the tangent altitude r_t, we change the integration variable to $q_r = \sqrt{r^2 - r_t^2}$ and Eq. 3.10 becomes:

$$ds = \frac{1}{\sqrt{1 + \frac{r_t^2}{n^2(r)} \frac{n^2(r) - n^2(r_t)}{q_r^2}}} dq \tag{3.11}$$

3.1.2 The absorption cross sections

The absorption cross section for a gas m is a function of temperature and pressure and is the sum on all the spectral lines of the species in the chosen interval

$$k_m(\sigma, T, p) = \sum_{i=1}^{Lines} L_{m,l}(T) A_{m,l}(\sigma - \sigma_{m,l}, T, p) \tag{3.12}$$

with $L_{m,l}(T)$ is the line strength of the l-th line of the gas m, $\sigma_{m,l}$ is its central wavenumber, and $A_{m,l}(\sigma - \sigma_{m,l}, T, p)$ is its line shape. The line strength can be calculated as

$$L_{m,l}(T) = L_{m,l}(T_0) \frac{Q_m(T_0)}{Q_m(T)} \cdot \frac{\exp\left[-\frac{hcE''_{m,l}}{K_B T}\right]}{\exp\left[-\frac{hcE''_{m,l}}{K_B T_0}\right]} \cdot \frac{1 - \exp\left[-\frac{hc\sigma_{m,l}}{K_B T}\right]}{1 - \exp\left[-\frac{hc\sigma_{m,l}}{K_B T_0}\right]} \tag{3.13}$$

where $L_{m,l}(T_0)$ is the line strength at reference temperature T_0, $Q_m(T)$ is the total internal partition function and $E''_{m,l}$ is the lower state energy. The line shape is usually modeled with so called, Voigt function ($A^V_{m,l}$), defined as the convolution of the gaussian Doppler ($A^D_{m,l}$) and Lorentz ($A^L_{m,l}$) line profiles

$$A^V_{m,l}(\sigma - \sigma_{m,l}, T, p) = A^D_{m,l}(\sigma - \sigma_{m,l}, T) * A^L_{m,l}(\sigma - \sigma_{m,l}, T, p) \tag{3.14}$$

The Doppler line shape is

$$A^D_{m,l}(\sigma - \sigma_{m,l}, T) = \sqrt{\frac{\ln 2}{\pi}} \frac{1}{\alpha^D_{m,l}} \exp\left[-\ln 2 \frac{(\sigma - \sigma_{m,l})^2}{{\alpha^D_{m,l}}^2}\right] \tag{3.15}$$

where $\alpha^D_{m,l}$ is the Doppler half width at half maximum (HWHM), given by:

$$\alpha^D_{m,l} = \sigma_{m,l} \sqrt{2 \ln 2 \frac{K_B T}{M_m c^2}} \tag{3.16}$$

with M_m molecular mass of the species m. The Lorentz line shape is defined as

$$A^L_{m,l}(\sigma - \sigma_{m,l}, T, p) = \frac{1}{\pi} \frac{\alpha^L_{m,l}}{{\alpha^L_{m,l}}^2 + (\sigma - \sigma_{m,l})^2} \tag{3.17}$$

with

$$\alpha_{m,l}^{L} = \alpha_{m,l}^{L_0} \frac{p}{p_0} \left[\frac{T_0}{T} \right]^{\gamma_{m,l}} \tag{3.18}$$

where $\alpha_{m,l}^{L_0}$ is the Lorentz HWHM at reference pressure p_0 and temperature T_0 and $\gamma_{m,l}$ represents the temperature dependence of the HWHM.

3.1.3 Apodized instrument line shape and field of view

In order to properly simulate the measured radiance, some technical aspects of the instrument have to be considered. In particular the instrumental FOV and the finite spectral resolution have to be taken into account. The finite extension of the moving mirror scan determines maximum optical path difference causing a truncation error. The effects of this truncation can be mathematically reconstructed assuming the measured interferogram as the real interferogram multiplied by a *boxcar* function (windowing operation) which cuts the amplitude of the sampling range. The Fourier Transform of this *boxcar* function is the so-called Instrument Line Shape (ILS). For an "ideal" Fourier Transform spectrometer, the ILS is equal to the *sinc* function, associated with the finite spectral resolution of the instrument. In a "real" instrument, the ILS deviates from the ideal line-shape due to misalignments and distortions of the incoming radiance. Being an important input of the radiative transfer model, a detailed characterization of the ILS line-shape is fundamental. For MIPAS It was experimentally measured and approximated by a function independent on tangent altitude. The ILS function shows oscillations in its wings (side lobes) and it assumes also negative values. In Fourier Transform spectroscopy, in order to reduce the side lobes of the ILS, the measured spectra are commonly apodized, i.e. convolved by a function with a peak slightly broader than that of the original ILS, but with strongly damped side lobes. This procedure introduces correlations among spectral points, which will have to be considered later, in the retrieval phase, when representing the measurement error of the spectra. Despite of this drawback, apodization limits the spectral range influenced by the individual spectral lines, thus permitting faster forward model computations. MIPAS spectra are apodized using the Norton-Beer [61] strong function. The Apodized Instrument Line Shape (AILS, Eq. 3.19) is obtained through the convolution of the measured ILS with the apodization function (APOD)

$$AILS(\sigma) = ILS(\sigma) * APOD(\sigma). \tag{3.19}$$

The AILS is then convolved with the atmospheric radiance simulated by the radiative transfer model (Eq. 3.20). The intent of this operation is to simultaneously take into account all the effects presented here: the finite spectral resolution, the distortion of the line-shape and the apodization.

$$S'(\sigma, z_g) = S(\sigma, z_g) * AILS(\sigma). \tag{3.20}$$

To correctly simulate the measured radiance we also have to consider the finite angular aperture field of view of the instrument. The FOV can be defined as the solid angle through which an instrument is sensitive to the atmospheric radiance. Generally it depends only on design and engineering aspects and its shape can be considered fixed, without any frequency or time dependence. Since MIPAS is located far away from the tangent point of the limb measurements, its angular response function can be in practice represented as a function of the tangent altitude z ($FOV_{MIPAS}(z_g, z)$). Starting from Eq. 3.20, we can take into account the effects of the FOV on the simulated atmospheric radiance performing the following convolution:

$$S^{MIPAS}(\sigma, z_g) = S'(\sigma, z) * FOV_{MIPAS}(z_g, z). \tag{3.21}$$

3.2 MIPAS spectroscopic database

A spectroscopic database is a collection of spectroscopic parameters, such as line position, line intensity and line width, built in order to provide all the necessary spectroscopic inputs for radiative transfer models. An accurate description of these parameters is fundamental because errors and shortcomings in these data directly propagate into the calculated spectra. As part of the auxiliary data of the MIPAS retrieval algorithm, at the beginning of the mission, an *ad-hoc* molecular spectroscopic database was built (HITRAN_MIPAS_PF_3.1, [72]). The dedicated database was designed for near-real-time operational Level 2 analysis [26]. This database was based on HITRAN (HIgh-resolution TRANsmission) 1996 database [81] with several updates supplied by laboratory measurements and new computations [72, 73]. HITRAN represents the first standardized molecular spectroscopic database

and its first version dates from the seventies. The HITRAN database contains spectroscopic parameters of the main absorbers of the Earth's atmosphere. The main goal of HITRAN is to have a theoretically self-consistent set of parameters, while at the same time attempting to maximize the accuracy. The most recent version of the database (HITRAN 2012, [82]) contains more than 7,400,000 spectral lines for 47 different molecules (120 isotopologues) [37].

The MIPAS spectroscopic database has been considerably improved over the MIPAS mission including new species and improving the accuracy of the already existing spectroscopic parameters. The most recent MIPAS spectroscopic database version is HITRAN_MIPAS_PF_4.45 (`http://atmos.difa.unibo.it/spectdb/`). Details about the recent improvements can be found in [72, 73].

3.3 MIPAS database of climatological profiles

In order to simulate the atmospheric radiances measured by the instrument, some assumptions about the atmosphere are needed. The MIPAS climatology, the so-called *IG2 atmospheres*, was created as part of the studied for MIPAS near-real-time operational processing [74]. The climatology was built combining already available satellite measurements, in-situ observations (i.e. radiosondes, ground-based networks) and model simulations. The climatology consists of reference profiles of atmospheric pressure, temperature, and VMR of more than 30 atmospheric constituents as function of both latitude and time. The profiles range from the surface to 120 km and are represented using a 1 km vertical grid step. In the IG2 atmospheres, the profiles are organized into 6 different latitudinal bands (Tab. 3.1) and into 4 climatological seasons (Tab. 3.2). As an example, Fig.s 3.2 and 3.3 show respectively the O_3 and H_2O IG2 version 4.1 climatological profiles as a function of season, altitude and latitude.

Latitude band	Latitude range
Polar South	from 90°S to 65°S
Mid-latitude South	from 65°S to 20°S
Tropical South	from 20°S to 0°
Tropical North	from 0° to 20°N
Mid-latitude North	from 20°N to 65°N
Polar North	from 65°N to 90°N

Table 3.1: The IG2 climatology latitudinal bands.

Season	Months	Acronym
Winter	December, January, February	DJF
Spring	March, April, May	MAM
Summer	June, July, August	JJA
Autumn	September, October, November	SON

Table 3.2: The IG2 climatological seasons (refer to the Northern hemisphere), the corresponding months and the acronym.

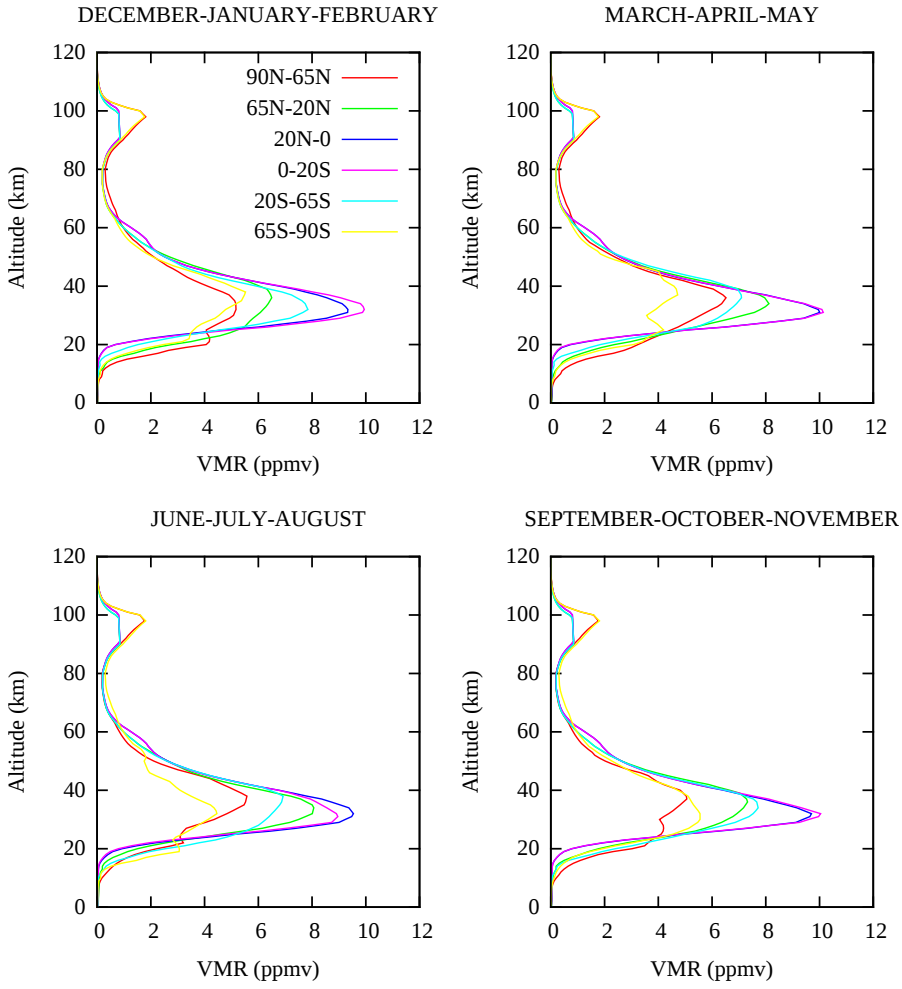

Figure 3.2: The O_3 IG2 version 4.1 climatological profiles for winter (upper left), spring (upper right), summer (lower left) and autumn (lower right) 2012. For each season, polar north (red lines), mid-latitude north (green lines), tropical north (blue lines), tropical south (violet lines)p, mid-latitude south (cyan lines) and polar south (yellow lines) climatological profiles are reported.

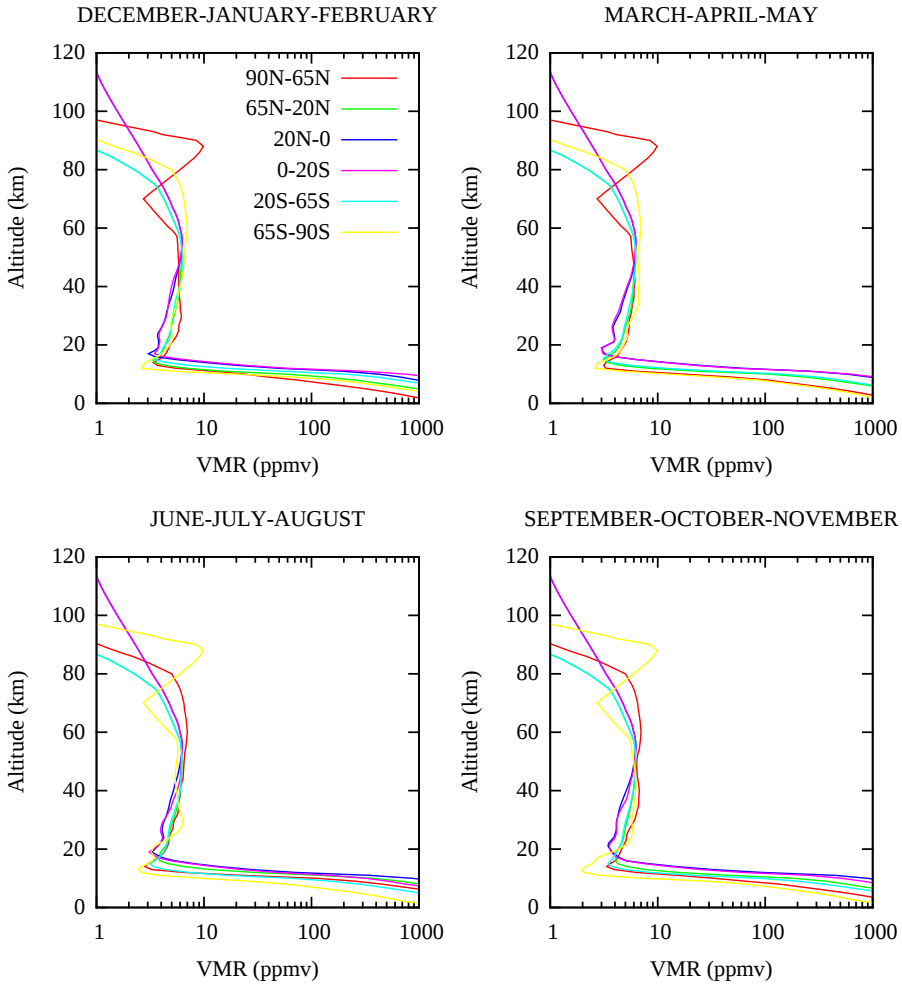

Figure 3.3: Same as for Fig 3.2 but for H_2O.

Chapter 4

The inverse problem

The forward model (Chap. 3) has been defined as the mapping from the state of the atmosphere to the quantities that we are able to measure. Remote-sensing measurements are typically indirect, and they are used whenever direct measurements are difficult or expensive, although they often introduce complex problems of interpretation. In this kind of techniques, the measured quantity contains information about the required atmospheric properties and the problem to retrieve these quantities is known as the *inverse problem*. The concepts and the notations used in this chapter are those that can be found in [78], an exhaustive and useful textbook regarding remote sensing retrieval techniques.

4.1 Inverse problem

The inverse problem can be written as

$$\mathbf{y} = \mathbf{F}(\mathbf{x}) + \varepsilon \tag{4.1}$$

where $\mathbf{y}$ [1] is the *measurement vector* (with m elements), $\mathbf{x}$ is the atmospheric state vector (with n elements) and ε is the *measurement noise*. Generally, inverse problems have a near-linear nature which has allowed the development of inverse methods based on linear theory. If the non-linearities are not negligible, a liberalization of the forward model about some reference state $\mathbf{x}_0$ is often an adequate approximation:

$$\mathbf{y} - \mathbf{F}(\mathbf{x}_0) = \frac{\partial \mathbf{F}(\mathbf{x})}{\partial \mathbf{x}}(\mathbf{x} - \mathbf{x}_0) + \varepsilon = \mathbf{K}(\mathbf{x} - \mathbf{x}_0) + \varepsilon$$

where $\mathbf{K}$ is the $m \times n$ Jacobian matrix, or the kernel, in which each element is the partial derivative of a forward model element with respect to a state vector element, i.e. $K_{ij} = \partial F_i(x)/\partial x_j$.

4.1.1 Linear inverse problem without measurement noise

In the linear problem case without measurement noise, the problem can be reduced to find the solution of the following linear set of equations

$$\mathbf{y} = \mathbf{K}\ \mathbf{x}$$

and can have no solutions, one solution or an infinite number of solutions.

If $\boxed{m < n}$, the problem is *under-constrained* because the number of unknowns exceeds the number of simultaneous equations and the parameters can not be determined from the measurements. In order to make the problem well-determined is it possible to reduce the number of unknowns.

If $\boxed{m = n = p}$, an unique solution, the so-called *exact solution*, can be found. p is the *rank* of the matrix $\mathbf{K}$ and it represents the dimension of the subspace of the state space spanned by the $\mathbf{K}_j$ weighting functions.

[1] In the following lowercase bold characters indicate vectors while uppercase bold characters denote matrices.

If $\boxed{m > n}$, the problem is described as *over-constrained* and two scenarios are possible. If $\boxed{p < n}$, the measurements are "blind" to certain aspects of the unknowns. This under-determined part of state space, with dimension $n - p$, is called *null space* of $\mathbf{K}$. On the other hand, if $\boxed{m > p = n}$, there is not a single solution that fits all the measurements and we have to apply some criteria to identify the "best" solution.

One of the most used criteria is the least squares approach, that minimizes the χ^2 function, defined as the sum of the squares of the differences between the measurements and the simulations (the *residuals*)

$$\chi^2 = (\mathbf{y} - \mathbf{K}\hat{\mathbf{x}})^T(\mathbf{y} - \mathbf{K}\hat{\mathbf{x}}) \tag{4.2}$$

The minimization of the χ^2 can be made deriving Eq. 4.2 with respect to $\mathbf{x}$ and equating to zero

$$\frac{\partial}{\partial \hat{\mathbf{x}}}(\mathbf{y} - \mathbf{K}\hat{\mathbf{x}})^T(\mathbf{y} - \mathbf{K}\hat{\mathbf{x}}) = -2\mathbf{K}^T(\mathbf{y} - \mathbf{K}\hat{\mathbf{x}}) = 0 \tag{4.3}$$

obtaining

$$\mathbf{K}^T\mathbf{K}\hat{\mathbf{x}} = \mathbf{K}^T\mathbf{y}. \tag{4.4}$$

$\mathbf{K}^T\mathbf{K}$ is an $n \times n$ square matrix and it is invertible if $\boxed{\text{p = n}}$. If the matrix is invertible, a unique solution exists and the best fit parameters $\hat{\mathbf{x}}$ can be found as

$$\hat{\mathbf{x}} = (\mathbf{K}^T\mathbf{K})^{-1}\mathbf{K}^T\mathbf{y}. \tag{4.5}$$

where $(\mathbf{K}^T\mathbf{K})^{-1}\mathbf{K}^T$ is known as the Moore-Penrose inverse or the "generalized inverse" of $\mathbf{K}$. The $\boxed{p < n}$ condition is also possible. In this case, infinite solutions exist and all of them minimize the χ^2 (the χ^2 function has a "degenerate" minimum or a "flat valley").

4.1.2 Adding the measurement noise

Real world experiments are affected by measurements uncertainties or noise. For this reason every retrieval approach has to take into account also this

aspect. The experimental uncertainty can be efficiently approximated as a Gaussian distribution P(y) with a mean $\bar{y}$ and variance σ^2. Working with vector quantities, different elements of the vector may be correlated:

$$S_{\epsilon_{ij}} = E\{(y_i - \overline{y}_i)(y_j - \overline{y}_j)^T\} \neq 0 \tag{4.6}$$

where $S_{\epsilon_{ij}}$ is the *covariance* of y_i and y_j, and ε is the expected value. These covariances can be assembled in the variance-covariance matrix of $\mathbf{y}$ ($\mathbf{S}_\epsilon$). Note that the diagonal elements of $\mathbf{S}_\epsilon$ are the variances of the individual elements of $\mathbf{y}$. A variance-covariance matrix is symmetric and non-negative definite. We can write the Gaussian distribution for $\mathbf{y}$ in the following form

$$P(\mathbf{y}) = \frac{1}{(2\pi)^{\frac{n}{2}}|\mathbf{S}_\epsilon|^{\frac{1}{2}}}\, exp(-\frac{1}{2}(\mathbf{y} - \hat{\mathbf{y}})^T\mathbf{S}_\epsilon^{-1}(\mathbf{y} - \hat{\mathbf{y}})) \tag{4.7}$$

In the case previously discussed (see Sect. 4.1.1), the least squares approach can be used assuming a zero mean Gaussian distributed noise with covariance matrix $\mathbf{S}_\varepsilon$. For this case, the χ^2 function can be rewritten as

$$\chi^2 = (\mathbf{y} - \mathbf{K}\hat{\mathbf{x}})^T\mathbf{S}_\varepsilon^{-1}(\mathbf{y} - \mathbf{K}\hat{\mathbf{x}}), \tag{4.8}$$

and minimized by deriving with respect to $\mathbf{x}$ and equating to zero, obtaining the besti fit parameters

$$\hat{\mathbf{x}} = (\mathbf{K}^T\mathbf{S}_\varepsilon^{-1}\mathbf{K})^{-1}\mathbf{K}^T\mathbf{S}_\varepsilon^{-1}\mathbf{y}. \tag{4.9}$$

The expected value of the χ^2 function (Eq. 4.8) is $m - n$. For simplicity, we can define the χ^2_N normalized as:

$$\chi^2_N = \frac{\chi^2}{m - n} \tag{4.10}$$

with an expectation value of 1. The deviation of the χ^2_N from 1 quantifies an estimate of the agreement between the model and the observations.

4.2 Bayesian approach

Due to the ill-posed nature[2] of the inverse problem, the mathematical solutions can appear without any physical sense or too far from our a-priori knowledge of the problem. Therefore, statistical methods can be very useful to combine the information coming from the measurements with some previous information. The Bayesian approach is very helpful if you have an a-priori knowledge or expectation about some quantity and you want to update your understanding on the basis of new information coming from the observation. The Bayes' theorem explains the relationship between the conditional probability of $\mathbf{y}$ given $\mathbf{x}$, $\mathrm{P}(\mathbf{y}|\mathbf{x})$, and the conditional probability of $\mathbf{x}$ given $\mathbf{y}$, $\mathrm{P}(\mathbf{x}|\mathbf{y})$.

$$P(\mathbf{x}|\mathbf{y}) = \frac{P(\mathbf{y}|\mathbf{x})P(\mathbf{x})}{P(\mathbf{y})}, \tag{4.11}$$

where $\mathrm{P}(\mathbf{x}|\mathbf{y})$ is the quantity that we obtain when we update the *a-priori* knowledge $\mathrm{P}(\mathbf{x})$ of the state with the measurement $\mathbf{y}$. $\mathrm{P}(\mathbf{x}|\mathbf{y})$ needs the knowledge of the forward model and the distribution of the measurement error. For simplicity, $\mathrm{P}(\mathbf{y})$ can be considered as a normalization factor and is often not needed.

4.2.1 Linear problem

As example of Bayesian approach, we consider a linear problem in which all of the *pdf* are Gaussian. In the linear problem the forward model is linear, hence

$$\mathbf{y} = \mathbf{F(x)} + \varepsilon = \mathbf{K}\ \mathbf{x} + \varepsilon$$

It is useful to introduce two *cost functions* (scalar quantities), defined as the logarithm of the Gaussian distribution (as Eq. (4.7)), to rewrite $P(\mathbf{y}|\mathbf{x})$ and $P(\mathbf{x})$ respectively as

$$-2\ln P(\mathbf{y}|\mathbf{x}) = (\mathbf{y} - \mathbf{Kx})^T \mathbf{S}_\varepsilon^{-1} (\mathbf{y} - \mathbf{Kx}) + c_1, \tag{4.12}$$

[2] An inverse problem can be defined *ill-posed* if one or more of the following are true: *i)* the inverse of the forward operator does not exist, *ii)* the inverse exists but it is not unique, *iii)* a small change in the measured data produces a large change in the solution (*ill-conditioned*).

$$-2\ln P(\mathbf{x}) = (\mathbf{x}-\mathbf{x}_a)^T\mathbf{S}_a^{-1}(\mathbf{x}-\mathbf{x}_a) + c_2, \tag{4.13}$$

where c_1 and c_2 are two constants (independent of $\mathbf{x}$), $\mathbf{S}_\varepsilon$ is the measurement covariance matrix, $\mathbf{x}_a$ is the *a-priori* value of $\mathbf{x}$ and $\mathbf{S}_a$ is the *a-priori* covariance matrix. In order to obtain the *a-posteriori pdf*, Eq. (4.11) can be rewritten using Eq.s (4.12) and (4.13), obtaining

$$-2\ln P(\mathbf{x}|\mathbf{y}) = (\mathbf{y}-\mathbf{K}\mathbf{x})^T\mathbf{S}_\varepsilon^{-1}(\mathbf{y}-\mathbf{K}\mathbf{x}) + (\mathbf{x}-\mathbf{x}_a)^T\mathbf{S}_a^{-1}(\mathbf{x}-\mathbf{x}_a) + c_3, \tag{4.14}$$

where c_3 is also a constant. This expression includes the cost function of the measurements (-ln P($\mathbf{y}$)). P($\mathbf{x}|\mathbf{y}$) is quadratic form in $\mathbf{x}$, thus we can represent it as a Gaussian distribution with expected value $\hat{\mathbf{x}}$ and covariance $\hat{\mathbf{S}}$. Furthermore, we can define a new *cost function*:

$$-2\ln P(\mathbf{x}|\mathbf{y}) = (\mathbf{x}-\hat{\mathbf{x}})^T\hat{\mathbf{S}}^{-1}(\mathbf{x}-\hat{\mathbf{x}}) + c_4. \tag{4.15}$$

Equating Eq.s (4.14) and (4.15), we obtain the following

$$\mathbf{x}^T\mathbf{K}^T\mathbf{S}_\varepsilon^{-1}\mathbf{K}\mathbf{x} + \mathbf{x}^T\mathbf{S}_a^{-1}\mathbf{x} = \mathbf{x}^T\hat{\mathbf{S}}^{-1}\mathbf{x}$$

from which it turns out that:

$$\hat{\mathbf{S}}^{-1} = \mathbf{K}^T\mathbf{S}_\varepsilon^{-1}\mathbf{K} + \mathbf{S}_a^{-1}. \tag{4.16}$$

Similarly equating the terms linear in $\mathbf{x}^T$ we obtain

$$(-\mathbf{K}\mathbf{x})^T\mathbf{S}_\varepsilon^{-1}\mathbf{y} + \mathbf{x}^T\mathbf{S}_a^{-1}(-\mathbf{x}_a) = \mathbf{x}^T\hat{\mathbf{S}}^{-1}\hat{\mathbf{x}}.$$

Canceling the $\mathbf{x}^T$ terms, because this expression must be valid for any value of $\mathbf{x}$, and inserting Eq. (4.16) we obtain

$$\mathbf{K}^T\mathbf{S}_\varepsilon^{-1}\mathbf{y} + \mathbf{S}_a^{-1}\mathbf{x}_a = (\mathbf{K}^T\mathbf{S}_\varepsilon^{-1}\mathbf{K} + \mathbf{S}_a^{-1})\hat{\mathbf{x}}$$

and

$$\hat{\mathbf{x}} = (\mathbf{K}^T\mathbf{S}_\varepsilon^{-1}\mathbf{K} + \mathbf{S}_a^{-1})^{-1}(\mathbf{K}^T\mathbf{S}_\varepsilon^{-1}\mathbf{y} + \mathbf{S}_a^{-1}\mathbf{x}_a). \tag{4.17}$$

4.2.2 Non-linear inverse problems

A non-linear inverse problem can be easily defined as a problem in which the forward model is *non-linear*. Moreover, it is also possible that non-quadratic terms, due to the *a-priori* constraint, lead to a non-linear problem even if the forward model is linear. It is important to note that any non-Gaussian *a-priori pdf* will lead to a non-linear problem.
The inverse problems can be classified as function of their linearity:

- *Linear*: the forward model can be put in the form $\mathbf{y} = \mathbf{K}\mathbf{x}$ and all the *pdf*'s are Gaussian.
- *Nearly linear*: the forward model is non-linear, but a linearization about some reference state is adequate to find a solution.
- *Moderately non-linear*: the linearization is adequate for the error analysis, but it is not for finding a solution.
- *Grossly non-linear*: problem deeply non-linear even within the error range.

The approach exposed for the *linear* case (Sect. 4.2.1) can be applied, after an appropriate linearization, also to *moderately non-linear* problems. In this case, the most important difference with respect to *linear* and *nearly linear* cases is that the explicit solution does not exist but it must be found numerically or iteratively.

The Bayesian solution for the linear case (Eq. 4.14, with or without the *a-priori* information respectively) can be generalized to include all the inverse problem in which the forward model is a general function $\mathbf{F}(\mathbf{x})$ of the state, also non-linear, and the measurement error is Gaussian:

$$\begin{aligned} &[\mathbf{y} - \mathbf{F}(\mathbf{x})]^T\mathbf{S}_\varepsilon^{-1}[\mathbf{y} - \mathbf{F}(\mathbf{x})] + [\mathbf{x} - \mathbf{x}_a]^T\mathbf{S}_a^{-1}[\mathbf{x} - \mathbf{x}_a] \\ &\qquad\qquad\qquad\qquad\qquad\qquad\qquad\qquad or \\ &[\mathbf{y} - \mathbf{F}(\mathbf{x})]^T\mathbf{S}_\varepsilon^{-1}[\mathbf{y} - \mathbf{F}(\mathbf{x})]. \end{aligned} \tag{4.18}$$

Note that, until *moderately non-linear* problems, if the measurement error *pdf* is Gaussian, the retrieval error *pdf* will be Gaussian.

4.3 Gauss-Newton method

The Gauss-Newton algorithm is a numerical method used for finding the minimum of a given function, such as Eq. (4.18). It represents a modification of the Newton's method. Considering a general vector equation $\mathbf{g}(\mathbf{x}) = \mathbf{y} - \mathbf{F}(\mathbf{x}) = 0$, the Newton's iteration can be written:

$$\mathbf{x}_{i+1} = \mathbf{x}_i - [\nabla_x \mathbf{g}(\mathbf{x}_i)]^{-1} \mathbf{g}(\mathbf{x}_i), \tag{4.19}$$

where $\mathbf{x}_i$ is the initial guess of $\mathbf{x}$ and $\nabla_x \mathbf{g}$ is the second derivative of the cost function, Eq. (4.18), known as the *Hessian*

$$\begin{aligned} \nabla_x \mathbf{g} &= \mathbf{S}_a^{-1} + \mathbf{K}^T \mathbf{S}_\varepsilon^{-1} \mathbf{K} - [\nabla_x \mathbf{K}^T] \mathbf{S}_\varepsilon^{-1} [\mathbf{y} - \mathbf{F}(\mathbf{x})] \\ &\qquad\qquad\qquad\qquad\qquad\qquad\qquad\qquad or \\ \nabla_x \mathbf{g} &= \mathbf{K}^T \mathbf{S}_\varepsilon^{-1} \mathbf{K} - [\nabla_x \mathbf{K}^T] \mathbf{S}_\varepsilon^{-1} [\mathbf{y} - \mathbf{F}(\mathbf{x})]. \end{aligned} \tag{4.20}$$

The Hessian needs the computation of both the Jacobian $\mathbf{K}$ and the second derivative of the forward model, $\nabla_x \mathbf{K}^T$. The second term is a quite complicated object and in many cases can be neglected. This assumption represents the modification of the Gauss-Newton method with respect to the Newton method. The iterative solution in a non-linear problem with and without the *a priori* information, also known as *optimal estimation* (OE), can be written as

$$\begin{aligned} \mathbf{x}_{i+1} &= \mathbf{x}_i + (\mathbf{S}_a^{-1} + \mathbf{K}_i^T \mathbf{S}_\varepsilon^{-1} \mathbf{K}_i)^{-1} [\mathbf{K}_i^T \mathbf{S}_\varepsilon^{-1} (\mathbf{y} - \mathbf{F}(\mathbf{x}_i)) - \mathbf{S}_a^{-1} (\mathbf{x}_i - \mathbf{x}_a)] \\ &\qquad\qquad\qquad\qquad\qquad\qquad\qquad\qquad or \\ \mathbf{x}_{i+1} &= \mathbf{x}_i + (\mathbf{K}_i^T \mathbf{S}_\varepsilon^{-1} \mathbf{K}_i)^{-1} \mathbf{K}_i^T \mathbf{S}_\varepsilon^{-1} [\mathbf{y} - \mathbf{F}(\mathbf{x}_i)] \end{aligned} \tag{4.21}$$

where $\mathbf{K}_i = \mathbf{K}(\mathbf{x})|_{\mathbf{x}_i}$.

4.4 Levenberg-Marquardt method

The Gauss-Newton method is quite powerful, but it may fail in strong non-linear conditions. In general, it gives bad results if the true solution is sufficiently far from the assumed solution. For these non-linear least squares problem, Levenberg [52] proposed to add a new term to Eq. 4.21:

$$\mathbf{x}_{i+1} = \mathbf{x}_i + (\mathbf{K}_i^T \mathbf{S}_\varepsilon^{-1} \mathbf{K}_i + \lambda_{LMi} \mathbf{I})^{-1} \mathbf{K}_i^T \mathbf{S}_\varepsilon^{-1} [\mathbf{y} - \mathbf{F}(\mathbf{x}_i)] \tag{4.22}$$

where $\mathbf{I}$ is the identity matrix and λ_{LMi} is a positive scalar parameter chosen at each step in order to minimize the cost function, in our case the χ^2. This procedure to select λ_{LMi} is computational expensive, thus Marquardt [56] simplified the selection starting a new iteration step as soon as a new λ_{LMi} is found for which the cost function is reduced. Note that for the limit $\lambda_{LM} \to 0$, the Levenberg-Marquardt method falls again in the Gauss-Newton case.

4.5 Averaging Kernels

Deriving Eq. 4.3 with respect to $\mathbf{x}_{i-1}$ at the last iteration, we obtain the averaging kernel (AK) matrix

$$\mathbf{A} = (\mathbf{K}^T \mathbf{S}_\varepsilon^{-1} \mathbf{K} + \mathbf{S}_a)^{-1} \mathbf{K}^T \mathbf{S}_\varepsilon^{-1} \mathbf{K} \tag{4.23}$$

$\mathbf{A}$ represents a measure of the sensitivity of the retrieved state vector $\hat{\mathbf{x}}$ produced by a small perturbation in the true state of the atmosphere: $A_{ij} = \partial \hat{x}_i / \partial x_j$, where $\hat{x}_i$ is the i^{th} component of the retrieved state $\hat{\mathbf{x}}$ and x_j is the j^{th} component of the true atmospheric state.

The rows of $\mathbf{A}$, also known as the *averaging kernels* ($\mathbf{a}_i$), indicate how much the i^{th} component of the retrieval is sensitive to the different components of the atmospheric state. In an ideal retrieval method, perfectly constrained, $\mathbf{A}$ would be a unit matrix. For a well constrained retrieval, $\mathbf{a}_i$ is a sharped function with the peak close to 1 at its i^{th} component. For an ill-posed problem, the peak value and the sum of all components of $\mathbf{a}_i$ tends to 0. The width of the averaging kernel $\mathbf{a}_i$, commonly computed as the full width at half maximum (FWHM), is a measure of the vertical resolution of

the retrieval.

Another indication of the retrieval sensitivity is represented by the number of degrees of freedom (DOF) of the retrieval, which is defined as the trace of **A**. For a well constrained problem the number of DOF is close to the number of retrieved parameters.

4.6 The Optimized Retrieval Model (ORM)

The ORM [76, 72, 73] was originally designed in order to process continuously and in *near-real-time* MIPAS measurements. Therefore, a trade-off between retrieval accuracy and run time was necessary and, for this purpose, some physical and mathematical optimizations of the retrieval scheme were implemented.

The retrieval is based on the use of MicroWindows (MWs, [19, 104]), selected spectral intervals not wider than 3 cm^{-1}. These intervals contain relevant information on the target parameters and permit to avoid the analysis of spectral regions affected by systematic errors or without any information regarding the targets. The MIPAS MW database was created with the aim to minimize the retrieval error. It was continuously updated during the MIPAS mission to include more accurate spectroscopic data and new retrieved gases.

The retrieval is based on the non-linear least squares fit with the Levenberg – Marquardt approach (Sect. 4.4). The vertical distribution of each geophysical parameter is retrieved simultaneously at all altitudes using the entire MIPAS limb scanning sequence, the so-called global fit approach [9]. The main advantage of this approach over the old "onion peeling" method [30] is that it properly accounts for the error propagation on the retrieved quantity in the vertical domain and allows the use of retrieval altitudes independent of the geometry of the observed spectra.

The ORM retrieves the geophysical parameters sequentially. Temperature and pressure are simultaneously retrieved first. The employed approach uses the hydrostatic equilibrium assumption. Then, the VMRs of several target species are retrieved individually, in sequence, according to their reciprocal spectral interference. The original retrieval sequence considering only the six main targets was: H_2O, O_3, HNO_3, CH_4, N_2O, NO_2. Currently, in the most recent version of MIPAS Level 2 data (Version 7) the

retrieval chain is: H_2O, O_3, N_2O, CH_4, HNO_3, NO_2, CFC–11, $ClONO_2$, N_2O_5, CFC–12, COF_2, CCl_4, HCN, CFC–14 and HCFC–22

The so-called atmospheric *continuum* is another auxiliary profile of inversion parameters in each retrieval. It can be defined as the absorption contribution of all emission sources that are frequency independent in a MW. This contribution is mainly caused by the wings of far lines, the pressure broadened bands of O_2 and N_2 and the emission of aerosols. In the ORM, the *continuum* vertical profile is retrieved for each MW.

4.6.1 Retrieval scheme

The ORM retrieval scheme is organized as follows (Fig. 4.1). Using an *initial-guess* of the unknown parameters and information on MIPAS instrument characteristics and observation geometry, the forward model computes the initial simulated spectra. The simulated spectra are then compared with the measured MIPAS Level 1b spectra (see Sect.2.4) providing the cost function (χ^2) that has to be minimized. A convergence criterion must be defined in order to "decide" if the χ^2 minimum has been reached with sufficient accuracy. If the convergence criteria are verified, the procedure stops and the outputs are generated. By contrast, if the convergence is not reached, an additional iteration is started according to Eq. 4.22. The improved profile is now used for generating new simulated spectra that are again compared with the MIPAS Level 1b spectra. The procedure is iterated until the convergence criteria are verified.

4.6.2 Optimized forward model

From the computational point of view, the most expensive part of the retrieval scheme is the computation of the forward model (Eq.s 3.5, 3.20, 3.21). The equations involved need many operations, repeated for the number of the variables and for the number of the iterations. On the other hand, the ORM was conceived as a *near-real-time* processor with well-defined run-time requirements. In order to optimize the computation of radiative transfer, an *optimized forward model* was developed. The main targets of this model were to optimize the sequence of operations, avoiding repetition of the same calculations, minimize the number of memorized quantities and perform the calculations with the required accuracy. The most important optimizations

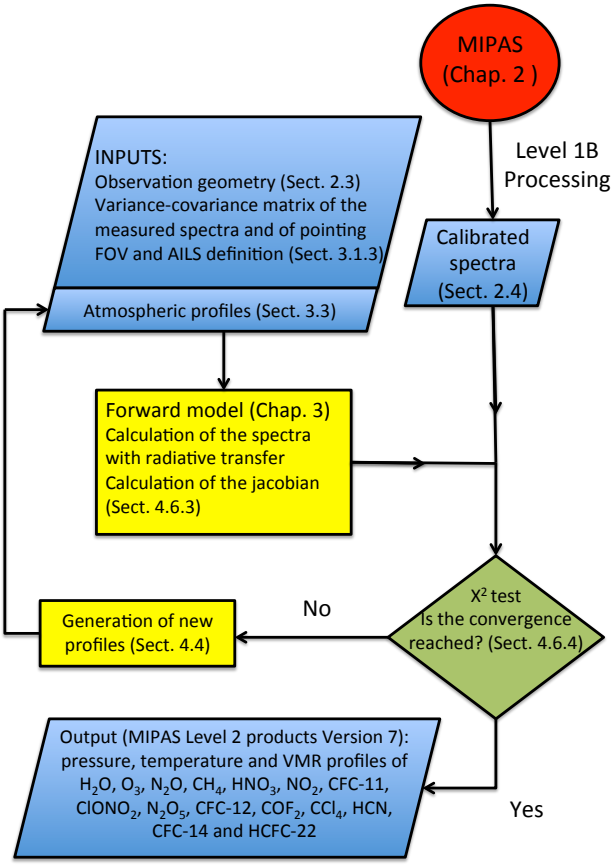

Figure 4.1: ORM retrieval algorithm scheme.

implemented in the *optimized forward model* are briefly described in the following.

Frequency grid As reported in Sect. 3.1.2, the spectral line shape depends on temperature and pressure due to effects of the Doppler and the Lorentz broadening. In order to sample all the features of the spectrum, a sufficiently fine frequency grid has to be used. The simplest approach is to choose a frequency grid fine enough to resolve the narrowest line at high altitude. This approach, based on the *fine grid* (0.0005 cm^{-1}), requires a large number of calculations and, as consequence, an excessive amount of computing time and storage. The *optimized forward model* uses a different approach, observing that not all the points of the *fine grid* are necessary to adequatly reconstruct the spectral distribution. In many cases, a subset of

spectral grid points, the so-called *irregular grid*, is sufficient. *Ad-hoc irregular grid* is defined for each MW and the calculations are performed only for this *irregular grid*, the remaining spectral points are obtained using a simple linear interpolation scheme.

Definition of the atmospheric layering The non-homogeneous properties of the atmosphere along the ray path has been managed dividing the atmosphere into a set of homogeneous layers. Assuming a layered atmosphere the calculation of the radiative transfer integral (Eq. 3.1) becomes a summation over all the layers intercepted by the ray path. Since the transmittance weighting functions for limb observations peak near the tangent point, it is important that a fine layer structure is used in the vicinity of the tangent points.

For each homogeneous layer appropriate "equivalent" temperature and pressure, or Curtis-Godson [41] quantities, have to be determined. Generally, the Curtis-Godson quantities have to be calculated for each layer and each limb observation. Assuming flat layers and straight LOS, the equivalent pressures and temperatures are independent on the limb angle between the LOS and the vertical direction (secant law approximation). Under this approximation, it is sufficient to calculate the Curtis-Godson quantities for all the layers of the lowermost limb observation, and only for the lowest layer of the other limb observation. The secant law approximation introduces small errors, except at the tangent altitude where the error is larger, but allows the calculation of a reduced number of equivalent pressures and temperatures. As a consequence, the cross-sections have to be computed, and stored, for a smaller number of pressure-temperature pairs (see next paragraph). Furthermore, assuming a spherically symmetric atmosphere, the transmittance is symmetrical in the two sides of the tangent point and therefore path parameters have to be calculated only for one of the two sides.

Absorption cross sections Considering the spectral resolution needed, the number of spectral lines and the number of pressure and temperature (p, T) combinations for which they have to be computed, the computation of the absorption cross sections (Sect. 3.1.2) is one of the most computational expensive parts of the forward model. A common approach is the Line-By-Line (LBL) calculation, in which the computation is performed for

every line at every wavenumber grid point with a pre-defined spectroscopic database. The *optimized forward model* uses a different approach based on the computation of the so-called Look-Up Tables (LUTs). The idea behind the LUTs [98] is to pre-calculate the absorption cross sections and store them into tabulated files, the LUTs. The computation is made for each species, for each frequency grid point (only at a subset considering the *irregular grid* approach) and for a pre-defined set of (p, T) pairs. At the beginning of each retrieval, the LUTs are read and interpolated to the actual pressure and temperature pairs for which they are needed. The LUTs and irregular grids combined approach reduces significantly the computing cost.

AILS and FOV convolution We have already discuss that, in order to properly simulate the measured spectra, the forward model has to take into account also some instrument technical aspects such as the AILS and the FOV (Sect. 3.1.3). The *optimized forward model* has been designed to make in the same step, the convolution of the simulated spectra with the AILS and the resampling of the convolved spectra from the *irregular grid* to the MIPAS instrument *coarse grid*. The *optimized forward model* also avoids repetition in the computation of adjacent altitudes spectra, exploiting the simultaneous computation of the entire sequence of MIPAS limb scanning spectra (*global fit approach*) and the MIPAS FOV linear relationship with tangent altitude.

4.6.3 Jacobian calculation

Another expensive part in the retrieval algorithm is the computation of the derivatives of the radiance with respect to the retrieval parameters. In many codes derivatives are computed by the sequential evaluation of the incremental ratio. In this approach the elements of the state vector are perturbed individually, the forward model recomputed and the differences to the unperturbed spectrum calculated. This method therefore requires to run the forward model several times. On the contrary, for tangent pressure, VMRs and atmospheric continuum retrievals, the ORM computes the different terms of the Jacobian matrix analytically, exploiting the analytical derivatives implemented in the code. When the calculation of analytical derivatives is expensive anyway (as for temperature retrieval), an optimized numerical approach is implemented. In these cases, the derivatives are computed in

parallel with the spectra in order to exploit the common calculations.

4.6.4 Convergence criteria

As anticipated in Sect. 4.6.1, convergence criteria have to be established in order to decide when the minimum of the χ^2 function has been reached. The ORM convergence criteria are based on the following conditions [73]:

i) the relative difference between the calculated χ^2 and the expected χ^2 (computed in the linear approximation) is less than a pre-defined threshold t_1;

ii) the maximum relative correction to the target parameters is less than a pre-defined threshold t_2;

iii) the relative difference between the χ^2 calculated at the current iteration and the χ^2 calculated at the at the previous iteration is less than a pre-defined threshold t_3. This condition is evaluated only if the current χ^2 is less than pre-defined threshold t_5.

iv) the $n-$dimensional state vector x at the current (i) and at the previous $(i-1)$ iteration are compatible within the covariance matrix $\mathbf{S}_{\hat{\mathbf{x}}_i}$ error

$$\sqrt{\frac{(\mathbf{x}_i - \mathbf{x}_{i-1})^T \mathbf{S}_{\hat{\mathbf{x}}_i}^{-1} (\mathbf{x}_i - \mathbf{x}_{i-1})}{n}} < t_4$$

4.6.5 Error budget

The main error components affecting each individual profiles are evaluated within each MW using the MWMAKE tool [19]. The MWMAKE tool computes the measurement noise in the retrieval, as evaluated for typical FR and OR retrievals. Moreover, the measurement noise is accurately mapped using the error covariance matrix provided by the ORM retrieval algorithm [12]. The other error components mapped by the MWMAKE tool can be grouped as follows:

- the random (profile to profile) errors caused by the uncertainties in the previously retrieved pressure and temperature, and VMR of spectrally interfering molecules;

- the systematic error due to horizontal variability of the atmosphere not already treated in the ORM [11];
- the systematic uncertainties in the spectroscopic and cross-section databases;
- the error caused by less than perfect instrument radiometric calibration;
- the errors caused by the less than perfect ILS characterization.

An exhaustive example of MWMAKE error budget will be shown in the discussion about the CCl_4 error characterization (Sect. 6.2.1). Full details about MWMAKE tool can be found in [19] and at the Oxford University MIPAS website [62].

Chapter 5

Phosgene ($COCl_2$)

This chapter is based on the following paper: Valeri, M., Carlotti, M., Flaud, J.-M., Raspollini, P., Ridolfi, M., and Dinelli, B. M.: Phosgene in the UTLS: seasonal and latitudinal variations from MIPAS observations, Atmospheric Measurement Techniques, **9**, *4655–4663*, https://doi.org/10.5194/amt-9-4655-2016, 2016.

The study presented here was performed thanks to the contributions of all the co-authors of the above mentioned paper. Dr. Piera Raspollini discovered the $COCl_2$ *spectral features in the MIPAS spectra and their interference with CFC-11 in MIPAS version 6 products (Sect. 5.1). The new* $COCl_2$ *spectroscopic data (Sect. 5.2) were developed by Prof. Jean–Marie Flaud and his group at the Laboratoire Interuniversitaire des Systémes Atmosphériques (LISA) in Paris (France). Together with Dr. Bianca Maria Dinelli I carried-out the preliminary analyses in order to identify the better retrieval setup for phosgene (Sect. 5.3). I analyzed the* $COCl_2$ *profiles retrieved using the ORM to identify latitudinal and seasonal variations (Sect. 5.4). I also compared our findings to ACE–FTS observations (Sect. 5.5). Prof. Massimo Carlotti and Prof. Marco Ridolfi supervised the whole work and contributed to the preparation of the above mentioned paper.*

Carbonyl chloride ($COCl_2$), better known as phosgene, is a toxic gas. In the 20th century phosgene was mainly used by the chemical industry in the preparation of insecticides, pharmaceuticals and herbicides. Its usage has been reduced over the years due to its high toxicity. The $COCl_2$ global distribution in the UTLS has been determined for the first time from MIPAS measurements. Here we present the vertical distribution of phosgene and its seasonal and latitudinal variations. We also describe newly developed $COCl_2$ spectroscopic information, the setup used for the retrieval and the associated diagnostic data.

5.1 Phosgene in the Earth's atmosphere

Atmospheric phosgene is formed in the troposphere by OH-initiated oxidation of chlorinated hydrocarbons such as *chloroform* ($CHCl_3$), *methylchloroform* (CH_3CC_3), *tetrachloroethylene* (C_2Cl_4) and *trichloroethylene* (C_2HCl_3) [28, 47]. In the stratosphere, it is formed by oxidation of its tropospheric source molecules and by the photochemical decay of CCl_4. Stratospheric phosgene is a weak absorber in the UV region and has a long lifetime (several years); however it is slowly oxidised to form ClO_X. By contrast, the lifetime of phosgene in the troposphere is shorter (about 70 days), because it is rapidly removed by water droplets or by deposition in the oceans [90, 47].

The first study about atmospheric phosgene was made by Singh [90], who studied the surface distribution of phosgene using data from six stations in California. In 1988, Wilson [109] measured phosgene at various altitudes during an aircraft flight over Germany. Toon et al. [99] used the Jet Propulsion Laboratory (JPL) MkIV interferometer, on board stratospheric balloons, to retrieve different VMR profiles of phosgene from 1992 to 2000. The first satellite measurements of stratospheric phosgene have been performed using the ACE-FTS on board the SCISAT-1 satellite. Fu et al. [28] used ACE-FTS measurements in the period between February 2004 and May 2006 to make the first analysis of the global distribution of phosgene. Using data acquired by the same experiment in the years from 2004 to 2010, Brown et al. [5] focused on the study of the trends of the halogen species, including phosgene. In the thermal infrared, phosgene can be measured in the 830–860 cm^{-1} spectral region, corresponding to the ν_5 band of $COCl_2$. However, in the same spectral region, the ν_4 band of CFC–

11 is present. The emission of the CFC–11 ν_4 band is much stronger than the one of $COCl_2$ ν_5 band; therefore phosgene spectral features are hidden by the CFC–11 absorbing band. In the validation phase of MIPAS version 6 products, obtained with the ESA level 2 processor, positive biases were found in the CFC–11 VMR profiles. In particular, CFC–11 profiles were found to be affected by a significant bias at all altitudes and latitudes with respect to MIPAS balloon measurements [58, 107] and Bonbon [85] measurements [23]. While below 19 km this bias was still within the combined systematic and total errors, above this altitude it clearly exceeded this error margin. From the study of the residuals of the CFC–11 retrievals, no particular features emerged but, while checking the atmospheric molecules absorbing in the same spectral range, it was found that $COCl_2$ had not been included in the computation of the simulated spectra. A preliminary test was performed which took into account $COCl_2$ interference in the simulated spectra using the vertical distribution retrieved by ACE-FTS [28] and $COCl_2$ cross sections recorded at 25 °C by Sharpe et al. [86]. The results of this test indicated that the differences in the average retrieved CFC-11 with and without $COCl_2$ included in the simulation were of the order of the bias found in CFC–11 profiles. Therefore, in subsequent retrievals of MIPAS CFC–11, phosgene has been added to the absorber list. The accuracy of the absorption cross section used in MIPAS retrievals is quite good but unfortunately the temperature range of the cross-section measurements is far from being adequate for atmospheric retrievals. This fact triggered the development of new spectroscopic data for phosgene in order to enable a better reproduction of its contribution to MIPAS spectra [49]. Furthermore, the clear interference of phosgene into the CFC–11 signal suggested that MIPAS measurements could be exploited to retrieve phosgene global distribution.

5.2 Spectroscopic data

Phosgene is a heavy molecule with small rotational constants and with a number of low-lying vibrational states. As a consequence, at room temperature its infrared spectrum is extremely dense and almost intractable. Kwabia–Tchana et al. [49] carried out the first detailed and extensive analysis of the 11.75 μm absorption region of phosgene using high-resolution

Fourier transform spectra recorded at the low temperature of 169 K. More precisely the ν_5 bands of the two isotopologues $CO^{35}Cl_2$ and $CO^{35}Cl^{37}Cl$ were assigned up to very high quantum numbers. The upper state rovibrational levels were fitted using Hamiltonian matrices, accounting for resonance effects when necessary. In this way, very satisfactory fits (to within the experimental accuracies) were obtained, leading to very accurate Hamiltonian constants and line positions. Unfortunately it was not possible to firmly assign the corresponding hot bands, which were modelled using extrapolated Hamiltonian constants. The new Hamiltonian constants were used to build the phosgene spectroscopic database used in this work. The line intensities used in our analysis were calculated using single transition moments (no rotational corrections) and calibrated using the cross-section measurements from [86]. Since no measurements of the pressure-broadening coefficients are available, a constant value of $0.8\,cm^{-1}\,atm^{-1}$ for air-broadening and of $0.3\,cm^{-1}\,atm^{-1}$ for self-broadening have been used. The error of the new phosgene spectroscopic database is dominated by the accuracy with which the cross sections have been measured [86].

Previous satellite analysis of phosgene [99, 28] were carried out using the 1995 Atmospheric Trace Molecule Spectroscopy (ATMOS) linelist [7]. To evaluate the difference of the new spectroscopic data with respect to the older database, we have simulated a MIPAS spectrum at 21.2 km tangent altitude for midlatitude atmospheric conditions in the 800–900 cm^{-1} spectral region using the HITRAN_MIPAS_PF_4.45 database (Sect. 3.2, [65]) where the new phosgene lines have been included and repeated the simulation using the same spectroscopic database where the phosgene lines were replaced by those from the ATMOS line list. Fig. 5.1 shows, in the upper panel, the simulated spectrum, while in the middle panel we report the contribution to the spectrum due to phosgene for our database (in red) and for the ATMOS database (in blue). The lowest panel of Fig. 5.1 shows the difference between the two phosgene spectra. The comparison between the two phosgene contributions shows that in the Q-branch region the two databases are in agreement, while higher radiances (about $3\,nW\,(cm^2\ sr\,cm^{-1})^{-1}$) are found for the new phosgene lines in the P and R branches.

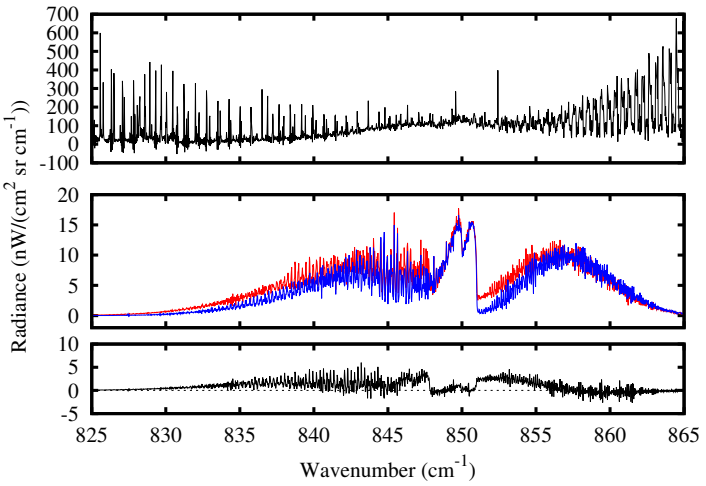

Figure 5.1: Top panel: simulated spectra at 21.2 km tangent altitudes for midlatitude atmospheric conditions in the 825–865 cm^{-1} spectral region using the HITRAN_MIPAS_PF_4.45 database (Sect. 3.2) containing the new phosgene lines. Middle panel: contribution of the new phosgene linelist (red line) and of the ATMOS 1995 phosgene lines (blue line). Bottom panel: difference between the new phosgene linelist and the ATMOS 1995 database.

5.3 Retrieval setup

The retrieval scheme used here is based on the ORM (Sect. 4.6, [76, 72, 73]) upgraded with the multi target retrieval (MTR) functionality [18] and with the possibility of using the OE approach (or maximum a posteriori likelihood, Sect. 4.3, [78]). The MTR functionality gives the possibility to properly take into account the mutual spectral interference between CFC–11 and $COCl_2$ (Sect. 5.1). Moreover, OE enables the quality of the retrieved profiles to be monitored using the individual information gain quantifier described in [17]. This quantifier allows data to be filtered out for which the information extracted from the measurements is below a predefined threshold. The use of OE in the retrievals requires an a priori estimate of both the target profile and of its error covariance matrix. In order to minimise the influence of the a priori information on the observed latitudinal and seasonal variations of the retrieved $COCl_2$ VMR, we used the same a priori profile and covariance matrix for all the retrievals presented in this work. We built the a priori profile of $COCl_2$ by averaging all the IG2 profiles (Fig. 5.2, see Sect. 3.3) for the different latitudinal bands. Since the retrieved phosgene profiles presented in this paper have been averaged using a common pressure grid, we tabulated the a priori $COCl_2$ profile onto the same pressure grid. This makes the a priori profile of $COCl_2$ different for each retrieval when represented as a function of the altitude coordinate, but makes its shape invariant as a function of pressure. To build the a priori covariance matrix we assumed a $COCl_2$ variability equal to 80 % of the a priori profile, plus a constant absolute error of 10 pptv. Moreover, in order to introduce a weak vertical constraint in the retrieved $COCl_2$ profiles, for the calculation of the a priori covariance matrix we assumed a vertical correlation length of 5 km [95].

MWMAKE [19] was used to select a set of MWs optimized for the retrieval of the $COCl_2$ VMR profile as a single target. With these MWs, $COCl_2$ was individually retrieved after the sequential retrieval of the following targets: tangent pressure, temperature and the VMR of H_2O, O_3, HNO_3, NO_2, CFC-11, CFC-12, HCFC-22. This approach, however, did not provide satisfactory results since it produced a double-peaked artifact at low altitudes in the zonally averaged $COCl_2$ VMR profiles. Tests showed that this artifact was due to the mutual spectral interference between $COCl_2$ and

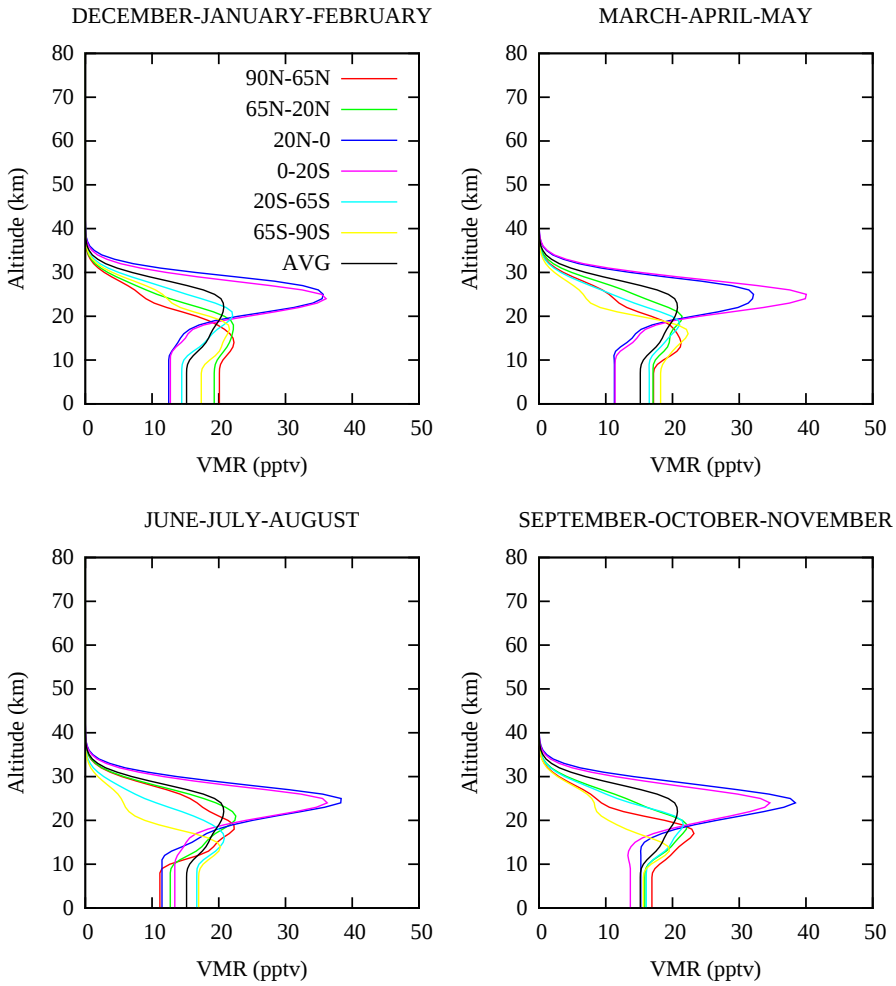

Figure 5.2: The $COCl_2$ IG2 version 4.1 climatological profiles for winter (upper left), spring (upper right), summer (lower left) and autumn (lower right) 2008. For each season, polar north (red lines), mid-latitude north (green lines), tropical north (blue lines), tropical south (violet lines), mid-latitude south (cyan lines) and polar south (yellow lines) climatological profiles are reported. The average profile (black lines) has been calculated considering both latitude bands and seasons.

CFC–11 [45]. As already said in Sect. 5.1, such a strong interference had already been highlighted in the validation phase of MIPAS CFC-11 version 6 profiles. Even if CFC–11 was retrieved from the same scan in a previous step of the retrieval chain, the error affecting the retrieved profile was large enough to produce the unrealistic artifact. Therefore we decided to account

Starting wavenumber (cm^{-1})	Ending wavenumber (cm^{-1})
815.6875	818.6875
818.7500	821.7500
836.6875	839.6875
839.7500	842.7500
842.8125	845.8125
846.9375	849.9375
850.2500	853.2500
857.1875	860.1875

Table 5.1: MWs selected for MTR retrievals of $COCl_2$ and CFC–11.

for the spectral interference between $COCl_2$ and CFC-11 by exploiting the MTR capability of our code to simultaneously retrieve both gases. We used MWMAKE to identify optimized MWs for the joint $COCl_2$ and CFC-11 retrieval. The resulting MWs are listed in Table 5.1.

The joint $COCl_2$ and CFC–11 retrieval assumes the profiles obtained from the sequential retrieval of the following targets: p, T and VMR of H_2O, O_3, HNO_3, NO_2, CFC-11, CFC-12, HCFC-22. With this retrieval setup, artifacts and non-physical features disappeared from the retrieved $COCl_2$ profiles. Moreover the retrieval error now properly takes into account the correlation between $COCl_2$ and CFC–11 VMR profiles, which is quantified by the off-diagonal elements of the covariance matrix of the retrieval [18]. For the CFC–11 MTR analysis we used the same vertical retrieval grid adopted in the single target retrieval with the IG2 profile used as initial guess and a priori profiles with a covariance matrix set to 80 % of the profile value. The correlation length for CFC-11 was the same used for phosgene. Differences between the CFC-11 retrieved in the previous step of the retrieval chain (assuming phosgene in climatological abundance) and simultaneously to phosgene were small, well within the noise error.

The main components of the resulting $COCl_2$ error budget estimated by MWMAKE (Sect. 4.6.5, [19]) are shown in Fig. 5.3. The total random component of the systematic error was calculated as the quadratic summation of all the errors that vary randomly from profile to profile. In our case this error includes uncertainties in temperature, pressure and interfering species that are not retrieved. The total systematic error was calculated as the quadratic summation of the errors that provide almost constant contribution to the total budget; therefore they produce a bias in the results. These

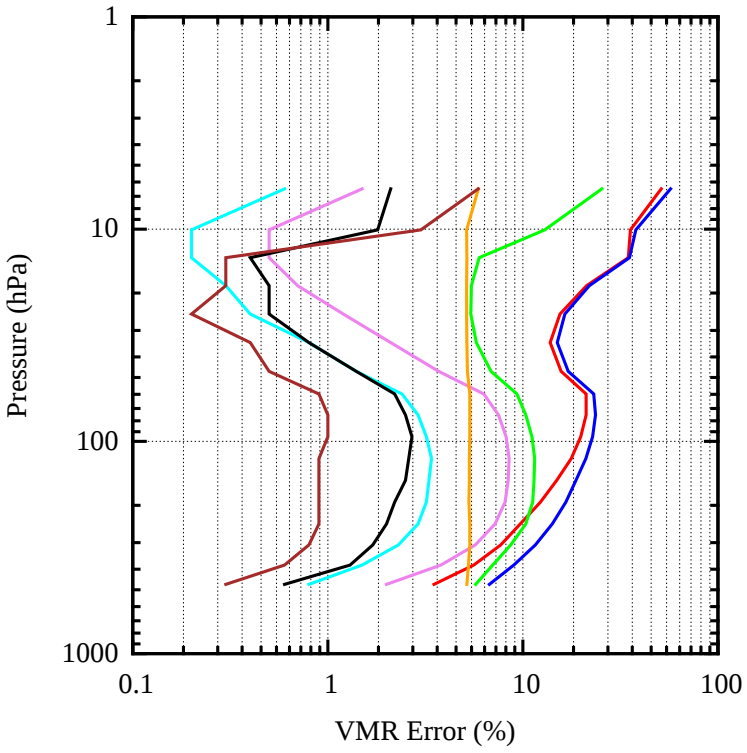

Figure 5.3: Error analysis of the joint $COCl_2$ and CFC-11 retrieval: the total error (blue), the total systematic error (green) and the total random error (red). We also report the uncertainties due to temperature (violet), pressure (cyan), spectroscopic database (orange-red), intensity calibration (black) and to the width of the instrument line shape (brown) for the phosgene VMR.

errors are the uncertainties in the spectroscopic database, in the radiometric calibration of the measured spectra and in the parameterization of the width of the instrumental line shape. The contribution of the new phosgene line list to the spectroscopic error was calculated considering the uncertainties in the line intensities (3–5 %, we have conservatively assumed an error of 5 %) and in the air-broadening coefficients (20 %). We have considered that an error of 5 % in the line intensity leads to an error of the same percentage in the retrieved VMRs since the phosgene absorption is in the linear region. An uncertainty of 20 % in the air-broadening coefficients produces an error of about 1 % in the phosgene cross sections computed at an average stratospheric temperature and pressure. We have assumed that on average the retrieved VMRs will be affected by a similar error. In Fig. 5.3 we report (orange) the final spectroscopic error resulting from the quadratic summation of the uncertainties due to the spectroscopic data of the other molecules (estimated by MWMAKE) and the phosgene spectroscopic errors reported above. In Fig. 5.3 we also report (blue) the total error obtained as the quadratic summation of the total systematic and random error components.

5.4 Results

An objective of this work is to demonstrate the feasibility of the phosgene retrieval from MIPAS spectra. Therefore, due to the computing resources required by a full mission retrieval, we considered adequate the use of a reduced data set. The analysis was performed using MIPAS Level 1B data Version 5, in which only a time-independent correction of detector nonlinearities was applied. Since nonlinearities change as the detector ages, this choice implies a calibration error drifting along the mission. The systematic calibration drift error prevents to study phosgene atmospheric trends. Therefore in this work we focus on the study of possible seasonal and latitudinal variations of $COCl_2$. We processed all MIPAS measurements acquired on days 18 and 20 of each month of 2008 when MIPAS was measuring in the NOM observation mode (in 2008 this mode was used for 80 % of the time). In total we retrieved more than 28 000 profiles.

In the left panel of Fig. 5.4, we report the typical phosgene AKs (Sect. 4.5) relative to a profile retrieved from a limb scan acquired on 18 March 2008 and geolocated at 31° N/75° W. The plot shows the sensitivity of

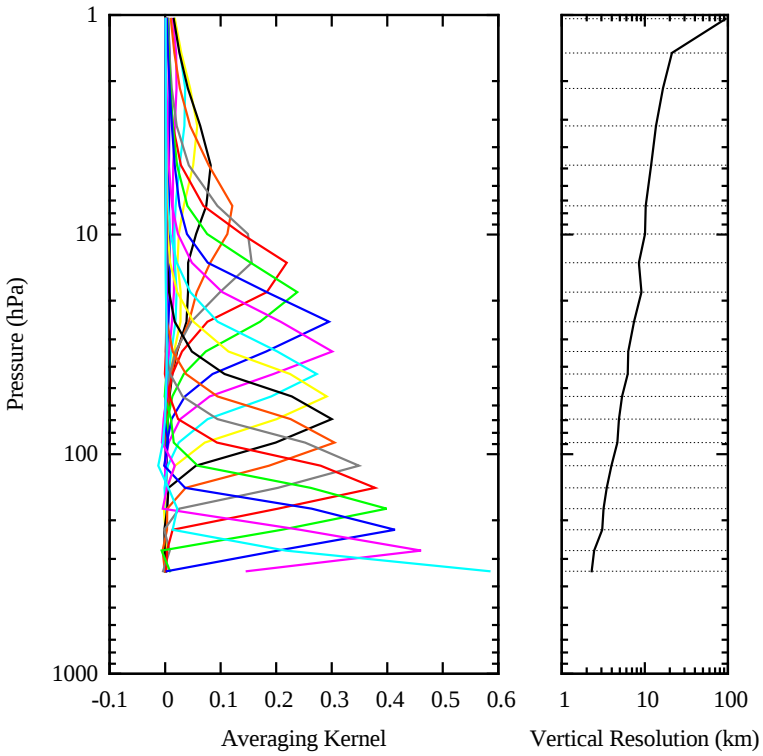

Figure 5.4: Typical phosgene averaging kernels (left panel) and vertical resolution (right panel). In the left panel each colour represents a row of the averaging kernel matrix. In the right panel we have also reported the pressure levels used for the retrieval. The plots refer to the retrieval from a MIPAS limb scan acquired on 18 March 2008, 31° N/75° W.

the retrieved profile to variations of the same gas VMR at pressure levels in the UTLS region. From the analysis of all the averaging kernels of the retrievals we can deduce that our analysis has a high sensitivity between 10 and 400 hPa. Above 10 hPa the AKs are less peaked, indicating lower sensitivity. In the right panel of Fig. 5.4 we plot, for the same AKs, the vertical resolution computed as the FWHM of the rows of the AK. We note that in the altitude region with high sensitivity (10–400 hPa) the vertical resolution ranges from 3 to 10 km while above 10 hPa it becomes larger.

The final data set was filtered by selecting only the profile data points for which a significant amount of information was extracted from the measurements. This was done using an information gain threshold of 0.3. This means that the a priori error is reduced in the analysis by a factor of about 1.2. After filtering, the final set of data was divided into four groups according to their measurement dates: JJA, SON, DJF and MAM (Tab. 3.2). For each season, we calculated the average phosgene profile in the IG2 latitudinal bands (Tab. 3.1). Since the MIPAS vertical sampling grid (coinciding with the retrieval grid) is not constant along the orbit, we first linearly interpolated each individual retrieved profile on a fixed pressure grid in log pressure, then we computed the averages.

In Fig. 5.5 we report, for 10° latitude bins and each season, the average number of DOFs (solid lines) and the corresponding average number of altitudes at which the phosgene profile is retrieved (dashed lines). The two curves show a reduction of the number of DOFs and of the number of retrieval altitudes in the tropical region for all seasons. This is caused by the presence of high-altitude clouds typical of this region. Clouds are in fact detected by the Level 2 preprocessor with a cloud-filtering algorithm [72, 73] and the spectra flagged as "cloudy" are excluded from the analysis. The only noticeable seasonal dependence of the number of DOFs is in the polar regions. In the figure we also see that in JJA at the South Pole there is a significant reduction in both the number of retrieved profile altitudes and DOFs. This is due to the presence of polar stratospheric clouds (PSCs) detected and filtered out by the cloud detection algorithm.

Figure 5.6 shows the average VMR profiles of phosgene for the latitudinal bands and seasons described above. The plots in this figure do not show evident seasonal variability in the vertical distribution of phosgene in the middle and tropical latitude bands, in agreement with the discussion of [47].

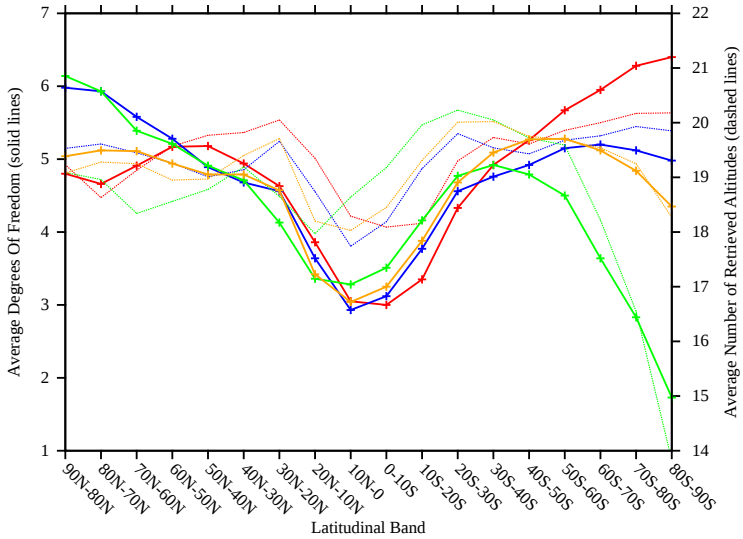

Figure 5.5: Average phosgene degrees of freedom (DOF, solid lines) and average number of retrieved altitudes (dashed lines) for DJF (red lines), MAM (blue lines), JJA (green lines) and SON (orange lines). Averages are calculated for 10° latitude bins.

We only observe a weak seasonality in the polar regions. The reduction of phosgene observed at both poles during winter and spring is probably related to both the subsidence of stratospheric air due to the presence of the polar vortex and the reduction of phosgene formation rate due to photolysis. The average profiles show a clear latitude dependence. Actually, in the polar and midlatitude regions the average profiles do not exceed 30 pptv and they do not show evident peaks. By contrast, at the tropical latitudes, the vertical VMR distributions show peak values close to 40 pptv located at lower pressure levels (30/40 hPa) with respect to the other regions. In Fig. 5.7 we show the zonal averages (for 10° latitude bins) of phosgene VMR, for each season of the year 2008. These maps highlight the latitudinal dependence of the phosgene distribution in the UTLS region. The symmetric pattern in which VMR values decrease moving from the equator to the poles is caused by the Brewer–Dobson circulation, which transports the tropical phosgene poleward. The equatorial bulk in the distribution of the $COCl_2$ is caused by the greater insolation at the tropics compared to the higher latitudes [28].

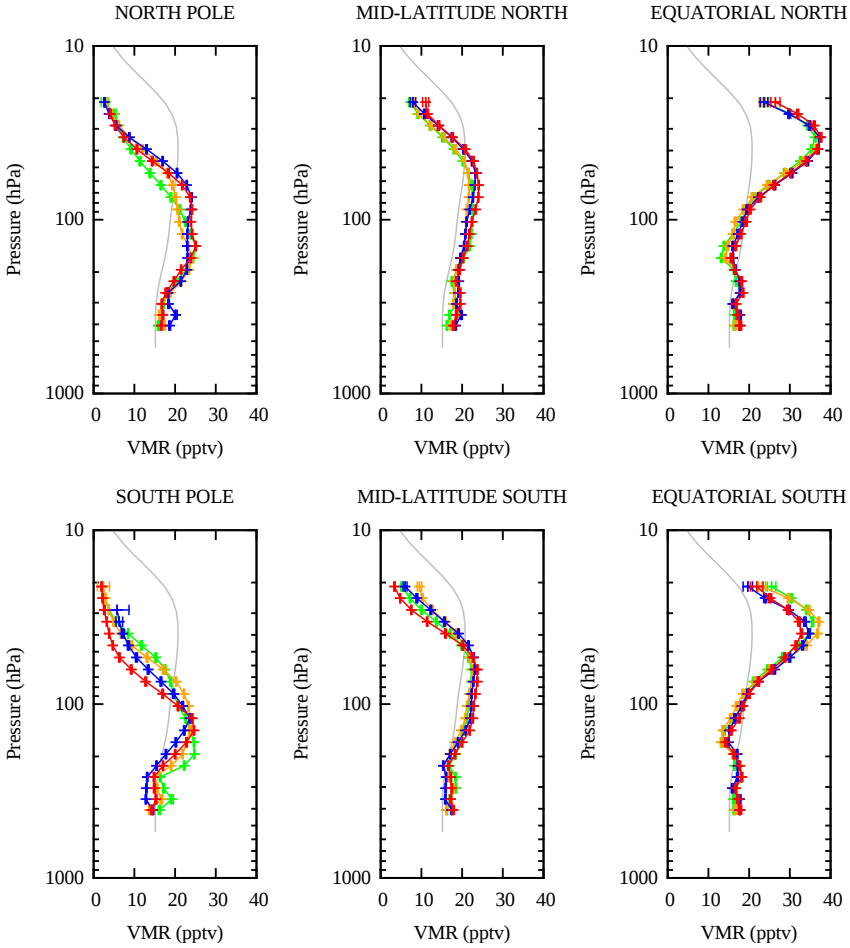

Figure 5.6: Average phosgene VMR profiles for DJF (green lines), MAM (orange lines), JJA (blue lines) and SON (red lines). Averages are calculated for North Pole (90–65° N, top left), midlatitude north (65–20° N, top centre), equatorial north (20–0° , top right), South Pole (65–90° S, bottom left), midlatitude south (20–65° S, bottom centre) and equatorial south (0–20° S, bottom right). We also report the a priori profile (solid grey lines) based on the existing climatology. This profile does not reproduce the observed geographical variability.

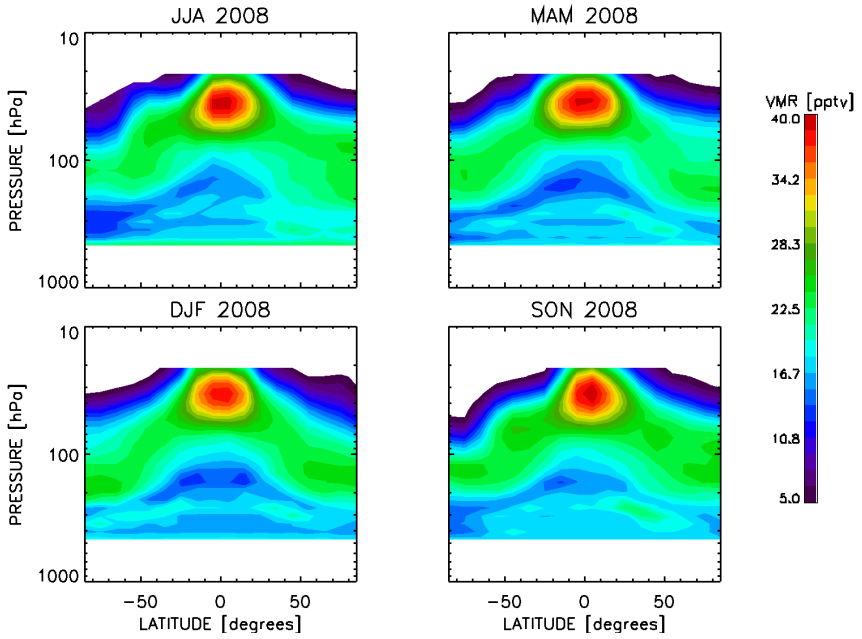

Figure 5.7: Zonal average phosgene VMR for JJA (top left), MAM (top right), DJF (bottom left) and SON (bottom right) 2008. Averages are calculated for 10° latitude bins.

5.5 Comparison with ACE-FTS measurements

To validate our results we used the phosgene data contained in version 3.5 of the measurements of the ACE-FTS instrument [2]. ACE-FTS is a solar occultation limb sounder onboard SciSat since 2004. It exploits the solar occultation technique to make measurements in the spectral interval between 750 and 4400 cm^{-1}, with a spectral resolution of 0.02 cm^{-1}. Several target atmospheric parameters are routinely retrieved from ACE-FTS measurements. Among them, temperature, pressure, and the VMR profiles of over 30 atmospheric trace gases and over 20 subsidiary isotopologues. Profiles are retrieved in the range from $\sim$ 5 to 150 km, with a vertical field of view of $\sim$ 3-4 km and a vertical sampling of 2-6 km. The ACE-FTS retrieval algorithm is described in [3], and the updates for the most recent version of the retrieval, version 3.5, are detailed in [4]. The retrieval algorithm uses a non-linear least-squares global-fitting technique that fits the ACE-FTS observed spectra in given MWs with forward modelled spectra based on line strengths and line widths from the HITRAN 2004 database [80] (with

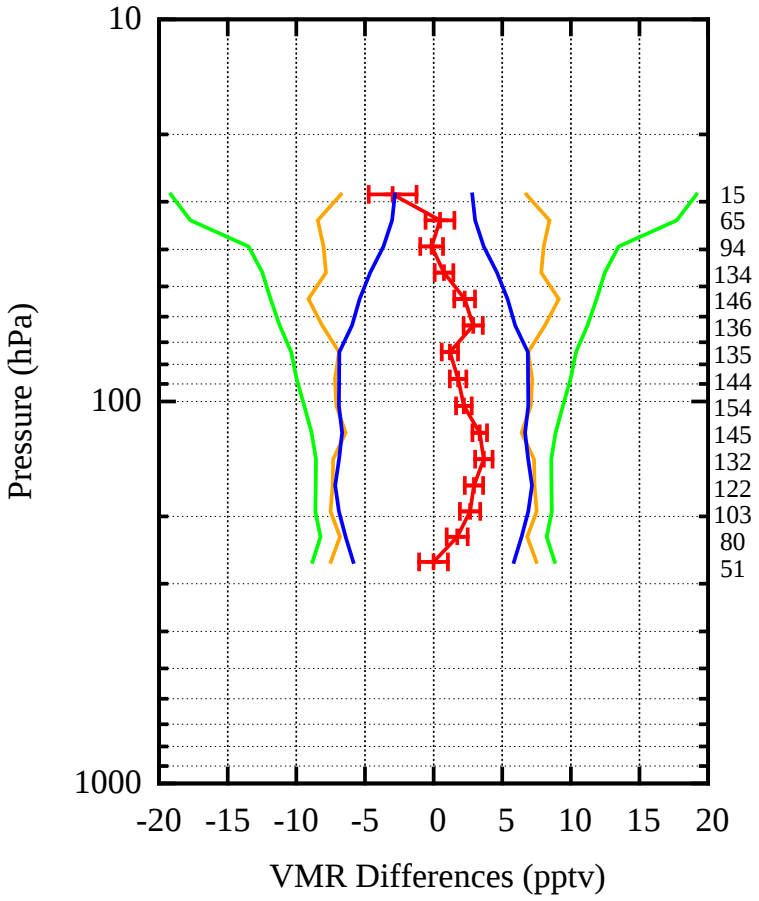

Figure 5.8: Average difference profile between the co-located MIPAS and ACE-FTS measurements (red line) with standard deviation of the mean (red error bars). The standard deviation of the difference (orange lines), the total random error (green lines), the total systematic error of the difference (blue lines) are also reported. The number of co-located pairs for each pressure level is reported on the right side of the plot.

updates as described by Boone et al. [4]).

Out of the whole ACE-FTS data set we selected the phosgene VMR profile co-located with the MIPAS measurements used in our analysis. The co-location criteria were 5° maximum difference in latitude and longitude and a maximum difference of 6 h in the acquisition time. In total we found about 150 coincidences. The ACE profiles were linearly interpolated in log pressure onto the same pressure grid used to calculate our averages. To remove unrealistic values we have filtered out the points of the ACE-FTS profiles for which the values exceeded the average value by more than 3 times the standard deviation. MIPAS data were filtered with the same criterion described in Sect. 5.4. We computed the differences between MIPAS and ACE-FTS co-located profiles and in Fig. 5.8 we report their average (red line). On the same figure we report the combined systematic error of the difference (blue lines), obtained as the square root of the sum of the squared systematic errors of each instrument. The percentage systematic error of the individual instruments was assumed constant for all the pressure levels and equal to 13 % of the phosgene VMR value for MIPAS (an average value of the estimated systematic errors reported in Fig. 5.3) and, as reported in [28], 30 % of the VMR value for ACE-FTS. The average difference shown in Fig. 5.8 is consistent with zero, considering its combined systematic error (blue line) and the standard deviation of the mean (represented by the red line error bar in the figure) [103]. This suggests that MIPAS and ACE-FTS phosgene retrievals are in good agreement. The random error of the difference (green lines in Fig. 5.8) is calculated as the square root of the sum of the squared random errors of MIPAS and ACE-FTS. This error should mimic the standard deviation of the differences (yellow lines in Fig. 5.8). We see that the two error estimates are in good agreement below 50 hPa. Given the relatively small number of MIPAS and ACE-FTS co-located measurements it was not possible to perform the comparison of the two instruments on separate latitude bands and seasons.

Chapter 6

Carbon tetrachloride (CCl_4)

This chapter is based on the following paper: Valeri, M., Barbara, F., Boone, C., Ceccherini, S., Gai, M., Maucher, G., Raspollini, P., Ridolfi, M., Sgheri, L., Wetzel, G., and Zoppetti, N.: CCl_4distribution derived from MIPAS ESA v7 data: intercomparisons, trend, and lifetime estimation, Atmospheric Chemistry and Physics, **17**, *10143–10162*, https://doi.org/10.5194/acp-17-10143-2017, 2017.

The study presented here was performed thanks to the contributions of all the co-authors of the above mentioned paper. Dr. M. Gai and Prof. M. Ridolfi evaluated the quality of the fits obtained in CCl_4 *retrievals (Sect. 6.2.1). Together with Dr. P. Raspollini, I studied the* CCl_4 *VMR distribution in the UTLS, its features and its seasonal variability (Sect. 6.3). Dr. G. Wetzel and Dr. G. Maucher compared MIPAS/ENVISAT results with those obtained using MIPAS-B measurements (Sect. 6.4.1). Dr. C. Boone, Dr. P. Raspollini, Dr. N. Zoppetti, Dr. S. Ceccherini and Mr. F. Barbara performed the comparison between MIPAS/ENVISAT and ACE–FTS measurements (Sect. 6.4.2). I compared MIPAS* CCl_4 *distribution with* CCl_4 *data derived from EMAC model simulations (Sect. 6.5). I estimated the trend of* CCl_4 *distribution as a function of both altitude and latitude (Sect. 6.6) and I compared MIPAS* CCl_4 *trends with those estimated using ACE–FTS and global surface networks measurements (Sect. 6.6.2). I calculated the atmospheric lifetime of the* CCl_4 *using an approach based on the tracer–tracer linear correlation in the lower stratosphere (Sect. 6.7). Dr. P. Raspollini and Prof. M. Ridolfi supervised the whole work and contributed to the preparation of the above mentioned paper.*

CCl_4 atmospheric emissions are regulated by the Montreal Protocol due to its role as a strong ozone-depleting substance. This molecule has been the subject of recent increased interest as a consequence of the so called "mystery of CCl_4", the discrepancy between atmospheric observations and reported production and consumption. Surface measurements of CCl_4 atmospheric concentrations have declined at a rate almost three times smaller than its lifetime-limited rate, suggesting persistent atmospheric emissions despite the ban. In this chapter, we study CCl_4 zonal distribution in the upper troposphere and lower stratosphere, its trend, and its stratospheric lifetime using MIPAS Level 2 data Version 7.

6.1 Carbon tetrachloride in the Earth's atmosphere

CCl_4 is a strong ozone-depleting substance with an ozone depletion potential of 0.72 and a strong greenhouse gas with a 100-year global warming potential of 1730 [33]. Regulated by the Montreal Protocol, the production of CCl_4 for dispersive applications was banned for developed countries in 1996, while developing countries were allowed a delayed reduction with the complete elimination by 2010 [53]. CCl_4 can still be legally used as a feedstock, for example in the production of hydro-fluorocarbons. CCl_4 natural emissions are not completely understood, which yields some uncertainty on the magnitude of their contributions. Stratosphere-troposphere Processes and their Role in Climate (SPARC) community [93] has recently defined an upper limit of the natural emissions (based on the analysis of old air in firn snow) of 3-4 Gg yr^{-1} out of a total emission estimation of 40 (25-55) Gg yr^{-1}.

The dominant loss mechanism for atmospheric CCl_4 is through photolysis in the stratosphere. The other major sinks are degradation in the oceans and degradation in soil. The estimated partial lifetimes provided in the latest ozone assessment report [10] with respect to these three sinks are 44 years for the atmospheric sink, 94 years for the oceanic sink, and 195 years for the soil sink. The combination of these three partial loss rates yields a total lifetime estimate of 26 years.

CCl_4 atmospheric concentration is routinely monitored by global networks such as Advanced Global Atmospheric Gases Experiment (AGAGE, `http://agage.mit.edu/`, [89, 70, 71]) and National Oceanic and Atmo-

spheric Administration / Earth System Research Laboratory / Halocarbons & other Atmospheric Trace Species (NOAA / ESRL / HATS, `http://www.esrl.noaa.gov/gmd/hats/`). The concentration of CCl_4 has been decreasing in the atmosphere since the early 1990s, and the latest ozone assessment report [10] indicates that the global surface mean mole fraction of CCl_4 continued to decline from 2008 to 2012. AGAGE and University of California Irvine (UCI) networks report rates of decline of 1.2–1.3 % yr^{-1} from 2011 to 2012, whereas the rate of decline reported by the NOAA/HATS network was 1.6 % yr^{-1}. These relative declines in mole fractions at the Earth's surface are comparable to declines in column abundances of 1.1–1.2 % yr^{-1} [5, 77].

A significant discrepancy is observed between global emissions estimates of CCl_4 derived by reported production and feedstock usage (bottom-up emissions) compared to those derived by atmospheric observations (top-down emissions). This discrepancy has recently stimulated a particular interest in furthering the understanding of atmospheric CCl_4. A study performed with a 3-D CCM using the observed global trend and the observed inter-hemispheric gradient (IHG, 1.5 ± 0.2 ppt for 2000–2012) estimated a total lifetime of 35 years [53]. Recently, a study has reassessed the partial lifetime with respect to the soil sink to be 375 years [75], and another study has reassessed the partial lifetime with respect to the ocean sink to be 209 years [8]. These new estimates of the partial lifetimes with respect to soil and oceanic sinks produce a new total lifetime estimate of 33 years, consistent with the estimate given in [53]. This longer total lifetime reduces the discrepancy between the bottom-up and top-down emissions from 54 Gg yr^{-1} to 15 Gg yr^{-1} [93]. While the new bottom-up emission is still less than the top-down emission, the new estimates reconcile the CCl_4 budget discrepancy when considered at the edges of their uncertainties. A recent study estimated that the average European emissions for 2006–2014 were 2.3 Gg yr^{-1} [31], with an average decreasing trend of 7.3% per year.

Since the atmospheric loss of CCl_4 is mainly due to photolysis in the stratosphere, satellite measurements that provide vertical profiles are particularly useful in validating the stratospheric loss rates in atmospheric models. A global distribution of CCl_4 extending up to the mid-stratosphere was obtained by ACE-FTS [1]. This study derived an atmospheric lifetime of 34 years through correlation with CFC-11. Another study using ACE-FTS

measurements in [5] estimated the CCl_4 atmospheric lifetime to be 35 years. A trend of atmospheric CCl_4 from ACE-FTS measurements was reported in [6], averaged in the 30° S-30° N latitude belt and in the altitude range from 5 to 17 km, where it was found to be decreasing at a rate of 1.2% yr^{-1}.

6.2 Retrieval setup

The ORM (ESA Level 2 processor version 7, Sect. 4.6) retrieves CCl_4 VMR profiles from MIPAS measurements simultaneously with a set of other target parameters. As for all MIPAS ESA retrievals, the MWs for CCl_4 retrievals are selected with the MWMAKE algorithm [19]. The MWs used in the retrievals from nominal FR and OR measurements are listed in Tab. 6.1.

Starting wavenumber (cm^{-1})	Ending wavenumber (cm^{-1})
Full Resolution (FR) Phase	
796.3750	799.3750
800.2750	803.2750
792.7000	795.7000
771.8000	773.7750
Optimized Resolution (OR) Phase	
792.8125	795.8125

Table 6.1: MWs used for CCl_4 retrieval from nominal FR and OR MIPAS measurements.

CCl_4 VMR is retrieved only up to about 27 km, since above this altitude the CCl_4 concentration is too small to generate a sufficient contribution to the measured spectrum for analysis. Moreover OR measurements sample the limb with a vertical step of 1.5 km, significantly finer than the instrument FOV (≈3 km, Sect. 2.2). For this reason, to avoid numerical instabilities due to oversampling, in the inversion of OR measurements the retrieval grid includes only one out of every two tangent points. Fig. 6.1 characterizes a typical CCl_4 retrieval from NOM limb scans acquired in the FR (top panel) and OR (bottom panel) measurement phases. The coloured solid lines show the rows of the AKs, each row corresponding to a retrieval grid point (8 grid points for FR and 7 for OR retrievals). Typically the number of DOF of the retrieval is 5–6 for FR and 4–5 for OR measurements. The slightly smaller number of DOF obtained in the OR retrievals stems from the fact that, to

make the retrieval more stable, CCl_4 is not retrieved at every tangent point of the OR limb measurements. The dotted red line of Fig. 6.1 represents the vertical resolution, calculated as the FWHM of the AK rows.

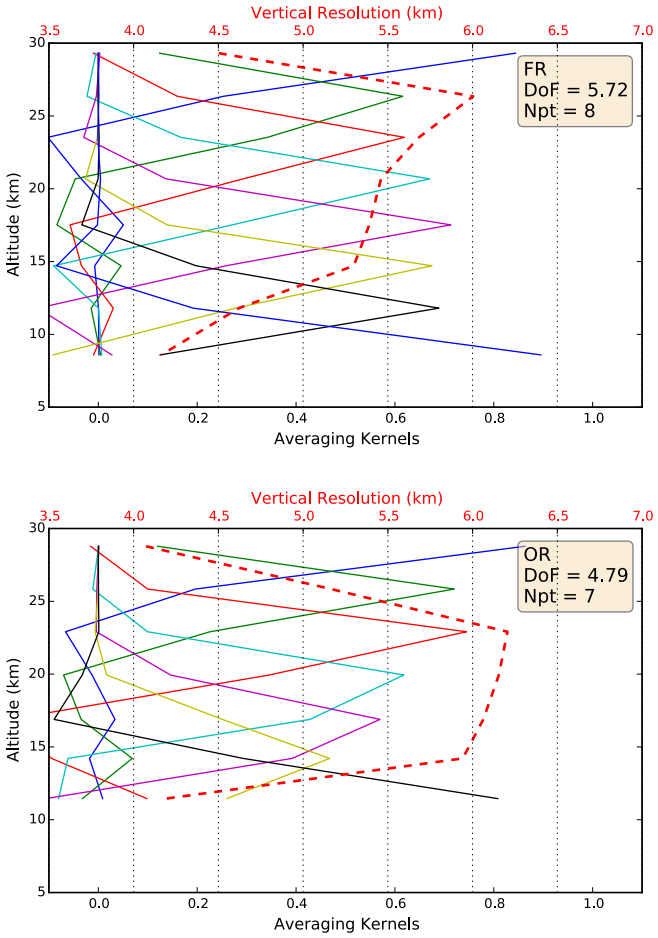

Figure 6.1: Typical AKs (coloured solid lines) and vertical resolution (red dotted lines) of CCl_4 VMR retrieved from FR (top panel) and OR (bottom panel) MIPAS measurements. The vertical resolution is calculated as the FWHM of the AK rows. The plot's key shows also the average number of DOF of the retrieval (trace of the AK matrix) and the number of retrieval grid points (Npt).

6.2.1 Error budget

To evaluate the CCl_4 VMR error due to the mapping of the measurement noise in the retrieval we use the error covariance matrix provided by the retrieval algorithm [12]. The other error components affecting the individual CCl_4 VMR profiles are evaluated using the MWMAKE tool [19]. Fig. 6.2 summarizes the most relevant error components affecting each individual retrieved CCl_4 profile, using the MWs of Tab. 6.1, for both the FR (top panel) and OR (bottom panel) NOM MIPAS measurement cases.

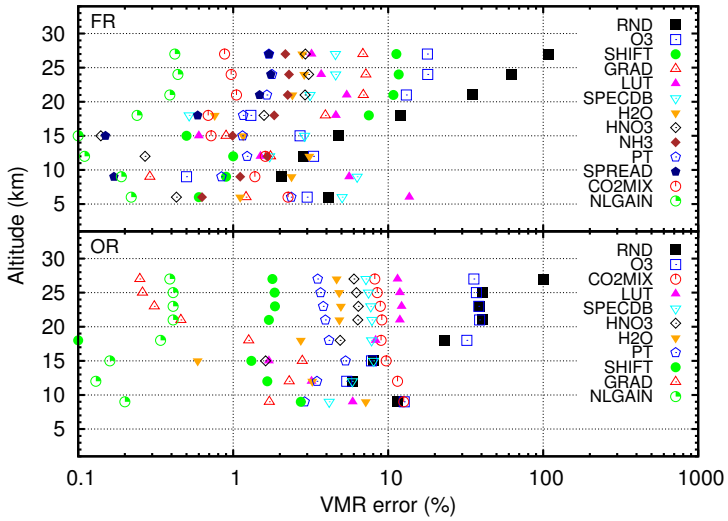

Figure 6.2: Main error components of the individual retrieved CCl_4 VMR profiles from FR (top) and OR (bottom) nominal MIPAS measurements.

The key "RND" in the plots refers to the mapping of the measurement noise in the retrieval, as evaluated for typical FR and OR retrievals. Apart from the "NLGAIN" error that will be discussed later, the other error components, in both the FR and OR cases, can be grouped as follows: a) the errors due to the uncertainties in the (previously retrieved) pressure and temperature profiles (PT), and VMR of spectrally interfering gases, for example O_3, H_2O, HNO_3 and NH_3; b) the error due to horizontal variability of the atmosphere (GRAD) not included in the model; c) the uncertainties in the spectroscopic (SPECDB) and cross-section (LUT) databases and the error in the CO_2 line mixing model (CO2MIX); d) the errors due to less than perfect instrument line-shape characterization, namely its spectral shift (SHIFT) and width (SPREAD). For the details on how the different

error components were calculated by MWMAKE, see [19] and the Oxford University MIPAS website [62].

The main errors of type a) are due to interfering gases whose VMRs are retrieved before CCl_4 with some random error. Therefore, like the RND error component, they change randomly from profile to profile. Thus, in the calculated (monthly) averages they scale down with the inverse square root of the number of averaged profiles. The errors of type b), as shown in [11], cause systematic (and opposite in sign) differences between profiles retrieved from measurements acquired in the ascending and the descending parts of the satellite orbits. These errors largely cancel out when calculating averages that evenly include profiles retrieved from measurements belonging to the ascending and the descending parts of the orbits. Errors of type c) are constant and may cause profile biases but have no effect on calculated trends. Regarding the errors due to the imperfect instrument line-shape modeling (type d), since the gain of MIPAS bolometric detectors remained constant throughout the whole mission, there is no hint of a possible degradation of instrument optics and thus of a possible change in the instrument line-shape. This type of error, therefore, has no impact on the trend calculation.

Imperfect instrument radiometric calibration also causes an error. This error is plotted in Fig. 6.2 with the label "NLGAIN". Being of the order of 0.4% in the upper part of the retrieval range, it is rather small in individual CCl_4 profiles. Although small, this error is important when calculating atmospheric trends as it includes the uncertainty in the correction applied to the radiances to account for the non-linearities of MIPAS photometric detectors [48]. In MIPAS Level 1B radiances up to version 5, the applied non-linearity correction is constant throughout the whole MIPAS mission. However, non-linearities change over the course of the mission due to progressive ageing of the detectors. A constant correction implies, therefore, a drift of the radiometric calibration error during the mission, with a direct impact in the calculated trends. MIPAS Level 1B radiances version 7 overcome this problem as they use a time-dependent non-linearity correction scheme. The residual drift of the calibration error after this time-dependent correction is still being characterized; however, preliminary results show that it is smaller than 1% across the entire mission. MIPAS Level 1B radiances version 5 were used in the past to extract information on trends of different gases, either ignoring this effect (see, e.g., CFC-11/CFC-12 in [45], or

HCFC-22 in [15]) or correcting the drift via intercomparison with other instruments assumed to be drift-free [21]. Recently it has been shown that ignoring this effect introduces a significant error on the trend estimation [20]. The MIPAS Level 1B calibrated radiances version 7 employed here are considered to be a significant improvement from the point of view of the correction of this drift.

The generally good quality of fits obtained in CCl_4 retrievals is illustrated in Fig. 6.3. The figure refers to the MWs used in the FR retrievals. We do not show the residuals in the single MW used for OR retrievals as it mostly overlaps the third MW of FR retrievals. The upper plot of Fig. 6.3 shows the average of 1141 observed (black dots) and simulated (red line) limb radiances in the MWs used for CCl_4 retrievals. The averages include spectra with tangent heights in the range from 6 to 17 km. The lower plot shows the average residuals of the fit (observation minus simulation, blue line) as well as the average noise level of the individual MIPAS measurements (dashed lines). The grey areas indicate spectral channels that, as recommended by the MWMAKE algorithm, are excluded from the fit to minimize the total retrieval error. Note that the average residuals shown in Fig. 6.3 have an associated random error given by the noise of the individual measured spectra divided by the square root of the number of averaged spectra, i.e. $\approx 1\text{nW}/(\text{cm}^2\text{sr}\,\text{cm}^{-1})$. This implies that while the magnitude of the average residuals is incompatible with their noise error, the additional systematic uncertainties are still smaller than the noise error of the individual measured spectra, in agreement with the predictions reported in Fig. 6.2.

6.3 Global distribution

Fig. 6.4 shows the global monthly distribution of MIPAS CCl_4 VMR for a representative month from each of the four seasons, spanning the time period from August 2010 through May 2011. Here, retrieved profiles were first interpolated to fixed pressure levels, and then binned in 5° latitude intervals (for more details see Sect. 6.5.2). In all the considered months, the zonal averages show the typical shape of long-lived species of anthropogenic origin, which are emitted at the surface and destroyed primarily in the stratosphere. Larger values are found in the troposphere, and then the VMR monotonically decreases with increasing altitude in the stratosphere.

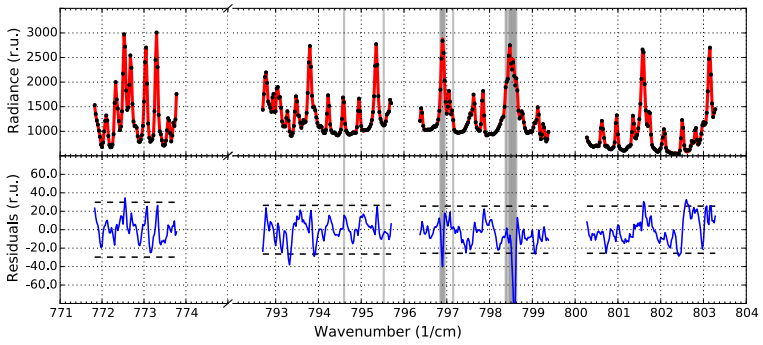

Figure 6.3: The upper plot shows an average of 1141 observed (black dots) and simulated (red line) limb radiances in the MWs used for CCl_4 FR retrievals. The averages include spectra with tangent heights from 6 to 17 km.The lower plot shows the average residuals of the fit (blue line, observation minus simulation) as well as the average noise level of the individual measurements (dashed lines). The grey areas indicate spectral channels excluded from the fit. The radiance units (r.u.) in the vertical axes of the plots are $\mathrm{nW/(cm^2 sr\,cm^{-1})}$.

In the lower stratosphere, concentrations between 30° S and 30° N are significantly larger compared to those at higher latitudes. This pattern can be attributed to the Brewer-Dobson circulation that is responsible for the uplift of the surface air in the tropical regions.

The maps in Fig. 6.5 show the time evolution of CCl_4 at all latitudes from July 2002 to April 2012. The three maps refer to different pressure levels: 50 hPa (upper map), 90 hPa (middle map) and 130 hPa (lower map). The CCl_4 time evolution maps show a seasonal variability. The intrusion of CCl_4-poor mesospheric air in the stratosphere during winter, due to the air subsidence induced by the polar vortex, is clearly visible in both polar winters, its effects continuing into early spring and extending into the troposphere. Minimum CCl_4 values are observed in November at the South Pole and in March at the North Pole (November is considered the beginning of spring at the South Pole, whereas spring begins in March at the North Pole). This was previously observed for other long lived anthropogenic species [45]. The effect is larger in the Antarctic due to the stronger, more stable polar vortex. Modulated by this seasonal variability, at all altitudes a constant trend and an inter-hemispherical difference can also be observed and are further analysed in the subsequent figures. We also note that for

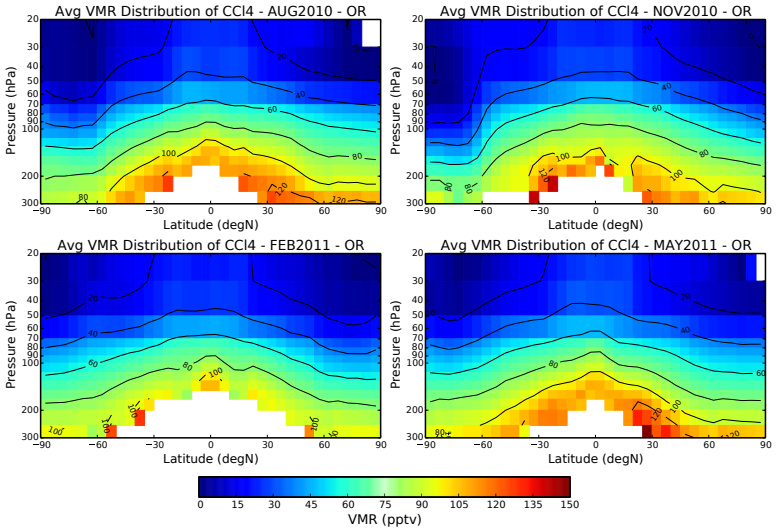

Figure 6.4: Zonal monthly averages of MIPAS CCl_4 profiles. The maps refer to four separate months in different seasons: August 2010 (top left), November 2010 (top right), February 2011 (bottom left) and May 2011 (bottom right).

pressures larger than 100 hPa, the CCl_4 measured in the OR phase has a positive bias with respect to that measured in the FR phase. This bias, discussed also in Sect. 6.4.1, may be due to the different MWs used for the retrieval in the two mission phases, or to the different limb sampling patterns adopted.

The IHG at the surface is largely used as a qualitative indicator of continuous emissions [54, 53]. Anthropogenic emissions are larger in the Northern Hemisphere (NH) [93] and the transport of these emissions from the NH to the Southern Hemisphere (SH) takes about one year, i.e. a time interval much shorter than the CCl_4 lifetime (Sect. 6.7). Hence, a significant IHG in the CCl_4 distribution represents evidence of ongoing emissions.

Although MIPAS measurements are not suitable to evaluate the IHG at the surface, they provide information about the distribution of inter-hemispheric differences in the UTLS region as a function of both latitude and pressure. To analyze these differences we interpolated to a fixed pressure grid MIPAS CCl_4 profiles acquired from April 2005 to March 2012. We then binned the profiles in 5° latitude intervals and calculated, for each latitude bin, the average CCl_4 VMR profile in the considered time period. Finally, for each latitude bin in the NH we identified the corresponding bin in the

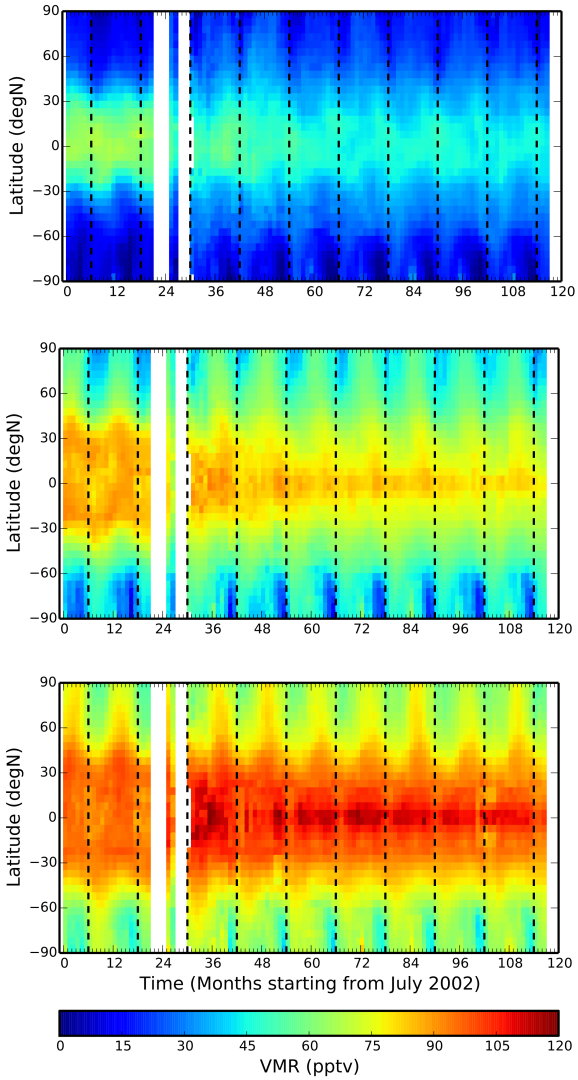

Figure 6.5: Time evolution of CCl_4 at all latitudes, from July 2002 to April 2012. The three maps refer to different pressure levels: 50 hPa (top), 90 hPa (center) and 130 hPa (bottom). The vertical dashed lines represent the year boundaries.

SH and computed the difference between the average profiles. The map of Fig. 6.6 shows the obtained average differences as a function of both latitude bin and pressure level. At high latitudes, the asymmetry likely stems from the fact that the polar vortex in the Antarctic is systematically stronger, more stable, and of longer duration than the Arctic polar vortex.

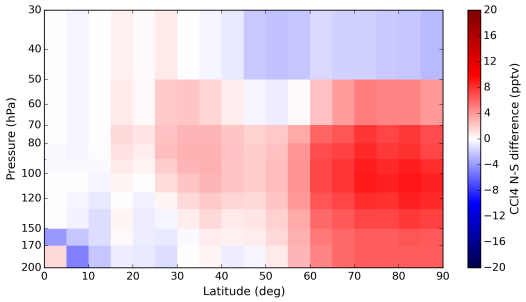

Figure 6.6: Average North-South CCl_4 VMR differences versus latitude and pressure. The average period includes MIPAS measurements from April 1^{st}, 2005 to March 31^{st}, 2012.

At mid-latitudes, NH and SH seasons are more symmetrical and the CCl_4 mean differences between the two hemispheres are probably caused by the larger CCl_4 emissions in the NH [93, 53]. As a final test we computed the weighted average of the NH-SH differences over latitude at fixed pressure levels. The weights used in the average are the solid angle fractions viewed by the individual latitude bands. The NH-SH mean differences in the UTLS span from 1.2 ppt at 130 hPa to 2.2 ppt at 100 hPa. At the lowermost pressure levels these differences are fully consistent with the IHG value of 1.5 ± 0.2 ppt (for 2000-2012) reported by [53].

6.4 Comparison with other measurements

The most accurate atmospheric CCl_4 measurements are collected at ground level, but such measurements are not suitable for direct comparison with profiles retrieved from MIPAS measurements in the 5-27 km height range. In the next two sub-sections we compare MIPAS CCl_4 profiles with co-located profiles obtained from the stratospheric balloon version of MIPAS (MIPAS-B, [27]) and from the ACE-FTS onboard the SciSat-1 satellite [2].

6.4.1 Comparison with MIPAS balloon

The balloon-borne limb emission sounder MIPAS-B can be regarded as a precursor of the MIPAS satellite instrument ([27] and references therein). Indeed, a number of specifications like spectral resolution (0.0345 cm^{-1}) and spectral coverage (750–2500 cm^{-1}) are similar. However, for other pa-

rameters the MIPAS-B performance is superior, in particular for the NESR and for the line of sight stabilization, which is based on an inertial navigation system supplemented with an additional star reference system and leads to a knowledge of the tangent altitude on the order of 90 m (3σ). The MIPAS-B NESR is further improved by averaging multiple spectra recorded at the same elevation angle. MIPAS-B limb scans are typically acquired on a 1.5 km vertical tangent height grid.

Retrieval of all species is performed on a 1 km grid with a least squares fitting algorithm using analytical derivative spectra calculated by the Karlsruhe Optimized and Precise Radiative transfer Algorithm [39, 97]. To avoid retrieval instabilities due to oversampling of vertical grid points, a regularization approach is adopted, constraining with respect to a first derivative a priori profile according to the method described by Tikhonov and Phillips. The spectral window used for the MIPAS-B target parameter retrieval of CCl_4 covers the 786.0–806.0 cm^{-1} interval. Spectroscopic parameters for the calculation of the infrared emission spectra are a combination of the HITRAN 2008 [83] database and the MIPAS dedicated database (Sect. 3.2, [73, 65]). The CCl_4 cross sections are taken from HITRAN as in MIPAS/ESA retrievals version 7. The MIPAS-B error budget includes random noise as well as covariance effects of the fitted parameters, temperature errors, pointing inaccuracies, errors of non-simultaneously fitted interfering species, and spectroscopic data errors (1σ). For CCl_4 the precision error is estimated to be between 5-10%, while the total error is 11-15%. Further details on the MIPAS-B data analysis and error estimation are provided in [108] and references therein. Tab. 6.2 lists all the MIPAS-B flights used for intercomparison with MIPAS on ENVISAT.

Further to the direct matches where the balloon and the satellite instruments observe simultaneously (within pre-defined margins) the same air-masses, we also considered trajectory matches. In this case both forward and backward trajectories were calculated [60] by the Free University of Berlin from the balloon measurement geolocation to search for air-masses sounded by the satellite instrument. Temperature and VMR values from the satellite profiles were interpolated to the trajectory match altitude such that these values can be directly compared to the MIPAS-B data at the trajectory start point altitude. To identify both direct and trajectory matches, a coincidence criterion of 1 hour and 500 km was adopted.

Location	Date	Distance (km)	Time difference (min)
Kiruna (68 N)	20 Mar 2003	16/546	14/15
	03 Jul 2003	Trajectories only	
	11 Mar 2009	187/248	5/6
	24 Jan 2010	109/302	5/6
	31 Mar 2011	Trajectories only	
Aire-sur-l'Adour (44 N)	24 Sep 2002	21/588/410/146	12/13/15/16
Teresina (5 S)	14 Jun 2005	109/497/184/338	228/229/268/269
	06 Jun 2008	224/284/600/194	157/158/169/170

Table 6.2: Overview of MIPAS balloon flights used for intercomparison with MIPAS/ENVISAT

Fig.s 6.7 and 6.8 show the average differences between CCl_4 VMR retrieved from MIPAS/ENVISAT and MIPAS-B both in absolute and relative units. The two figures refer to matching measurements in the FR and the OR phases of the MIPAS/ENVISAT mission, respectively. Combined random, systematic and total errors are also shown in the plots. The numbers reported on the left side of the plots indicate the number of matching profiles contributing to the statistics. The results of the intercomparison can be summarized as follows. In the case of FR measurements: for pressures between 80 and 190 hPa MIPAS/ENVISAT shows a statistically significant negative bias of about -10% with respect to MIPAS-B, this bias is however within the combined total error bounds. A statistically significant positive bias is also evident for pressures smaller than 25 hPa. It increases with altitude and quickly becomes incompatible with the total combined error. This bias can be at least partly explained by the selection of different microwindows used during the retrieval process of both MIPAS sensors. This bias, however, is not a major concern because it is localized at the upper end of the retrieval range. In this region the predicted uncertainty is so large that the linear approximation of the error propagation theory may easily fail to explain the discrepancies between the measurements of the two instruments. In case of OR measurements: for pressures between 150 and 190 hPa MIPAS/ENVISAT shows a statistically significant positive bias of about $+10\%$ with respect to MIPAS-B; this bias is however within the combined total error bounds. A statistically significant positive bias is also evident for pressures smaller than 25 hPa. It increases with altitude and, for pressures smaller than 20 hPa is no longer compatible with the total com-

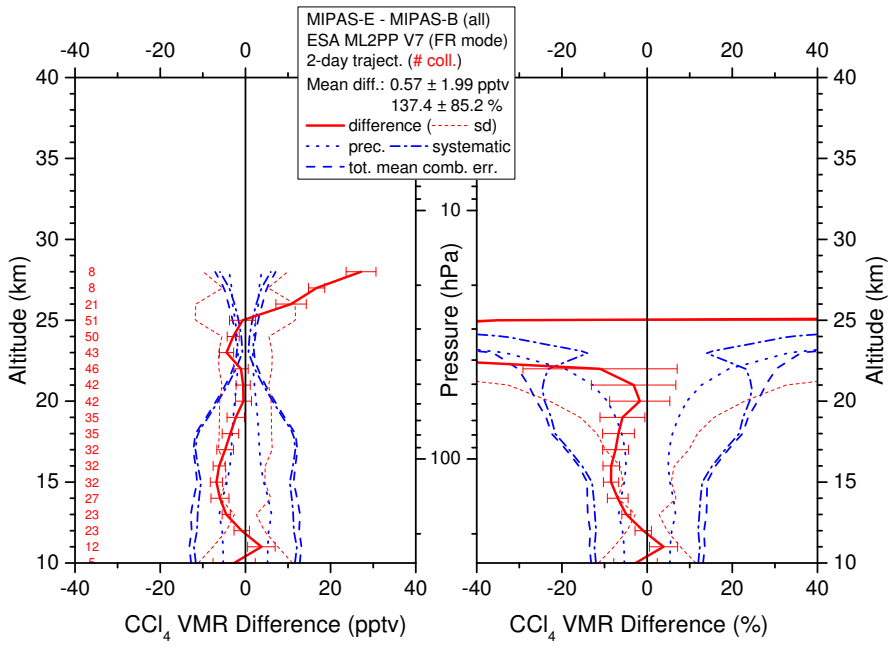

Figure 6.7: Intercomparison between MIPAS-B and MIPAS/ENVISAT (MIPAS-E) CCl_4 VMR. Results for the FR part of the MIPAS mission. The plots show mean absolute and relative VMR differences of trajectory match collocations (red numbers) between both MIPAS sensors (red solid line) including standard deviation of the difference (red dotted lines) and standard error of the mean (plotted as error bars). Precision (blue dotted lines), systematic (blue dash-dotted lines) and total (blue dashed lines) mean combined errors calculated according to the error summation ($\sqrt{\sigma^2_{MIPAS-E} + \sigma^2_{MIPAS-B}}$) are also displayed. For further details on the error calculation, see [106].

bined error. As in the FR case, this large bias occurs at the upper end of the MIPAS/ENVISAT retrieval range where the predicted combined error is very large. Furthermore, comparison with ACE-FTS (see next Section) indicates a negative bias of MIPAS with respect to ACE-FTS, in the same altitude region, hence MIPAS/ENVISAT is in the middle between MIPAS balloon and ACE-FTS.

6.4.2 Comparison with ACE-FTS V3.5

CCl_4 distribution has been routinely retrieved from ACE-FTS measurements using the most recent version of ACE-FTS retrieval algorithm (version 3.5,

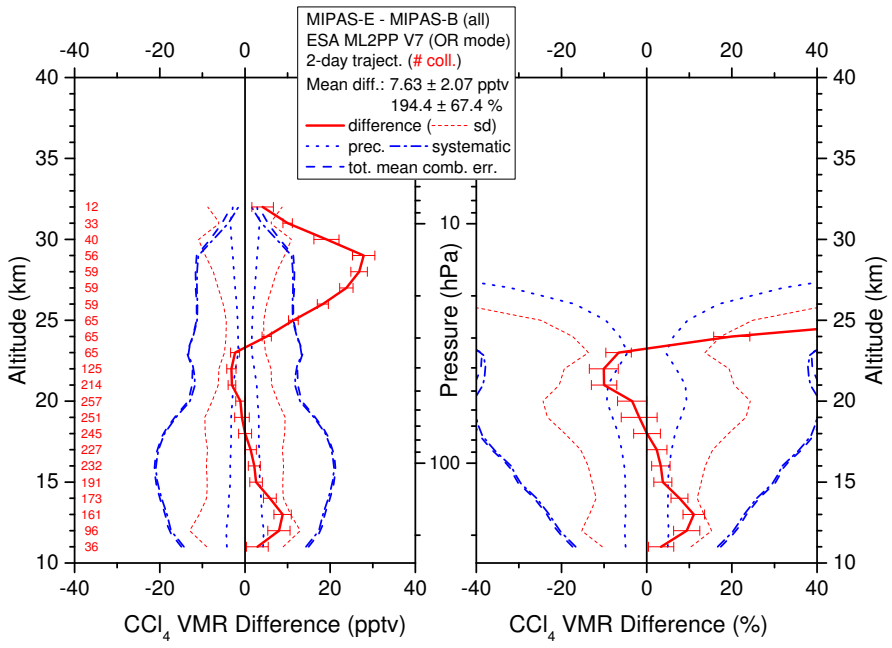

Figure 6.8: Same as Figure 6.7 but for the OR part of the MIPAS mission.

Sect. 5.5, [3, 4]). The spectral window used for CCl_4 retrievals extends from 787.5 to 805.5 cm^{-1}. Several hundred ACE-FTS measurements are coincident with MIPAS soundings of the OR part of the mission. These measurements are located both in the Northern and Southern hemispheres, mainly at latitudes larger than 45°. For comparison with MIPAS, all ACE-FTS CCl_4 data used were screened using the v3.5 quality flags. As recommended by [87], any profile data point with flag value of 2 or greater was removed and any profile containing a flag value between 4 and 7, inclusive, was discarded. For intercomparison with MIPAS measurements we adopted a matching criterion of 3 hours and 300 km. We also tested different matching criteria, such as 2 hours and 300 km, 3 hours and 200 km, but found no significant changes in the intercomparison. First we interpolated the matching MIPAS and ACE-FTS CCl_4 profiles to a fixed set of pressure levels. Then we grouped the profile differences in latitudinal intervals. The results of the comparison are summarized in Fig. 6.9. Each of the four plots of the figure refers to one of the considered latitude intervals: 50–70° and 70–90° in both the Southern and the Northern hemispheres. Each plot shows the average CCl_4 difference profile between co-located MIPAS and ACE-FTS measure-

ments (red) with standard deviation of the mean (red error bars, calculated as the standard deviation of the differences divided by the square root of the sample size). The standard deviation of the differences (orange), the total random error (green), the total systematic error of the difference (blue) are also shown. The number of co-located pairs contributing at each pressure level is reported on the right side of each plot. The average difference (red line) quantifies the systematic bias between ACE-FTS and MIPAS, the error bars indicate its statistical significance. The standard deviation (orange) is an *ex-post* estimate of the combined random error of the individual profile differences and, therefore, should be similar to its *ex-ante* estimate represented in the plots by the green line. We calculated the ex-ante random error of the individual profile differences as the quadrature summation of the ACE-FTS and MIPAS random errors. The ACE-FTS random error is estimated via the noise error covariance matrix of the retrieval included in the Level 2 products. The MIPAS random error is estimated as the quadrature summation of the measurement noise error evaluated by the covariance matrix of the retrieval [12] and the other error components that are expected to change randomly in our sample, i.e. the errors that we classified of types a) and b) in Sect. 6.2.1. The systematic error of the profile differences is obtained as the quadrature summation of the ACE-FTS and the MIPAS errors that are constant within the sample and are not expected to bias in the same direction the measurements of the two instruments. On the basis of the error figures suggested by [1], for ACE-FTS we assumed a 20% systematic error constant at all pressure levels. For MIPAS we calculated the quadrature summation of systematic errors that in Sect. 6.2.1 we classified as of type c) and d). For the calculation of the combined systematic error we explicitly excluded the uncertainty in the CCl_4 cross-section data [80] that are used, approximately in the same spectral region, both in MIPAS and ACE-FTS retrievals.

Apart from the latitude interval from 50 to 70° S, the systematic differences between MIPAS and ACE-FTS are within 5 pptv ($\sim$ 10 %, mostly not significant from the statistical point of view) in the pressure range from 50 to 100–110 hPa. The amplitude of systematic differences increases up to 15–20 pptv and becomes statistically significant at 30 hPa, while it is again quite small at 20 hPa. In the latitude interval from 50 to 70° S we observe a statistically significant $\approx$ 10 pptv low bias of MIPAS with respect

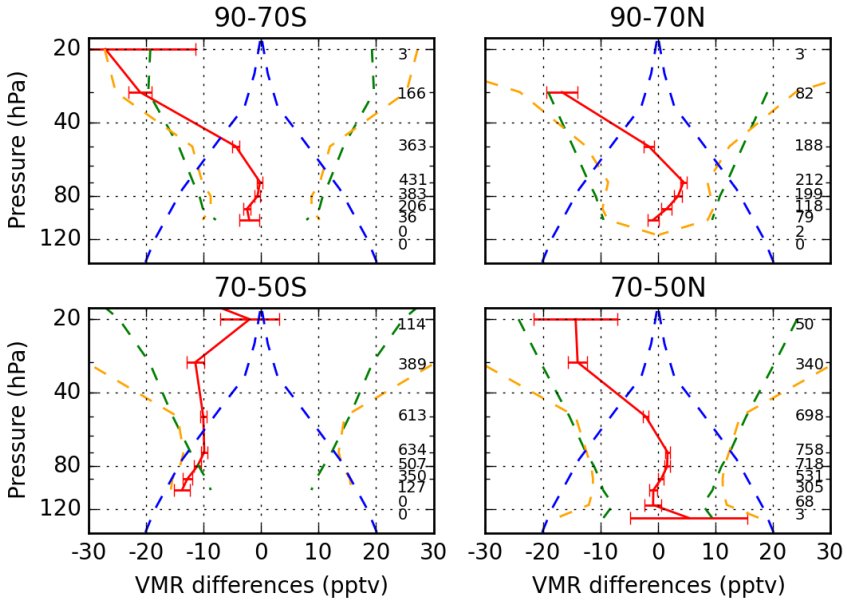

Figure 6.9: Mean CCl_4 profile difference between co-located MIPAS and ACE-FTS measurements (red) with standard deviation of the mean (red error bars). The standard deviation of the differences (orange), the estimated total random (green) and total systematic (blue) errors of the difference are also shown. The number of co-located pairs for each pressure level is reported on the right side of each graph. Each plot refers to a latitude interval as indicated in the title.

to ACE-FTS, almost uniform over the entire retrieval height range. At all latitudes, the observed biases are compatible with the estimated combined systematic error only for pressures greater than 40 hPa. At 30 hPa the bias is statistically significant and incompatible with error bars. The reason for this inconsistency is still unclear; however, preliminary investigations show that the inconsistency will be reduced when using the future release version 4.0 of ACE-FTS products.

The ex-ante estimate of the combined random error (green line in Fig. 6.9) agrees pretty well with the ex-post estimated standard deviation of the profile differences (orange line) in the range between 40 and 80–100 hPa. At the limits of the retrieval range the observed variability of the differences generally exceeds the ex-ante estimate of the random error. This may be due both to the fact that our ex-ante random error estimate does not take into account the imperfect matching of the compared profiles, and to the fact

that, at these specific altitudes, the sensitivity of the measurements to the CCl_4 VMR is so low that the linear approximation of the error propagation theory could provide only rough error estimates.

As a final remark we note that at 30 hPa MIPAS-B (Fig. 6.8) and ACE-FTS (Fig. 6.9) intercomparisons provide contrasting indications on the MIPAS bias in the OR part of the mission. While MIPAS-B suggests a positive MIPAS bias of about 10 pptv, ACE-FTS points to a negative bias of $10 - 20$ pptv.

6.5 Comparison with model simulations

In order to evaluate MIPAS CCl_4 distribution on a global scale, we compare MIPAS measurements with data of the European Centre for medium–range weather forecasts – HAMburg (ECHAM) / Modular Earth Submodel System (MESSy) Atmospheric Chemistry (EMAC, [43]) model.

6.5.1 EMAC

The numerical model EMAC is a modular global climate and chemistry simulation system with several sub-models for the calculation of dynamic and chemistry processes in the atmosphere. The core of EMAC is the general circulation model ECHAM5 [79]. ECHAM5 was developed at the Max-Planck Institute for Meteorology and the University of Hamburg. It uses the spectral transformation method and it is based on the weather forecast model of the European Centre for Medium-Range Weather Forecast (ECMWF). ECHAM5 simulations are performed in a T42 (triangular) spectral resolution which corresponds to a quadratic Gaussian grid of $2.8° \times 2.8°$ in latitude and longitude. The simulations can be made with two possible vertical resolutions: 90 (L90MA) model levels or 47 (L47MA) model levels, both reaching about 80 km. The MESSy system ([43, 44], see also `http://www.messy-interface.org`) comprises several sub-models to describe different processes that occur in the atmosphere, such as the Module Efficiently Calculating the Chemistry of the Atmosphere (MECCA, [84]) chemistry model. Due its modular structure EMAC can be operated in different modes, such as general circulation model (GCM) or as a quasi chemistry transport model (QCTM) without feedbacks from the chemistry to the dynamics.

In the last decades several CCM have been developed in order to study the chemistry and the dynamics of the troposphere and the middle atmosphere. The International Global Atmospheric Chemistry (IGAC) / SPARC Chemistry-Climate Model Initiative (CCMI, `http://blogs.reading.ac.uk/ccmi/`) was established to coordinate CCM modeling activities. With the aim to define common scenarios to be simulated, CCMI have suggested three reference simulations:

- the free-running hindcast simulations from 1960 to 2010 (RC1),
- the hindcast simulations with specified dynamics (SD) from 1980 to 2010 (RC1SD), and
- the combined free-running hindcast and forecast from 1960 to 2100 (RC2).

The hindcast simulations with SD are computed taking a branch of the corresponding free-running hindcast simulations and performing the "nudge" by Newtonian relaxation towards ECMWF ReAnalysis (ERA) – Interim re-analysis data [16]. The Newtonian relaxation (or nudging) of the ECHAM5 base model is applied in spectral space for the prognostic variables divergence, vorticity, temperature, and the (logarithm of the) surface pressure. The idea was to correct potential temperature biases and to investigate the response of the model.

For this specific comparison we use two different simulations with SD:

- the RC1SD-Base-07 (the global mean temperature was included in the nudging) and
- the RC1SD-Base-10 (the global mean temperature was omitted).

Both simulations are performed from 1979 to 2013 with T42 spectral resolution ($2.8^\circ \times 2.8^\circ$) and with 90 model levels.

6.5.2 Latitude-pressure comparison

We build specific climatologies using CCl_4 ESA MIPAS measurements and both EMAC RC1SD (Base-07 and Base-10) simulations through the following procedure. First we linearly interpolate in log-pressure all the considered CCl_4 VMR profiles to the 28 SPARC data initiative [36] pressure levels (300,

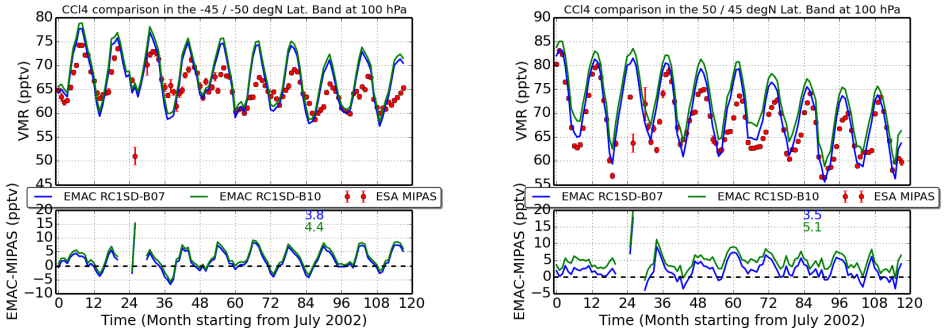

Figure 6.10: Upper panels: CCl_4 ESA MIPAS (red dots), EMAC RC1SD-Base-07 (blue line) and EMAC RC1SD-Base-10 (green line) monthly mean time series in the 45°S - 50°S (left) and in the 45°N - 50°N (right) latitudinal band at 100 hPa. The error bar of the red dots represents the standard deviation of the mean of the ESA MIPAS monthly means. Lower panels: Absolute difference time series between ESA MIPAS and EMAC RC1SD-Base-07 (blue line) and between ESA MIPAS and EMAC RC1SD-Base-10 (green line). The RMSE of EMAC RC1SD-Base-07 minus ESA MIPAS (blue number) and EMAC RC1SD-Base-10 minus ESA MIPAS (green number) time series are also reported.

250, 200, 170, 150, 130, 115, 100, 90, 80, 70, 50, 30, 20, 15, 10, 7, 5, 3, 2, 1.5, 1.0, 0.7, 0.5, 0.3, 0.2, 0.15, 0.1 hPa). We then group the interpolated profiles in 5° latitude bins and calculate monthly averages. Using these climatologies, we have performed a detailed comparison for each 5° latitude band and each pressure level. Two examples of this analysis are reported in Fig 6.10. In order to summarize the results of the comparison, we compute the root mean square error (RMSE) as follows

$$RMSE = \sqrt{\frac{\sum_{i=1}^{N}(VMR_i^{EMAC} - VMR_i^{MIPAS})^2}{N}} \tag{6.1}$$

where N is the length of the MIPAS mission in months, VMR_i^{EMAC} and VMR_i^{MIPAS} represent respectively the EMAC CCl_4 and ESA MIPAS CCl_4 monthly means. In the case of no differences between the two considered time series, RMSE would be equal to zero. RMSE becomes greater as the difference between the two time series increases. In Fig. 6.10 we show the distribution of RMSE as a function of latitude and pressure.

We observe a general good agreement in all the UTLS region. The agree-

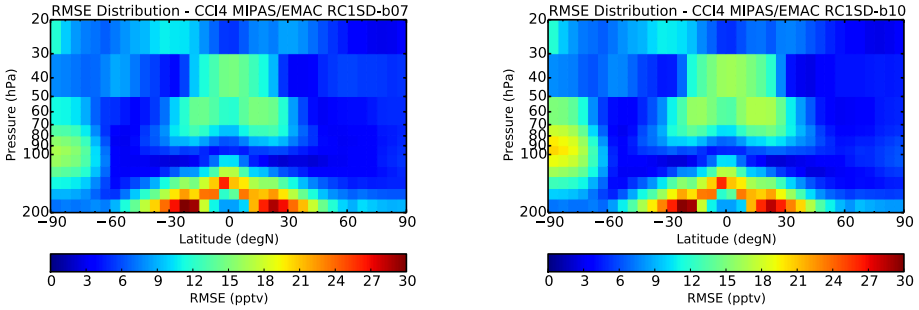

Figure 6.11: Map of the RMSE calculated using CCl_4 ESA MIPAS and EMAC RC1SD-Base-07 datasets (left) and CCl_4 ESA MIPAS and EMAC RC1SD-Base-10 (right).

ment between ESA MIPAS and both EMAC RC1SD simulations appears better in the NH with respect to the SH. At the south pole the differences become higher due to the presence of the poler vortex. In this region, and also at the tropics region around 50 hPa, the agreement is better considering RC1SD-Base-07 simulation. This result highlights that the EMAC simulation with the full nudging of the temperature (RC1SD-Base-07) is able to better reproduce the dynamic of the atmosphere and consequently the CCl_4 vertical distribution. In general RC1SD-Base-07 simulation better reproduces the atmospheric dynamics in the regions where vertical motions play a key role, such as the poles and the tropics, introducing clear improvements in the comparison with real measurements.

6.5.3 Comparison within the IG2 latitude bands

We perform another comparison considering the IG2 latitude bands (Sect. 3.3). ESA MIPAS measurements and both EMAC simulations are used to calculate CCl_4 mean profiles within each latitude band (Fig. 6.12). A general good agreement is evident at middle and high latitudes. At mid-latitudes the major differences are at the lower pressure levels (below 100 hPa). At the tropics the agreement is good between 100 and 30 hPa, becoming worst below 100 hPa. This result is consistent with the 20% positive bias of CCl_4 ESA MIPAS with respect to the observations of the NOAA/HATS and AGAGE networks (Sect. 6.6.2). As already observed in Fig. 6.11, at all latitudes the differences increase above 30 hPa. A similar analysis has been

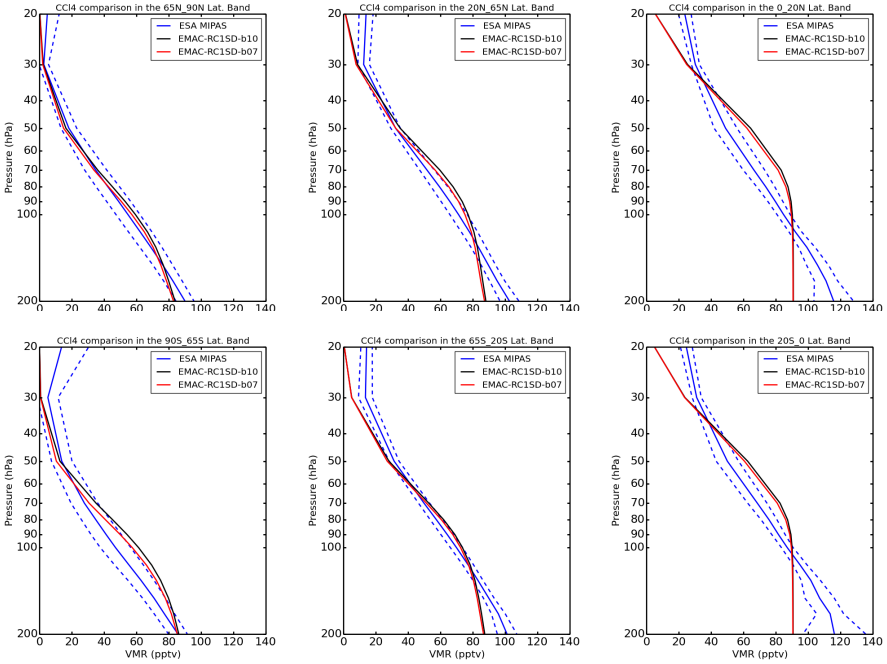

Figure 6.12: CCl_4 ESA MIPAS (blue lines), EMAC RC1SD-Base-10 (black lines) and EMAC RC1SD-Base-07 (red lines) mean profiles within 90°N-65°N (upper left), 65°N-20°N (upper center), 20°N-0° (upper right), 65°S-90°S (bottom left), 20°S-65°S (bottom center) and 0°-20°S (bottom right) latitudinal band. Dashed blue lines show the standard deviation of the CCl_4 ESA MIPAS profiles.

performed considering the seasonal average profiles, showing similar results due to the weak seasonal variability of CCl_4 distribution.

We also calculate the correlation between CCl_4 ESA MIPAS and both EMAC RC1SD monthly means time series for the different latitudinal bands. We report in Fig. 6.13 the analysis made using CCl_4 ESA MIPAS and CCl_4 EMAC RC1SD-Base-07 simulations. The results are summarized in Tab. 6.3. The results of the analysis performed using EMAC RC1SD-Base-10 are similar to those presented in Fig. 6.13 with slightly lower correlations at all latitudes. At middle latitudes of both hemispheres and at the north pole the agreement is good, whereas at the tropics we observe the worst results. At the south pole the distribution appears more scattered due to the relatively higher seasonal variability with respect to the other latitudinal bands.

	POL S	MID S	TRO S	TRO N	MID N	POL N
MIPAS/RC1SD-Base-07	0.917	0.957	0.882	0.866	0.949	0.961
MIPAS/RC1SD-Base-10	0.900	0.953	0.874	0.857	0.941	0.956

Table 6.3: Correlation between MIPAS and EMAC RC1SD-Base-07 (second row) and RC1SD-Base-10 (third row) monthly means for different latitudinal bands.

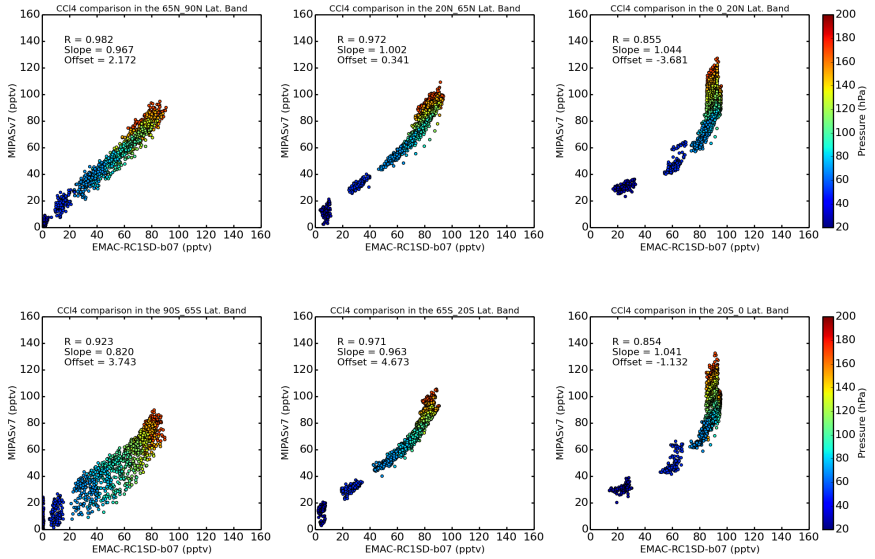

Figure 6.13: Correlation between CCl_4 ESA MIPAS and EMAC RC1SD-Base-07 monthly means within within 90°N-65°N (upper left), 65°N-20°N (upper center), 20°N-0° (upper right), 65°S-90°S (bottom left), 20°S-65°S (bottom center) and 0°-20°S (bottom right) latitudinal band. Similar results have been found considering CCl_4 ESA MIPAS and EMAC RC1SD-Base-10 monthly means.

6.6 Trends

The measurements used for the analysis presented in this study cover the entire MIPAS mission, from July 2002 to April 2012. The CCl_4 VMR profiles considered are those derived by the ESA Level 2 processor version 7 analysing MIPAS limb scanning measurements with tangent heights in the 6-70 km range, obtained from NOM, MA and UTLS-1 observational modes (see Sect. 2.3). First we build a CCl_4 VMR climatology following the procedure describe in Sect. 6.5.2. Then, using the least-squares method, for each latitude bin and pressure level we fit the following function VMR(t) to the time series of the monthly averages:

$$\begin{aligned}\mathrm{VMR}(t) = a_{\mathrm{FR}}\,\mathbf{1}_{\mathrm{FR}}(t) + a_{\mathrm{OR}}\,\mathbf{1}_{\mathrm{OR}}(t) + b\,t + f_1\,\mathrm{qbo30}(t) + f_2\,\mathrm{qbo50}(t) + \\ + g\,\mathrm{SRF}(t) + \sum_i \left[c_i \sin\left(\frac{2\pi t}{T_i}\right) + d_i \cos\left(\frac{2\pi t}{T_i}\right)\right].\end{aligned} \tag{6.2}$$

In this expression t is the time expressed in months since the beginning of the mission (July 2002) and a_{FR}, a_{OR}, b, f_1, f_2, g and c_i, d_i, $i = 1, ..., 8$ are the 22 fitting parameters. The function $\mathbf{1}_{\mathrm{P}}(t)$ is the indicator function of the time interval P, such that $\mathbf{1}_{\mathrm{P}}(t) = 1$ if $t \in \mathrm{P}$ and $\mathbf{1}_{\mathrm{P}}(t) = 0$ otherwise. The functions qbo30(t) and qbo50(t) are the quasi-biennial oscillation (QBO) quantifiers and SRF(t) is the solar radio flux index. The two QBO terms (available at `http://www.geo.fu-berlin.de/met/ag/strat/produkte/qbo/index.html`) represent the Singapore winds at 30 and 50 hPa [50]. The SRF index is calculated using measurements of the solar flux at 10.7 cm (available at `http://lasp.colorado.edu/lisird/tss/noaa_radio_flux.html`) and is considered a good proxy for the solar activity. We re-normalized both the QBO and the SRF proxies to the interval $[-1, +1]$ within the time frame covered by MIPAS mission. The terms in the sum are 8 sine and 8 cosine functions. They represent periodic oscillations with period T_i. In T_i we include annual (12 months), semi-annual (6 months) and other characteristic atmospheric periodicities of 3, 4, 8, 9, 18 and 24 months [32]. We decided to fit two different constant parameters for the two parts of the mission: a_{FR} for the FR and a_{OR} for the OR part. The aim of this choice is to account for possible relative biases between the two phases of the mission. These may be caused, for example, by the different

spectral resolutions adopted, by the different MWs used for the retrieval and by the different vertical and horizontal samplings of the instrument in the two mission phases. We calculate the uncertainty on the fitted parameters assuming each monthly average is affected by an error given by the standard deviation of the mean. Furthermore we multiply the uncertainty obtained from the error propagation analysis by the square root of the normalized least squares (the so-called "reduced χ^2"). This latter operation is intended to account also for the quality of the fit in the evaluation of trend errors.

6.6.1 Results

Fig. 6.14 shows some examples of CCl_4 trend analysis. Each panel refers to a specific latitude band and pressure level. The top plot of each panel shows the time series of the monthly averages with error bars given by the standard deviation of the mean (blue symbols). The red curve represents the best fitting function VMR(t), while the green line represents the constant and the linear (trend) terms of VMR(t). In the lower plot of each panel we show the residuals of the fit (the monthly averages minus the values calculated on the fitting curve). In each panel we also report the value obtained for the trend, its uncertainty and the difference between the two constant terms $a_{FR} - a_{OR}$.

The quality of the fit is generally better in the OR period. Indeed, in this mission phase the instrument provides measurements with more uniform and finer geographical coverage. We also carried out a spectral analysis of the fitting residuals, which revealed that all the periodicities embedded in the considered time series of monthly means are properly accounted for by the fitting function (Eq. 6.2).

Fig. 6.15 summarizes the results obtained for CCl_4 trends. Panel a) shows the absolute trends. Negative trends are observed at all latitudes in the UTLS region. The magnitude of the negative trend decreases with increasing altitude. The trend shows slightly positive values (about 5-10 pptv/decade) in a limited region, particularly in the Southern mid-latitudes between 50 and 10 hPa. This feature is probably related to the asymmetry in the general circulation of the atmosphere. The air at higher altitudes can be considered *older* than the tropospheric air that has been lifted up by strong convection mechanisms in the tropical regions [96]. The tropospheric air just injected into the stratosphere is richer in CCl_4. We attribute positive

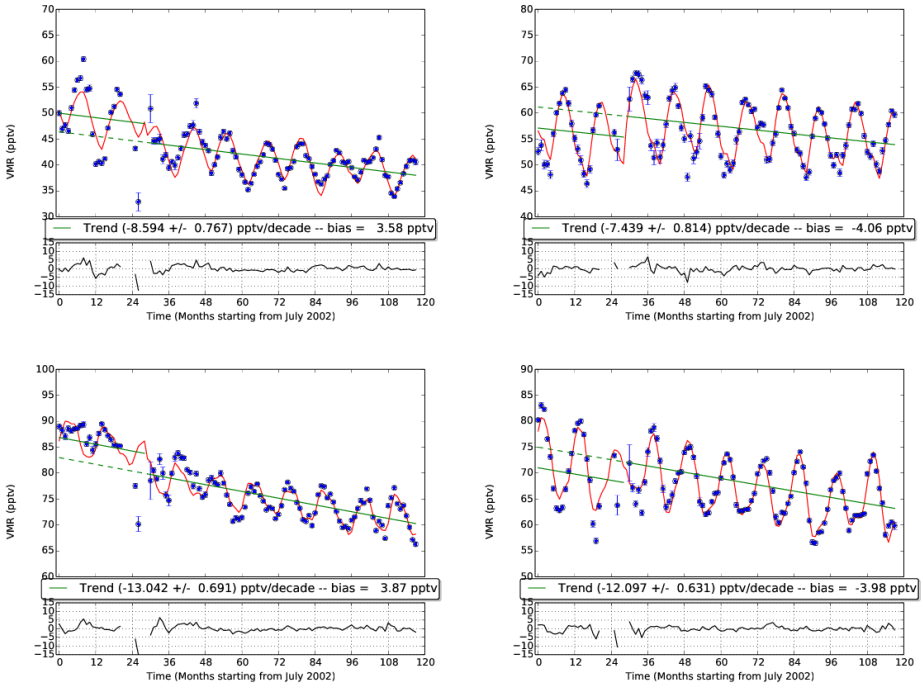

Figure 6.14: CCl_4 trend analysis for 20° S/25° S at 50 hPa (top left), 55° S/60° S at 100 hPa (top right), 25° N/20° N at 90 hPa (bottom left) and 50° N/45° N at 100 hPa (bottom right). The blue dots are the MIPAS monthly averages and the error bars are the standard deviation of the means. The red curve is the best fitting function VMR(t) and green line is the linear term (trend). The lower part of each plot shows the residuals between the MIPAS monthly averages and the best fitting function VMR(t). The CCl_4 trend, its uncertainty and the *bias* between FR and OR are also indicated in each panel.

stratospheric trend values in certain latitude regions to the less effective mixing mechanisms in the stratosphere as compared to the troposphere at these latitudes. Similar features have also been observed by other authors in CFC-11 and CFC-12 trends [45]. Recently some studies [34, 55, 66] have shown that the trends in stratospheric trace gases are affected by variability in the stratospheric circulation. This has been shown for a number of halogen source gases and the complementary degradation products (i.e. HCl and HF). This variability can partially explain why the stratospheric trend does not simply follow the tropospheric trend with a time lag.

Assuming for each latitude bin and pressure level the average CCl_4 VMR

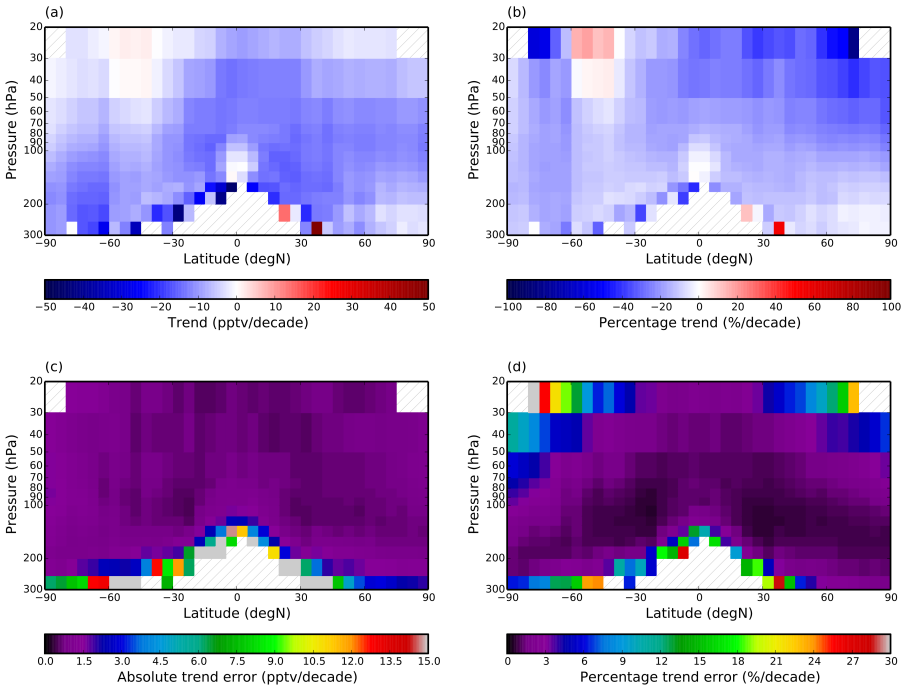

Figure 6.15: CCl_4 trends as a function of latitude and pressure. Panel a) absolute trends, b) percentage trends, c) absolute errors, d) percentage errors. Latitudes / pressures with trend error greater than 30% are masked with dashed areas.

obtained from the full MIPAS dataset, we also calculated the relative CCl_4 trends. They are shown in the panel b) of Fig. 6.15. The same considerations made for the absolute trends apply also to relative trends. The asymmetry between the NH and the SH is very pronounced, the NH having larger negative relative trends increasing with altitude and reaching 30-35%/decade at 50 hPa. Note however that above 50 hPa they show large variations with both latitude and pressure. These oscillations correspond to extremely small average VMR values that make the relative trend numerically unstable. Panels c) and d) of Fig. 6.15 show, respectively, the absolute and percentage random errors on the trends. The uncertainties increase above 20 hPa. Large uncertainties are associated to latitude bins and pressure levels for which a relatively small number of measurements is available. For clarity in Fig. 6.16 we show the ratio between CCl_4 trends and the related random errors. Latitude bins / pressure levels with ratio values less than

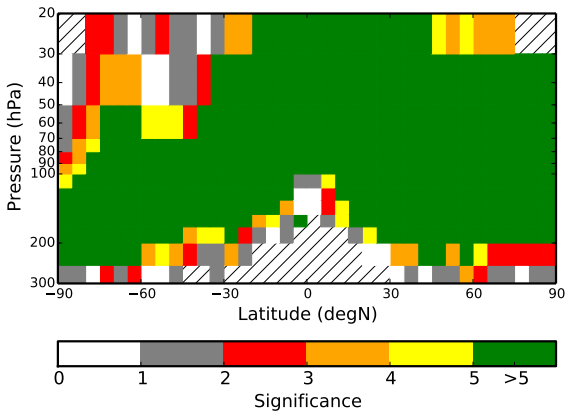

Figure 6.16: Map of the ratio between CCl_4 trends and associated random errors.

2 are marked with white and grey colors and correspond to trend values that are not significantly different from zero from the statistical point of view. Note, however, that most of the calculated trends are greater than 5 times the related error, and are thus statistically significant. In the maps of Fig.s 6.15 and 6.16, values corresponding to errors greater than 30% are masked with dashes. We consider unreliable any trends with errors greater than this threshold.

As mentioned in Sect. 6.2.1, an important source of uncertainty could arise from a residual drift of the calibration error, possibly due to neglecting changes in detector non-linearity as the instrument ages. As outlined in Sect. 6.2.1, however, the worst case scenario for the drift of the calibration error could amount to 1% of the calibration error itself, which in turn, is of the order of 0.4% of each individual retrieved CCl_4 VMR profile. Therefore, this error source is negligible compared to the statistical error shown in panel d) of Fig. 6.15.

6.6.2 Comparison with CCl_4 trends reported in literature

Although measurements acquired at ground stations cannot be directly compared with MIPAS profiles that have a lower altitude limit of 5-6 km, we can still compare tropospheric CCl_4 trends derived from MIPAS with trends derived from ground-based measurements. Under the assumption of well-

mixed troposphere, we can consider the CCl_4 vertical distribution approximately constant [14, 1]. We consider observations provided by two networks that regularly perform long-term, highly accurate near-surface measurements of various tracers, including CCl_4: the NOAA/ESRL/HATS (`http://www.esrl.noaa.gov/gmd/hats/`) and the AGAGE [89, 70, 71] `http://agage.mit.edu/`) networks. The NOAA/ESRL/HATS group provides accurate measurements of CCl_4 through three different programs: two in situ electron capture detector (ECD) measurement programs and one flask system using gas chromatography with ECD program. In this work we use a CCl_4 combined dataset, developed by the NOAA to homogenize all of the measurements made by the different programs (more details at `http://www.esrl.noaa.gov/gmd/hats/combined/CCl4.html`). All the CCl_4 NOAA records are reported on the NOAA-2008 scale. AGAGE measurements used here are obtained using in situ gas chromatography with ECD and reported on the SIO-2005 calibration scale. NOAA and AGAGE in situ measurements at common sites are inter-compared every 6 months for validation purposes.

To compare MIPAS CCl_4 trends to those derived from the ground-based measurements of NOAA and AGAGE, we first choose a pressure level belonging to the troposphere, with the following procedure. For each latitude bin (λ) and MIPAS monthly average profile we identify the tropopause with the pressure level where the monthly average temperature shows its minimum value. We multiply this pressure by 1.6 and find the nearest pressure level ($p_t(\lambda)$) in the fixed pressure grid defined in Sect. 6.6. Using this procedure the selected pressure level is located approximately 3 km below the tropopause. For each latitude bin and month we then compute the monthly CCl_4 average at $p_t(\lambda)$. Finally, for each latitude bin, we calculate the trend at this month- and latitude- dependent tropospheric pressure as explained in Sect. 6.6. Fig. 6.17 compares the time series of ground-based CCl_4 measurements of selected stations (black and orange lines) with MIPAS monthly tropospheric averages (blue dots) in the same latitude bin of the ground station. The two plots refer to ground stations located at tropical (top) and middle (bottom) latitudes. Ground-based measurements do not really show a seasonality, while MIPAS measurements do. The amplitude of the seasonal variations observed by MIPAS increases with latitude. For tropical latitudes MIPAS OR measurements show a positive bias of approximately 15%. Although not focused on tropical regions, Fig. 6.8 comparing MIPAS to balloon

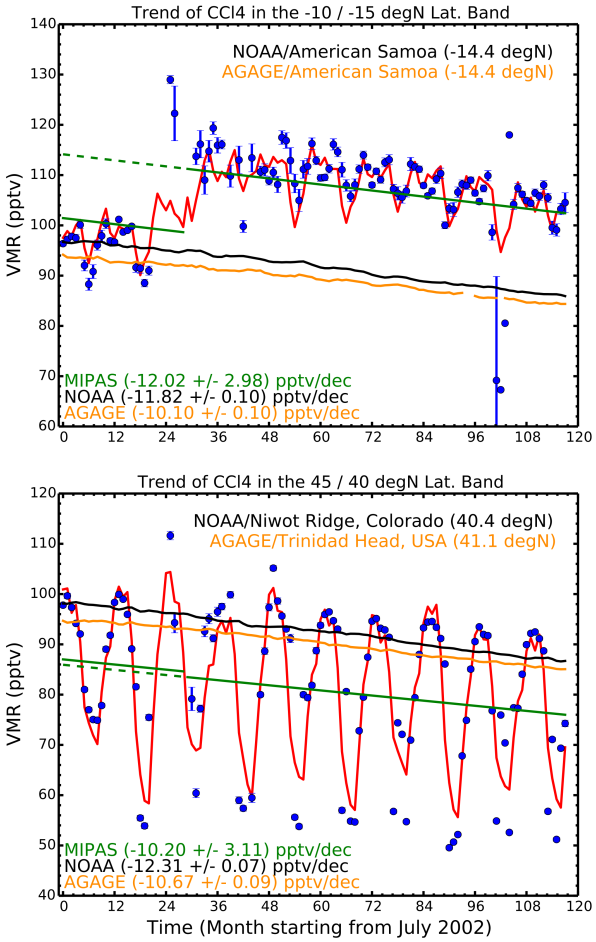

Figure 6.17: Comparison between MIPAS (blue dots) and NOAA/AGAGE (black/orange) CCl_4 time series. The two plots refer to ground stations located at tropical (top) and middle (bottom) latitudes. The red curve is the fitting model used to derive the trend from MIPAS data, the green line is the linear part of the model itself. The obtained trend values are also shown in the plots.

measurements, already suggests the existence of this bias. At middle latitudes the maximal values of the MIPAS time series roughly match ground measurements. In Fig. 6.17 we also show the trend values determined on the basis of the plotted measurements. In the examined cases the trends obtained from MIPAS and ground stations are in very good agreement.

In Tab. 6.4 we compare MIPAS tropospheric CCl_4 trends with trends derived for the 2002–2012 decade from NOAA/AGAGE stations located

Site Code	Site Name	Latitude (degN)	Network	In-situ trend (pptv/decade)	MIPAS trend (pptv/decade)	MIPAS Lat. Band (degN)
BRW	Barrow, USA	71.3	NOAA	-12.7	-3.2 ± 10.4	70/75
MHD	Mace Head, Ireland	53.3	AGAGE	-10.1	-4.7 ± 5.1	50/55
THD	Trinidad Head, USA	41.1	AGAGE	-10.6	-10.2 ± 3.1	40/45
NWR	Niwot Ridge, USA	40.4	NOAA	-12.3	-10.2 ± 3.1	40/45
MLO	Mauna Loa, USA	19.5	NOAA	-12.2	-14.9 ± 2.3	15/20
RPB	Ragged Point, Barbados	13.2	AGAGE	-10.7	-12.7 ± 3.6	10/15
SMO	Tatuila, American Samoa	-14.4	NOAA AGAGE	-11.8 -10.1	-12.0 ± 3.0	$-10/-15$
CGO	Cape Grim, Tasmania	-40.7	AGAGE	-10.2	-25.9 ± 5.4	$-40/-45$
SPO	South Pole, Antartica	-90.0	NOAA	-11.9	-7.9 ± 10.6	$-85/-90$

Table 6.4: For each ground station the table columns show respectively: site code, site name, site latitude, network name, station-related CCl_4 trend, tropospheric MIPAS trend, latitudinal band from which MIPAS data were extracted.

in the same latitude band. Some stations produce CCl_4 trends in very good agreement with MIPAS. However, in general, and especially in the polar regions, the variability of the tropopause is quite large, thus producing time series of MIPAS monthly averages at $p_t(\lambda)$ that can not be adequately matched by the fitting function defined in Eq. 6.2. This feature sometimes generates large residuals in the trend fit and thus large trend errors and/or unrealistic trend values. Despite this difficulty, from the statistical point of view the only trends calculated at the CGO site disagree significantly. We attribute this disagreement to the instabilities occurring in MIPAS data at low altitudes. Indeed, the MIPAS tropospheric trend estimated for the latitude bin 35°/40° S (the bin adjacent to the CGO site) is already equal to -9.16 ± 2.03 pptv/decade, i.e. in perfect agreement with the trend calculated from the CGO measurements.

Looking at the literature we found that [5] estimate the global CCl_4 trend from ACE-FTS measurements. The authors consider CCl_4 VMR profiles obtained from ACE-FTS in the 30° S/30° N latitude belt. They cal-

culate yearly averages of CCl_4 VMR in the altitude range from 5 to 17 km and fit the seven 2004-2010 yearly averages with a linear least-squares approach. The resulting trend is -13.2 ± 0.9 pptv/decade. If we average MIPAS trends presented in Sect. 6.6.1 in the 30° S/30° N latitude interval and in the 100–300 hPa pressure range, with a filter discarding trend values with relative error greater than 30%, we get an average trend of -12.80 ± 0.12 pptv/decade. This value is in very good agreement with the trend determined from ACE-FTS. Note also that, since MIPAS measures atmospheric emission its sampling is finer than that of ACE-FTS both in space and time. With MIPAS it is therefore possible to estimate trends with a better precision.

6.7 Lifetime

In this section, we estimate the stratospheric lifetime of CCl_4 according to the tracer-tracer correlation method established by [102] based on the theoretical framework presented by [68] and [69]. Here we choose $CFC-11$ as the reference tracer (b) correlated to CCl_4 (tracer a). The stratospheric lifetime can be calculated using the following equation:

$$\frac{\tau_a}{\tau_b} = \frac{\frac{\overline{\sigma_a}}{\overline{\sigma_b}}}{\frac{d\sigma_a}{d\sigma_b}\Big|_{tropopause}} \tag{6.3}$$

where τ_a and τ_b are the stratospheric lifetimes of the two correlated tracers and $\overline{\sigma_a}$, $\overline{\sigma_b}$, $d\sigma_a/d\sigma_b$ are, respectively, the atmospheric VMRs of the two species and the slope of the correlation at the tropopause in steady-state. A major complication that arises when using Eq. 6.3 is due the fact that the considered tracers decline in the 2002 - 2012 decade, therefore MIPAS measurements can not be considered to refer to a steady state. Using decadal averages for $\overline{\sigma_a}$ and $\overline{\sigma_b}$ does not actually cause large errors in τ_a, however, replacing the steady state slope with the measured slope $d\chi_a/d\chi_b$ may be a rough approximation [102]. The difference between the slopes in steady- and transient- states is mainly linked to the tropospheric change rate γ_0 of the tracers in the considered time period. In order to account for the effect

of γ_0 on $d\sigma_a/d\sigma_b$ we use the following formula proposed by [102]:

$$\left.\frac{d\sigma_a}{d\sigma_b}\right|_{tropopause} = \frac{\frac{d\chi}{d\chi_b}\big|_{tropopause} \cdot \frac{d\chi_b}{d\Gamma}\big|_{\Gamma=0} + \gamma_{0_a}\sigma_{0_a}}{\frac{d\chi_b}{d\Gamma}\big|_{\Gamma=0} + \gamma_{0_b}\sigma_{0_b}} \cdot \frac{1-2\gamma_{0_b}\Lambda}{1-2\gamma_{0_a}\Lambda}. \tag{6.4}$$

In this expression $d\chi_b/d\Gamma\big|_{\Gamma=0}$ is the slope of the reference tracer (b) with respect to the age of air Γ at the tropopause, Λ is the width of the atmospheric age spectrum, γ_0 and σ_0 are, respectively, the effective linear growth rate and the VMR of the tracers at the tropopause. According to [102], γ_0 can be calculated as:

$$\gamma_0 = c - 2\Lambda d \tag{6.5}$$

where c and d are time-dependent coefficients. At each month (t) they are obtained by fitting a 5-years prior time series of monthly VMR averages of the considered tracer at the tropopause level ($\chi_0(t')$) with the following function:

$$\chi_0(t') = \chi_0(t)[1 + c(t'-t) + d(t'-t)^2]. \tag{6.6}$$

To derive lifetime estimates, as suggested in [6], we considered only the latitudes in the so-called *surf* zone [102], between 30° N/S and 70° N/S. The tropical regions are not suitable to estimate the stratospheric lifetime using the tracer-tracer method due to the intense large-scale upwelling [68]. Similarly, the polar regions are not suitable for this study due to the intense subsidence, especially during winter [67]. For each month of the MIPAS mission and each 5° latitudinal band between 30° N/S and 70° N/S, we determine the pressure level corresponding to the tropopause, as the level with a minimum in the monthly average temperature profile. For CFC-11 we assume a lifetime τ_b = 52(43 - 67) years [92]. To determine the coefficients c and d appearing in Eq. 6.6, at each MIPAS measurement month t we fit a time series of HATS (`http://www.esrl.noaa.gov/gmd/hats/`) CCl_4 and CFC-11 global monthly averages. Each time series extends back in time for 5 years, starting from the month t. The calculation is then repeated for each month of the MIPAS mission, from April 2002 to July 2012. For the estimation of lifetimes limited to NH and SH we used respectively NH and SH HATS monthly means instead of global monthly mean. We then used the coefficients c and d to calculate the effective linear growth rate γ_0 via Eq. 6.5, assuming Λ =1.25 years [102, 51].

To estimate the slope of CFC-11 with respect to the age of air at the tropopause we used an analysis of air samples acquired on board *Geophysica* aircraft [51]. The analysis produces a $d\chi_b/d\Gamma\big|_{\Gamma=0}$ value of -20.6 ± 4.6 *ppt* yr^{-1} for 2010. We calculated the slope for other years by scaling the 2010 value according the relative change of the yearly γ_0 average. For Eq. 6.4 we used an average of the γ_0 values obtained in the whole MIPAS mission period.

We determined $d\chi_a/d\chi_b\big|_{tropopause}$, the slope of the correlation at the tropopause, according to the method suggested by [6]. We considered only the VMR monthly means of CFC-11 and CCl_4 at the SPARC pressure levels (see Sect. 6.6) above the tropopause. First of all, the mean correlation curve has been created calculating the mean of the CCl_4 data within 2 pptv of CFC-11 wide windows. The slope of the data has been calculated using a linear least squared fit within a moving window of 80 pptv of CFC-11. After the calculation, the moving window would be shifted forward by 5 pptv and the slope would be calculated again. The procedure was repeated for each 5 degrees latitudinal band. As suggested in [6] only CFC-11 VMRs greater than 120 pptv are considered. This approach makes us confident that the calculated slope is not affected by VMR values arising from the upper stratosphere. The remaining data were fitted using a second degree polynomial to calculate the value of the slope at the tropopause.

We calculated the VMR at the tropopause (σ_0) by averaging all the VMR monthly averages at the tropopause pressure level. The monthly means are then weighted using the corresponding atmospheric pressure. The atmospheric VMR ($\overline{\sigma}$) is calculated averaging the VMR monthly averages weighted with atmospheric pressure, in the pressure range between 200 and 20 hPa. The calculation of σ_0 and $\overline{\sigma}$ of CCl_4 and CFC-11 is carried-out separately for each latitudinal band, yielding a CCl_4 global average lifetime of 47(39 - 61) years, a lifetime of 49(40 - 63) years in the NH, and 46(38 - 60) years in the SH. We calculated the CCl_4 lifetime confidence interval by mapping through the calculations the CFC-11 lifetime confidence interval (see [92, 93] for more details). We also evaluated the impact of other possible error sources using a perturbative approach. We found that a 10% bias in the CCl_4 VMR retrieved from MIPAS (see Sect. 6.4) would cause an error of the order of $3 - 4\%$ in the CCl_4 lifetime. An uncertainty of ± 4.6 *ppt* yr^{-1} in $d\chi_b/d\Gamma\big|_{\Gamma=0}$ would cause an error smaller than 4% in the

CCl_4 lifetime. These contributions are by far smaller than the error implied by the uncertainty in the CFC-11 lifetime.

Our CCl_4 lifetime estimations are consistent with the most recent literature that suggests an atmospheric lifetime of 44(36 - 58) years [92, 93]. Several older studies report atmospheric CCl_4 lifetimes between 30 and 50 years [91, 88, 59, 110, 1]. [6] studied the stratospheric lifetime of several species (including CFC-11 and CCl_4) using ACE-FTS measurements. Using a CFC-11 lifetime of 45±7 [111] they calculated a CCl_4 global lifetime of 35±11 years. The difference with our results is explained taking into account the different reference CFC-11 lifetimes used: using the same CFC-11 lifetime [111] we would obtain a CCl_4 lifetime of 41±6 years. [6] report also very different lifetimes in the two hemispheres (41±9 years in the NH and 21±6 years in the SH) but they are not able to provide a solid justification for this finding. Again, the differences with our results are partially explained with the different CFC-11 lifetime considered (using the same CFC-11 lifetime [111] we would obtain a CCl_4 lifetime of 42±7 years in the NH and 40±6 years in the SH) but the choice of different reference lifetimes does not explain the hemispheric asymmetry reported in [6].

Chapter 7

Conclusions

The main target of this PhD thesis is the retrieval and the study of minor constituents of the middle atmosphere.

The analyses made during this thesis have been performed exploiting the measurements of the MIPAS instrument (Chap. 2). MIPAS is a limb-scanning Fourier transform spectrometer that operated onboard the polar-orbiting ESA ENVISAT from July 2002 to April 2012. MIPAS measured atmospheric limb emission radiance in the middle and upper atmosphere in the spectral range from 4.15 to 14.6 μm, covering almost the complete thermal infrared region in which emission lines of most atmospheric constituents are present. MIPAS provided a fundamental contribution to improve the knowledge of the chemistry and the dynamics of the middle atmosphere. MIPAS measurements were routinely processed by ESA using an online algorithm based on the ORM (Sect. 4.6). The retrieval was based on the non-linear least squares fit within selected spectral intervals (MWs). The vertical distribution of each geophysical parameter was retrieved simultaneously at all altitudes using the entire MIPAS limb scanning sequence. At the beginning of the mission, MIPAS measurements were exploited for the retrieval of some key chemical components, and, for this reason the retrieval sequence included "only" the joint retrieval of pressure and temperature, and the VMR of the H_2O, O_3, HNO_3, CH_4, N_2O and NO_2.

Over the years several authors have studied the possibility to retrieve the distribution of other minor constituents of the middle atmosphere from MIPAS measurements. Some of the minor species recently studied include CFC–11 [45], $ClONO_2$ [40], N_2O_5 [57], CFC–12 [45], COF_2 [35], CCl_4 [100],

HCN [29], HCFC–22 [15], H_2O_2 [63], C_2H_6 [105], H_2CO [94], C_2H_2 [64] and SO_2 [38]. These minor constituents give a minor contribution to the MIPAS spectra but their retrieval is fundamental to improve our general knowledge of the chemistry of the middle atmosphere. Moreover the retrieval and the study of these minor species allow a better characterization of the already known species due to possible mutual interferences. As a consequence of these studies, in the most recent version of MIPAS Level 2 data (Version 7), the list of retrieved molecules has been extended to include also CFC–11, $ClONO_2$, N_2O_5, CFC–12, COF_2, CCl_4, HCN, CFC–14, and HCFC–22.

In the first part of this PhD project, I worked on the retrieval of $COCl_2$ (Chap. 5). The $COCl_2$ global distribution in the UTLS was determined for the first time from MIPAS measurements [101]. $COCl_2$ was retrieved using an upgraded version of the ORM (Sect. 4.6) with the MTR functionality and the OE approach (Sect. 5.3). These upgrades allowed the $COCl_2$ and CFC–11 VMRs joint retrieval. This choice was crucial because of the weakness of $COCl_2$ spectral features and because of their mutual spectral interference with CFC–11. In order to get the best performances in the retrieval of $COCl_2$ VMR, new $COCl_2$ spectroscopic data have been tuned and an optimal set of MWs has been selected. To determine seasonal and latitudinal averages of phosgene VMR, more than 28000 profiles were retrieved from a set of MIPAS Level 1B Version 5 measurements acquired in the year 2008. $COCl_2$ mean seasonal VMR profiles show an evident latitudinal variability (Sect. 5.4). Largest values of the $COCl_2$ VMR (about 35 pptv) are found at the tropics at pressures around 30 hPa. At the mid-latitudes and at the poles, the VMR distribution is less peaked with highest values not exceeding 30 pptv. The results of this analysis were compared with ACE-FTS $COCl_2$ profiles co-located with the profiles retrieved using MIPAS observations (Sect. 5.5). The inter-comparison showed a good agreement between the two instruments, well within the combined systematic and random errors. MIPAS $COCl_2$ average seasonal profiles highlighted, for the first time, that the $COCl_2$ distribution in the UTLS has no seasonal variability apart from a somewhat weak seasonality at the poles. When this analysis was performed the most recent available version of the MIPAS level 1B data was version 5. Unfortunately that version of the data was affected by a small drifting calibration error induced by the non-linear behavior of the detectors [48]. This feature of MIPAS version 5 spectra prevented us to carry-out an

accurate trend analysis for this gas [21, 46].

In the second part of this PhD project, I studied the CCl_4 distribution in the UTLS region (Chap. 6). CCl_4 is a strong ozone-depleting substance, banned by the Montreal protocol starting from 1996. The analysis was performed using the CCl_4 official ESA Level 2 Version 7 products (Sect. 6.2).

The mean distribution of CCl_4 VMR shows the typical characteristics of long-lived species of anthropogenic origin that are primarily destroyed by photolysis (Sect. 6.3). The highest VMR values (higher than 100 pptv) are found in the lowermost sounded altitudes, and VMR monotonically decreases with increasing altitude. In the lower stratosphere, the largest values are observed at the tropics due to the intense updraft that occurs in the tropical region. The CCl_4 global distribution shows a seasonal variability in the polar regions due to CCl_4-poor mesospheric air subsidence induced by the polar vortex.

MIPAS CCl_4 VMR vertical profiles have been compared with those derived from other independent instruments, MIPAS-B and ACE-FTS (Sect. 6.4), and from EMAC model simulations (Sect. 6.5). MIPAS/ENVISAT measurements highlight a general good agreement (within 10%) with both instruments in the pressure range from 100 to 40 hPa. For pressures smaller than 40 hPa, MIPAS/ENVISAT CCl_4 values are between MIPAS-B and ACE–FTS. Within the 50°S-70°S latitude band, MIPAS shows a large negative bias with respect ACE–FTS. Further investigations have demonstrated that this bias is probably related with ACE–FTS products and it will be reduced in the upcoming version of the ACE–FTS products. For the comparison with EMAC model data, I used two different simulations performed from 1979 to 2013 with a spatial resolution of about $2.8° \times 2.8°$ and with 90 model levels. These simulations are performed with the so-called specified dynamics, in which the simulations are "nudged" towards the ERA – Interim re-analysis data in order to correct possible potential temperature biases and better simulate atmospheric dynamics. The comparison between CCl_4 ESA MIPAS and both EMAC RC1SD simulations shows a general good agreement, slightly better in the NH than in the SH. The largest differences are observed at the south pole, due to the presence of the polar vortex, and at the tropics, where vertical motions play a key role. At these latitudes the comparison highlights a better agreement considering the EMAC RC1SD-

Base-07 simulation, with the full nudging of the temperature, that is able to better reproduce the dynamics of the atmosphere and, as a consequence, the transport of CCl_4.

ESA MIPAS Level 2 version 7 products were produced using the new version of the MIPAS Level 1B spectra (version 7) which overcome the error caused by the imperfect instrument radiometric calibration using a new time-dependent correction scheme for detector non-linearities. Exploiting this new feature I had the opportunity to accurately evaluate CCl_4 trends as a function of latitude and altitude (Sect. 6.6). I observed negative trends of about $-10/-15$ pptv/decade ($-10/-30$ %/decade) at all latitudes in the UTLS region, with the exception of positive values of about 5/10 pptv/decade (15/20 %/decade) at mid-latitudes of the SH between 50 and 10 hPa. This positive stratospheric trend is probably caused by the less effective mixing mechanisms in the stratosphere with respect to the troposphere. In general, CCl_4 VMR values exhibit a greater decline rate for the NH than the SH. This asymmetry of the trend in the two hemispheres is probably related to the asymmetry in the general circulation of the atmosphere. The magnitude of the negative trend increases with altitude, more strongly in the NH, reaching values of 30-35%/decade at 50 hPa, close to the lifetime limited rate. The results of CCl_4 MIPAS trend analysis were compared with those estimated using ACE–FTS and surface networks, AGAGE and NOAA/ESRL/HATS, observations. Although surface network measurements cannot be properly compared with MIPAS observations, due to their lower altitude limit of 5-6 km, the comparison of the estimated trends highlights a general good agreement from the statistical point of view, mainly at mid-latitudes.

The interest on CCl_4 has recently increased as a consequence of the discrepancy between the atmospheric observations and the reported production and consumption ("the mystery of CCl_4", [93]), that demonstrated how CCl_4 concentration has declined at a rate almost three times smaller than its lifetime-limited rate. In order to contribute to the solution of this "mystery", I computed the CCl_4 stratospheric lifetime using the tracer-tracer linear correlation approach (Sect. 6.7). Considering CFC–11 as reference tracer, the calculation of the CCl_4 lifetime provides a global average lifetime of 47(39 - 61) years and a lifetime of 49(40 - 63) years for the NH and of 46(38 - 60) years for the SH. These results are consistent with the most

recent literature results of 44(36 - 58) years [92, 93].

List of Figures

List of Tables

Bibliography

[1] N. D. C. Allen, P. F. Bernath, C. D. Boone, M. P. Chipperfield, D. Fu, G. L. Manney, D. E. Oram, G. C. Toon, and D. K. Weisenstein. Global carbon tetrachloride distributions obtained from the Atmospheric Chemistry Experiment (ACE). *Atmospheric Chemistry and Physics*, 9(19):7449–7459, 2009.

[2] P. F. Bernath, C. T. McElroy, M. C. Abrams, C. D. Boone, M. Butler, C. Camy-Peyret, M. Carleer, C. Clerbaux, P.-F. Coheur, R. Colin, P. DeCola, M. DeMazière, J. R. Drummond, D. Dufour, W. F. J. Evans, H. Fast, D. Fussen, K. Gilbert, D. E. Jennings, E. J. Llewellyn, R. P. Lowe, E. Mahieu, J. C. McConnell, M. McHugh, S. D. McLeod, R. Michaud, C. Midwinter, R. Nassar, F. Nichitiu, C. Nowlan, C. P. Rinsland, Y. J. Rochon, N. Rowlands, K. Semeniuk, P. Simon, R. Skelton, J. J. Sloan, M.-A. Soucy, K. Strong, P. Tremblay, D. Turnbull, K. A. Walker, I. Walkty, D. A. Wardle, V. Wehrle, R. Zander, and J. Zou. Atmospheric Chemistry Experiment (ACE): Mission overview. *Geophysical Research Letters*, 32(15), 2005. L15S01.

[3] C. D. Boone, R. Nassar, K. A. Walker, Y. Rochon, S. D. McLeod, C. P. Rinsland, and P. F. Bernath. Retrievals for the Atmospheric Chemistry Experiment–Fourier Transform Spectrometer. *Appl. Opt.*, 44(33):7218–7231, 2005.

[4] C. D. Boone, K. A. Walker, and P. F. Bernath. Version 3 retrievals for the Atmospheric Chemistry Experiment Fourier Transform Spectrometer (ACE-FTS). *The Atmospheric Chemistry Experiment (ACE)*, 10:103–127, 2013.

[5] A. T. Brown, M. P. Chipperfield, C. Boone, C. Wilson, K. A. Walker, and P. F. Bernath. Trends in atmospheric halogen containing gases

since 2004. *Journal of Quantitative Spectroscopy and Radiative Transfer*, 112(16):2552 – 2566, 2011.

[6] A. T. Brown, C. M. Volk, M. R. Schoeberl, C. D. Boone, and P. F. Bernath. Stratospheric lifetimes of CFC–12, CCl_4, CH_4, CH_3Cl and N_2O from measurements made by the Atmospheric Chemistry Experiment-Fourier Transform Spectrometer (ACE-FTS). *Atmospheric Chemistry and Physics*, 13(14):6921–6950, 2013.

[7] L. R. Brown, M. R. Gunson, R. A. Toth, F. W. Irion, C. P. Rinsland, and A. Goldman. The 1995 Atmospheric Trace Molecule Spectroscopy (ATMOS) linelist. *Appl. Opt.*, 35:2828–2848, 1996.

[8] J. H. Butler, S. A. Yvon-Lewis, J. M. Lobert, D. B. King, S. A. Montzka, J. L. Bullister, V. Koropalov, J. W. Elkins, B. D. Hall, L. Hu, and Y. Liu. A comprehensive estimate for loss of atmospheric carbon tetrachloride (CCl_4) to the ocean. *Atmospheric Chemistry and Physics*, 16(17):10899–10910, 2016.

[9] M. Carlotti. Global-fit approach to the analysis of limb-scanning atmospheric measurements. *Appl. Opt.*, 27(15):3250–3254, Aug 1988.

[10] L. J. Carpenter, S. Reimann, J. B. Burkholder, C. Clerbaux, B. D. Hall, R. Hossaini, J. C. Laube, and S. A. Yvon-Lewis. Update on Ozone-Depleting Substances (ODSs) and Other Gases of Interest to the Montreal Protocol. In Global Ozone Research and Report No. 55 Monitoring Project, editors, *Scientific Assessment of Ozone Depletion: 2014*, chapter 1. World Meteorological Organization, Geneva, Switzerland, 2014.

[11] E. Castelli, M. Ridolfi, M. Carlotti, B.-M. Sinnhuber, O. Kirner, M. Kiefer, and B. M. Dinelli. Errors induced by different approximations in handling horizontal atmospheric inhomogeneities in MIPAS/ENVISAT retrievals. *Atmospheric Measurement Techniques*, 9(11):5499–5508, 2016.

[12] S. Ceccherini and M. Ridolfi. Technical note: Variance-covariance matrix and averaging kernels for the Levenberg-Marquardt solution of the retrieval of atmospheric vertical profiles. *Atmospheric Chemistry and Physics*, 10(6):3131–3139, 2010.

[13] S. Chapman. A theory of upper-atmospheric ozone. *Mem. of the Royal Met. Soc.*, 4:26, 1930.

[14] M. P. Chipperfield, Q. Liang, M. Rigby, R. Hossaini, S. A. Montzka, S. Dhomse, W. Feng, R. G. Prinn, R. F. Weiss, C. M. Harth, P. K. Salameh, J. Mühle, S. O'Doherty, D. Young, P. G. Simmonds, P. B. Krummel, P. J. Fraser, L. P. Steele, J. D. Happell, R. C. Rhew, J. Butler, S. A. Yvon-Lewis, B. Hall, D. Nance, F. Moore, B. R. Miller, J. W. Elkins, J. J. Harrison, C. D. Boone, E. L. Atlas, and E. Mahieu. Model sensitivity studies of the decrease in atmospheric carbon tetrachloride. *Atmospheric Chemistry and Physics*, 16(24):15741–15754, 2016.

[15] M. Chirkov, G. P. Stiller, A. Laeng, S. Kellmann, T. von Clarmann, C. D. Boone, J. W. Elkins, A. Engel, N. Glatthor, U. Grabowski, C. M. Harth, M. Kiefer, F. Kolonjari, P. B. Krummel, A. Linden, C. R. Lunder, B. R. Miller, S. A. Montzka, J. Mühle, S. O'Doherty, J. Orphal, R. G. Prinn, G. Toon, M. K. Vollmer, K. A. Walker, R. F. Weiss, A. Wiegele, and D. Young. Global HCFC–22 measurements with MIPAS: retrieval, validation, global distribution and its evolution over 2005–2012. *Atmospheric Chemistry and Physics*, 16(5):3345–3368, 2016.

[16] D. P. Dee, S. M. Uppala, A. J. Simmons, P. Berrisford, P. Poli, S. Kobayashi, U. Andrae, M. A. Balmaseda, G. Balsamo, P. Bauer, P. Bechtold, A. C. M. Beljaars, L. van de Berg, J. Bidlot, N. Bormann, C. Delsol, R. Dragani, M. Fuentes, A. J. Geer, L. Haimberger, S. B. Healy, H. Hersbach, E. V. Hlm, L. Isaksen, P. Kllberg, M. Khler, M. Matricardi, A. P. McNally, B. M. Monge-Sanz, J.-J. Morcrette, B.-K. Park, C. Peubey, P. de Rosnay, C. Tavolato, J.-N. Thpaut, and F. Vitart. The ERA-Interim reanalysis: configuration and performance of the data assimilation system. *Quarterly Journal of the Royal Meteorological Society*, 137(656):553–597, 2011.

[17] B. M. Dinelli, E. Castelli, B. Carli, S. Del Bianco, M. Gai, L. Santurri, B. P. Moyna, M. Oldfield, R. Siddans, D. Gerber, W. J. Reburn, B. J. Kerridge, and C. Keim. Technical note: Measurement of the tropical UTLS composition in presence of clouds using millimetre-

wave heterodyne spectroscopy. *Atmospheric Chemistry and Physics*, 9(4):1191–1207, 2009.

[18] B.M. Dinelli, D. Alpaslan, M. Carlotti, L. Magnani, and M. Ridolfi. Multi-target retrieval (MTR): the simultaneous retrieval of pressure, temperature and volume mixing ratio profiles from limb-scanning atmospheric measurements. *Journal of Quantitative Spectroscopy and Radiative Transfer*, 84(2):141 – 157, 2004.

[19] A. Dudhia, V. L. Jay, and C. D. Rodgers. Microwindow selection for high-spectral-resolution sounders. *Appl. Opt.*, 41(18):3665–3673, Jun 2002.

[20] E. Eckert, A. Laeng, S. Lossow, S. Kellmann, G. Stiller, T. von Clarmann, N. Glatthor, M. Höpfner, M. Kiefer, H. Oelhaf, J. Orphal, B. Funke, U. Grabowski, F. Haenel, A. Linden, G. Wetzel, W. Woiwode, P. F. Bernath, C. Boone, G. S. Dutton, J. W. Elkins, A. Engel, J. C. Gille, F. Kolonjari, T. Sugita, G. C. Toon, and K. A. Walker. MIPAS IMK/IAA CFC–11 (CCl_3F) and CFC–12 (CCl_2F_2) measurements: accuracy, precision and long-term stability. *Atmospheric Measurement Techniques*, 9(7):3355–3389, 2016.

[21] E. Eckert, T. von Clarmann, M. Kiefer, G. P. Stiller, S. Lossow, N. Glatthor, D. A. Degenstein, L. Froidevaux, S. Godin-Beekmann, T. Leblanc, S. McDermid, M. Pastel, W. Steinbrecht, D. P. J. Swart, K. A. Walker, and P. F. Bernath. Drift-corrected trends and periodic variations in MIPAS IMK/IAA ozone measurements. *Atmospheric Chemistry and Physics*, 14(5):2571–2589, 2014.

[22] M. Endemann. MIPAS, the Michelson Interferometer for Passive Atmospheric Sounding for the EnviSat Satellite. In *Fourier Transform Spectroscopy/ Hyperspectral Imaging and Sounding of the Environment*, pages n/a–n/a. Optical Society of America, 2005.

[23] A. Engel, H. Bönisch, T. Schwarzenberger, H. P. Haase, K. Grunow, J. Abalichin, and S. Sala. Long term validation of ESA operational retrieval (version 6.0) of MIPAS Envisat vertical profiles of methane, nitrous oxides, CFC–11 and CFC–12 using balloon borne observations

and trajectory matching. *Atmospheric Measurement Techniques Discussions*, 8(7):7455–7489, 2015.

[24] P. B. Fellgett. *Doctoral Thesis (unpublished),* Univ. of Cambridge(1951). Proceeding of Ohio State Symposium on Molecular Spectroscopy, 1952.

[25] H. Fischer, M. Birk, C. Blom, B. Carli, M. Carlotti, T. von Clarmann, L. Delbouille, A. Dudhia, D. Ehhalt, M. Endemann, J. M. Flaud, R. Gessner, A. Kleinert, R. Koopman, J. Langen, M. López-Puertas, P. Mosner, H. Nett, H. Oelhaf, G. Perron, J. Remedios, M. Ridolfi, G. Stiller, and R. Zander. MIPAS: an instrument for atmospheric and climate research. *Atmospheric Chemistry and Physics*, 8(8):2151–2188, 2008.

[26] J.-M. Flaud, C. Piccolo, B. Carli, A. Perrin, L.H. Coudert, J.-L. Teffo, and L.R. Brown. Molecular line parameters for the MIPAS (Michelson Interferometer for Passive Atmospheric Sounding) experiment. *J. Atm. and Ocean Optics*, (16):172–182, 2003.

[27] F. Friedl-Vallon, G. Maucher, M. Seefeldner, O. Trieschmann, A. Kleinert, A. Lengel, C. Keim, H. Oelhaf, and H. Fischer. Design and characterization of the balloon-borne Michelson Interferometer for Passive Atmospheric Sounding (MIPAS-B2). *Appl. Opt.*, 43(16):3335–3355, Jun 2004.

[28] D. Fu, C. D. Boone, P. F. Bernath, K. A. Walker, R. Nassar, G. L. Manney, and S. D. McLeod. Global phosgene observations from the Atmospheric Chemistry Experiment (ACE) mission. *Geophysical Research Letters*, 34(17):n/a–n/a, 2007. L17815.

[29] N. Glatthor, M. Höpfner, G. P. Stiller, T. von Clarmann, B. Funke, S. Lossow, E. Eckert, U. Grabowski, S. Kellmann, A. Linden, K. A. Walker, and A. Wiegele. Seasonal and interannual variations in HCN amounts in the upper troposphere and lower stratosphere observed by MIPAS. *Atmospheric Chemistry and Physics*, 15(2):563–582, 2015.

[30] A. Goldman and R.S. Saunders. Analysis of atmospheric infrared spectra for altitude distribution of atmospheric trace constituents I.

method of analysis. *Journal of Quantitative Spectroscopy and Radiative Transfer*, 21(2):155 – 161, 1979.

[31] F. Graziosi, J. Arduini, P. Bonasoni, F. Furlani, U. Giostra, A. J. Manning, A. McCulloch, S. O'Doherty, P. G. Simmonds, S. Reimann, M. K. Vollmer, and M. Maione. Emissions of Carbon Tetrachloride (CCl_4) from Europe. *Atmospheric Chemistry and Physics Discussions*, 2016:1–24, 2016.

[32] F. J. Haenel, G. P. Stiller, T. von Clarmann, B. Funke, E. Eckert, N. Glatthor, U. Grabowski, S. Kellmann, M. Kiefer, A. Linden, and T. Reddmann. Reassessment of MIPAS age of air trends and variability. *Atmospheric Chemistry and Physics*, 15(22):13161–13176, 2015.

[33] N. R. P. Harris, D. J. Wuebbles, J. S. Daniel, J. Hu, L. J. M. Kuijpers, K. S. Law, M. J. Prather, and R. Schofield. Scenarios and information for policy makers. In Global Ozone Research and Report No. 55 Monitoring Project, editors, *Scientific Assessment of Ozone Depletion: 2014*, chapter 5. World Meteorological Organization, Geneva, Switzerland, 2014.

[34] J. J. Harrison, M. P. Chipperfield, C. D. Boone, S. S. Dhomse, P. F. Bernath, L. Froidevaux, J. Anderson, and J. Russell III. Satellite observations of stratospheric hydrogen fluoride and comparisons with SLIMCAT calculations. *Atmospheric Chemistry and Physics*, 16(16):10501–10519, 2016.

[35] J. J. Harrison, M. P. Chipperfield, A. Dudhia, S. Cai, S. Dhomse, C. D. Boone, and P. F. Bernath. Satellite observations of stratospheric carbonyl fluoride. *Atmospheric Chemistry and Physics*, 14(21):11915–11933, 2014.

[36] M. Hegglin and S. Tegtmeier. The SPARC Data Initiative. *SPARC Newsletter*, 36:22–23, 2011.

[37] HITRAN. HIgh-resolution TRANsmission, 2017.

[38] M. Höpfner, C. D. Boone, B. Funke, N. Glatthor, U. Grabowski, A. Günther, S. Kellmann, M. Kiefer, A. Linden, S. Lossow, H. C. Pumphrey, W. G. Read, A. Roiger, G. Stiller, H. Schlager, T. von

Clarmann, and K. Wissmüller. Sulfur dioxide (SO_2) from MIPAS in the upper troposphere and lower stratosphere 2002–2012. *Atmospheric Chemistry and Physics*, 15(12):7017–7037, 2015.

[39] M. Höpfner, H. Oelhaf, G. Wetzel, F. Friedl-Vallon, A. Kleinert, A. Lengel, G. Maucher, H. Nordmeyer, N. Glatthor, G. Stiller, T. v. Clarmann, H. Fischer, C. Kröger, and T. Deshler. Evidence of scattering of tropospheric radiation by PSCs in mid-IR limb emission spectra: MIPAS-B observations and KOPRA simulations. *Geophysical Research Letters*, 29(8):119–1–119–4, 2002.

[40] M. Höpfner, T. von Clarmann, H. Fischer, N. Glatthor, U. Grabowski, S. Kellmann, M. Kiefer, A. Linden, G. Mengistu Tsidu, M. Milz, T. Steck, G. P. Stiller, D. Y. Wang, and B. Funke. First spaceborne observations of Antarctic stratospheric $ClONO_2$ recovery: Austral spring 2002. *Journal of Geophysical Research: Atmospheres*, 109(D11):n/a–n/a, 2004. D11308.

[41] J. Houghton. *The physics of atmospheres*. Cambridge University Press, 2002.

[42] P. Jacquinot. The luminosity of spectrometers with prisms, gratings, or Fabry-Perot etalons. *J. Opt. Soc. Am.*, 44(10):761–765, Oct 1954.

[43] P. Jöckel, H. Tost, A. Pozzer, C. Brühl, J. Buchholz, L. Ganzeveld, P. Hoor, A. Kerkweg, M. G. Lawrence, R. Sander, B. Steil, G. Stiller, M. Tanarhte, D. Taraborrelli, J. van Aardenne, and J. Lelieveld. The atmospheric chemistry general circulation model ECHAM5/MESSy1: consistent simulation of ozone from the surface to the mesosphere. *Atmospheric Chemistry and Physics*, 6(12):5067–5104, 2006.

[44] P. Jöckel, H. Tost, A. Pozzer, M. Kunze, O. Kirner, C. A. M. Brenninkmeijer, S. Brinkop, D. S. Cai, C. Dyroff, J. Eckstein, F. Frank, H. Garny, K.-D. Gottschaldt, P. Graf, V. Grewe, A. Kerkweg, B. Kern, S. Matthes, M. Mertens, S. Meul, M. Neumaier, M. Nützel, S. Oberländer-Hayn, R. Ruhnke, T. Runde, R. Sander, D. Scharffe, and A. Zahn. Earth System Chemistry integrated Modelling (ESCiMo) with the Modular Earth Submodel System (MESSy) version 2.51. *Geoscientific Model Development*, 9(3):1153–1200, 2016.

[45] S. Kellmann, T. von Clarmann, G. P. Stiller, E. Eckert, N. Glatthor, M. Höpfner, M. Kiefer, J. Orphal, B. Funke, U. Grabowski, A. Linden, G. S. Dutton, and J. W. Elkins. Global CFC-11 (CCl_3F) and CFC–12 (CCl_2F_2) measurements with the Michelson Interferometer for Passive Atmospheric Sounding (MIPAS): retrieval, climatologies and trends. *Atmospheric Chemistry and Physics*, 12(24):11857–11875, 2012.

[46] M. Kiefer, G. Aubertin, M. Birk, M. de Laurentis, E. Eckert, A. Kleinert, G. Perron, and G. Wagner. *Impact of Improved Corrections for MIPAS Detector Non-Linearity, Atmospheric Composition Validation and Evolution.* Number 38. ESA, Abstract Book, Frascati, March 2013.

[47] T. P. Kindler, W. L. Chameides, P. H. Wine, D. M. Cunnold, F. N. Alyea, and J. A. Franklin. The fate of atmospheric phosgene and the stratospheric chlorine loadings of its parent compounds: CCl_4, C_2Cl_4, C_2HCl_3, CH_3CCl_3, and $CHCl_3$. *Journal of Geophysical Research: Atmospheres*, 100(D1):1235–1251, 1995.

[48] A. Kleinert, G. Aubertin, G. Perron, M. Birk, G. Wagner, F. Hase, H. Nett, and R. Poulin. MIPAS Level 1B algorithms overview: operational processing and characterization. *Atmospheric Chemistry and Physics*, 7(5):1395–1406, 2007.

[49] F. Kwabia-Tchana, W. J. Lafferty, J.-M. Flaud, L. Manceron, and M. Ndao. High-resolution analysis of the $\nu 1$ and $\nu 5$ bands of phosgene $^{35}Cl_2CO$ and $^{35}Cl^{37}ClCO$. *Molecular Physics*, 113(21):3241–3246, 2015.

[50] E. Kyrölä, J. Tamminen, V. Sofieva, J. L. Bertaux, A. Hauchecorne, F. Dalaudier, D. Fussen, F. Vanhellemont, O. Fanton d'Andon, G. Barrot, M. Guirlet, T. Fehr, and L. Saavedra de Miguel. GOMOS O_3, NO_2, and NO_3 observations in 2002–2008. *Atmospheric Chemistry and Physics*, 10(16):7723–7738, 2010.

[51] J. C. Laube, A. Keil, H. Bönisch, A. Engel, T. Röckmann, C. M. Volk, and W. T. Sturges. Observation-based assessment of stratospheric fractional release, lifetimes, and ozone depletion potentials

of ten important source gases. *Atmospheric Chemistry and Physics*, 13(5):2779–2791, 2013.

[52] K. Levenberg. A method for the solution of certain non-linear problems in least squares. *Quart. Appl. Math.*, 2:164, 1944.

[53] Q. Liang, P. A. Newman, J. S. Daniel, S. Reimann, B. D. Hall, G. Dutton, and L. J. M. Kuijpers. Constraining the carbon tetrachloride (CCl_4) budget using its global trend and inter-hemispheric gradient. *Geophysical Research Letters*, 41(14):5307–5315, 2014. 2014GL060754.

[54] J. E. Lovelock, R. J. Maggs, and R. J. Wade. Halogenated hydrocarbons in and over the atlantic. *Nature*, 241:194–196, 1973.

[55] E. Mahieu, M. P. Chipperfield, J. Notholt, T. Reddmann, J. Anderson, P. F. Bernath, T. Blumenstock, M. T. Coffey, S. S. Dhomse, W. Feng, B. Franco, L. Froidevaux, D. W. T. Griffith, J. W. Hannigan, F. Hase, R. Hossaini, N. B. Jones, I. Morino, I. Murata, H. Nakajima, M. Palm, C. Paton-Walsh, J. M. Russell III, M. Schneider, C. Servais, D. Smale, and K. A. Walker. Recent northern hemisphere stratospheric HCl increase due to atmospheric circulation changes. *Nature*, 515(7525):104–107, 11 2014.

[56] D. W. Marquardt. An algorithm for the least-squares estimation of nonlinear parameters. *J. Soc. Appl. Math.*, 11:431, 1963.

[57] G. Mengistu Tsidu, T. von Clarmann, G. P. Stiller, M. Höpfner, H. Fischer, N. Glatthor, U. Grabowski, S. Kellmann, M. Kiefer, A. Linden, M. Milz, T. Steck, D. Y. Wang, and B. Funke. Stratospheric n_2o_5 in the austral spring 2002 as retrieved from limb emission spectra recorded by the Michelson Interferometer for Passive Atmospheric Sounding (MIPAS). *Journal of Geophysical Research: Atmospheres*, 109(D18):n/a–n/a, 2004. D18301.

[58] ML2PP. Readme file of MIPAS ESA Level 2 products Version 6 - ENVI-GSOP-EOGD-QD-12-0116. 2012.

[59] S. A. Montzka, J. H. Butler, J.W. Elkins, T. M. Thompson, A. D. Clarke, and L. T. Lock. Present and future trends in the atmospheric burden of ozone-depleting halogens. *Nature*, 398:690–694, 1999.

[60] B. Naujokat and K. Grunow. The stratospheric Arctic winter 2002/03: balloon flight planning by trajectory calculations. In *Proceedings of the 16th ESA Symposium on European Rocket and Balloon Programmes and Related Research*, pages 421–425, St. Gallen, 2003. ESA SP-530.

[61] R. H. Norton and R. Beer. New apodizing functions for fourier spectrometry. *J. Opt. Soc. Am.*, 67:419, 1977. and errata corrige *J. Opt. Soc. Am.* **67**, 419 (1977).

[62] Oxford University. MIPAS website, 2016. Lastchecked on 2017-12-10.

[63] E. Papandrea, A. Dudhia, R. G. Grainger, X. Vancassel, and M. P. Chipperfield. Retrieval of global hydrogen peroxide (H_2O_2) profiles using ENVISAT-MIPAS. *Geophysical Research Letters*, 32(14):n/a–n/a, 2005. L14809.

[64] R. J. Parker, J. J. Remedios, D. P. Moore, and V. P. Kanawade. Acetylene C_2H_2 retrievals from MIPAS data and regions of enhanced upper tropospheric concentrations in august 2003. *Atmospheric Chemistry and Physics*, 11(19):10243–10257, 2011.

[65] A. Perrin, J.-M. Flaud, M. Ridolfi, J. Vanderâ Auwera, and M. Carlotti. MIPAS database: new HNO_3 line parameters at 7.6 μm validated with MIPAS satellite measurements. *Atmospheric Measurement Techniques*, 9(5):2067–2076, 2016.

[66] F. Ploeger, M. Riese, F. Haenel, P. Konopka, R. Mller, and G. Stiller. Variability of stratospheric mean age of air and of the local effects of residual circulation and eddy mixing. *Journal of Geophysical Research: Atmospheres*, 120(2):716–733, 2015. 2014JD022468.

[67] R. A. Plumb. Tracer interrelationships in the stratosphere. *Reviews of Geophysics*, 45(4):n/a–n/a, 2007. RG4005.

[68] R. A. Plumb and M. K. W. Ko. Interrelationships between mixing ratios of long-lived stratospheric constituents. *Journal of Geophysical Research: Atmospheres*, 97(D9):10145–10156, 1992.

[69] R. A. Plumb and X. Zheng. Source determination from trace gas observations: An orthogonal function approach and results for long-

lived gases with surface sources. *Journal of Geophysical Research: Atmospheres*, 101(D13):18569–18585, 1996.

[70] R. G. Prinn, R. F. Weiss, P. J. Fraser, P. G. Simmonds, D. M. Cunnold, F. N. Alyea, S. O'Doherty, P. Salameh, B. R. Miller, J. Huang, R. H. J. Wang, D. E. Hartley, C. Harth, L. P. Steele, G. Sturrock, P. M. Midgley, and A. McCulloch. A history of chemically and radiatively important gases in air deduced from ALE/GAGE/AGAGE. *Journal of Geophysical Research: Atmospheres*, 105(D14):17751–17792, 2000.

[71] R. G. Prinn, R. F. Weiss, Fraser P. J., P. G. Simmonds, D. M. Cunnold, S. O'Doherty, P. K. Salameh, L. W. Porter, P. B. Krummel, R. H. J. Wang, B. R. Miller, C. Harth, B. R. Greally, F. A. Van Woy, L. P. Steele, J. Mühle, G. A. Sturrock, F. N. Alyea, J. Huang, and D. E. Hartley. The ALE / GAGE AGAGE network, carbon dioxide information analysis center (CDIAC), Oak Ridge National Laboratory (ORNL). U.S. Department of Energy (DOE), 2016.

[72] P. Raspollini, C. Belotti, A. Burgess, B. Carli, M. Carlotti, S. Ceccherini, B. M. Dinelli, A. Dudhia, J.-M. Flaud, B. Funke, M. Höpfner, M. López-Puertas, V. Payne, C. Piccolo, J. J. Remedios, M. Ridolfi, and R. Spang. MIPAS level 2 operational analysis. *Atmospheric Chemistry and Physics*, 6(12):5605–5630, 2006.

[73] P. Raspollini, B. Carli, M. Carlotti, S. Ceccherini, A. Dehn, B. M. Dinelli, A. Dudhia, J.-M. Flaud, M. López-Puertas, F. Niro, J. J. Remedios, M. Ridolfi, H. Sembhi, L. Sgheri, and T. von Clarmann. Ten years of MIPAS measurements with ESA Level 2 processor V6 - Part 1: Retrieval algorithm and diagnostics of the products. *Atmospheric Measurement Techniques*, 6(9):2419–2439, 2013.

[74] J. J. Remedios, R. J. Leigh, A. M. Waterfall, D. P. Moore, H. Sembhi, I. Parkes, J. Greenhough, M.P. Chipperfield, and D. Hauglustaine. MIPAS reference atmospheres and comparisons to V4.61/V4.62 MIPAS level 2 geophysical data sets. *Atmospheric Chemistry and Physics Discussions*, 7(4):9973–10017, 2007.

[75] R. C. Rhew and J. D. Happell. The atmospheric partial lifetime of carbon tetrachloride with respect to the global soil sink. *Geophysical Research Letters*, 43(6):2889–2895, 2016. 2016GL067839.

[76] M. Ridolfi, B. Carli, M. Carlotti, T. von Clarmann, B. M. Dinelli, A. Dudhia, J.-M. Flaud, M. Höpfner, P. E. Morris, P. Raspollini, G. Stiller, and R. J. Wells. Optimized Forward Model and Retrieval Scheme for MIPAS Near-Real-Time Data Processing. *Appl. Opt.*, 39:1323–1340, March 2000.

[77] C. P. Rinsland, E. Mahieu, P. Demoulin, R. Zander, C. Servais, and J.-M. Hartmann. Decrease of the carbon tetrachloride (CCl_4) loading above Jungfraujoch, based on high resolution infrared solar spectra recorded between 1999 and 2011. *Journal of Quantitative Spectroscopy and Radiative Transfer*, 113(11):1322 – 1329, 2012.

[78] C. D. Rodgers. *Inverse methods for atmospheric sounding: Theory and Practice*, volume 2 of *Series on Atmospheric, Oceanic and Planetary Physics*. World Scientific Publishing Co., Singapore, 2000.

[79] E. Roeckner, R. Brokopf, M. Esch, M. Giorgetta, S. Hagemann, L. Kornblueh, E. Manzini, U. Schlese, and U. Schulzweida. Sensitivity of simulated climate to horizontal and vertical resolution in the ECHAM5 atmosphere model. *Journal of Climate*, 19(16):3771–3791, 2006.

[80] L. S. Rothman, D. Jacquemart, A. Barbe, D. Chris Benner, M. Birk, L. R. Brown, M. R. Carleer, C. Chackerian Jr., K. Chance, L. H. Coudert, V. Dana, V. M. Devi, J.-M. Flaud, R. R. Gamache, A. Goldman, J.-M. Hartmann, K. W. Jucks, A. G. Maki, J.-Y. Mandin, S. T. Massie, J. Orphal, A. Perrin, C. P. Rinsland, M. A. H. Smith, J. Tennyson, R. N. Tolchenov, R. A. Toth, J. Vander Auwera, P. Varanasi, and G. Wagner. The HITRAN 2004 molecular spectroscopic database. *Journal of Quantitative Spectroscopy and Radiative Transfer*, 96(2):139 – 204, 2005.

[81] L. S. Rothman, C. P. Rinsland, A. Goldman, S. T. Massie, D. P. Edwards, J-M. Flaud, A. Perrin, C. Camy-Peyret, V. Dana, J.-Y. Mandin, J. Schroeder, A. McCann, R. R. Gamache, R. B. Wattson, K. Yoshino, K. V. Chance, K. W. Jucks, L. R. Brown, V. Nemtchinov,

and P. Varanasi. The HITRAN molecular spectroscopic database and HAWKS (HITRAN Atmospheric Workstation): 1996 Edition. *Journal of Quantitative Spectroscopy and Radiative Transfer*, 60(5):665–710, 1998.

[82] L.S. Rothman, I.E. Gordon, Y. Babikov, A. Barbe, D. Chris Benner, P.F. Bernath, M. Birk, L. Bizzocchi, V. Boudon, L.R. Brown, A. Campargue, K. Chance, E.A. Cohen, L.H. Coudert, V.M. Devi, B.J. Drouin, A. Fayt, J.-M. Flaud, R.R. Gamache, J.J. Harrison, J.-M. Hartmann, C. Hill, J.T. Hodges, D. Jacquemart, A. Jolly, J. Lamouroux, R.J. Le Roy, G. Li, D.A. Long, O.M. Lyulin, C.J. Mackie, S.T. Massie, S. Mikhailenko, H.S.P. Mller, O.V. Naumenko, A.V. Nikitin, J. Orphal, V. Perevalov, A. Perrin, E.R. Polovtseva, C. Richard, M.A.H. Smith, E. Starikova, K. Sung, S. Tashkun, J. Tennyson, G.C. Toon, Vl.G. Tyuterev, and G. Wagner. The HITRAN 2012 molecular spectroscopic database. *Journal of Quantitative Spectroscopy and Radiative Transfer*, 130(Supplement C):4 – 50, 2013. HITRAN2012 special issue.

[83] L.S. Rothman, I.E. Gordon, A. Barbe, D.Chris Benner, P.F. Bernath, M. Birk, V. Boudon, L.R. Brown, A. Campargue, J.-P. Champion, K. Chance, L.H. Coudert, V. Dana, V.M. Devi, S. Fally, J.-M. Flaud, R.R. Gamache, A. Goldman, D. Jacquemart, I. Kleiner, N. Lacome, W.J. Lafferty, J.-Y. Mandin, S.T. Massie, S.N. Mikhailenko, C.E. Miller, N. Moazzen-Ahmadi, O.V. Naumenko, A.V. Nikitin, J. Orphal, V.I. Perevalov, A. Perrin, A. Predoi-Cross, C.P. Rinsland, M. Rotger, M. Šimečková, M.A.H. Smith, K. Sung, S.A. Tashkun, J. Tennyson, R.A. Toth, A.C. Vandaele, and J. Vander Auwera. The HITRAN 2008 molecular spectroscopic database. *Journal of Quantitative Spectroscopy and Radiative Transfer*, 110(9–10):533 – 572, 2009.

[84] R. Sander, A. Baumgaertner, S. Gromov, H. Harder, P. Jöckel, A. Kerkweg, D. Kubistin, E. Regelin, H. Riede, A. Sandu, D. Taraborrelli, H. Tost, and Z.-Q. Xie. The atmospheric chemistry box model CAABA/MECCA-3.0. *Geoscientific Model Development*, 4(2):373–380, 2011.

[85] U. Schmidt, G. Kulessa, E. Klein, E.-P. Roeth, and P. Fabian. Intercomparison of ballloon-borne cryogenic whole air samplers during the MAP/GLOBUS 1983 campaign. *Planetary and Space Science*, 35:647–656, May 1987.

[86] S. W. Sharpe, T. J. Johnson, R. L. Sams, P. M. Chu, G. C. Rhoderick, and P. A. Johnson. Gas-phase databases for quantitative infrared spectroscopy. *Applied Spectroscopy*, 58(12):1452–1461, 2004.

[87] P. E. Sheese, C. D. Boone, and K. A. Walker. Detecting physically unrealistic outliers in ACE–FTS atmospheric measurements. *Atmospheric Measurement Techniques*, 8(2):741–750, 2015.

[88] P. G. Simmonds, D. M. Cunnold, F. N. Alyea, C. A. Cardelino, A. J. Crawford, R. G. Prinn, P. J. Fraser, R. A. Rasmussen, and R. D. Rosen. Carbon tetrachloride lifetimes and emissions determined from daily global measurements during 1978–1985. *Journal of atmospheric chemistry*, 7(1):35–58, 1988.

[89] P. G. Simmonds, D. M. Cunnold, R. F. Weiss, R. G. Prinn, P. J. Fraser, A. McCulloch, F. N. Alyea, and S. O'Doherty. Global trends and emission estimates of CCl_4 from in situ background observations from July 1978 to June 1996. *Journal of Geophysical Research: Atmospheres*, 103(D13):16017–16027, 1998.

[90] H. B. Singh. Phosgene in the ambient air. *Nature*, 264(5585):428–429, 12 1976.

[91] H. B. Singh, D. P. Fowler, and T. O. Peyton. Atmospheric carbon tetrachloride: Another man-made pollutant. *Science*, 192(4245):1231–1234, 1976.

[92] SPARC. Sparc report on the lifetimes of stratospheric ozone-deleting substances, their replacements, and related species. M.K.W. Ko, P.A. Newman, S. Reimann, S.E. Strahan (eds.), available at `www.sparc-climate.org/publications/sparc-reports/sparc-report-no6`, 2013.

[93] SPARC. Sparc report on the mystery of carbon tetrachloride. SPARC Report No. 7, WCRP-13/2016. Liang Q. and Newman

P.A. and S. Reimann (eds.), available at: `www.sparc-climate.org/publications/sparc-reports/sparc-report-no7`, 2016.

[94] T. Steck, N. Glatthor, T. von Clarmann, H. Fischer, J. M. Flaud, B. Funke, U. Grabowski, M. Höpfner, S. Kellmann, A. Linden, A. Perrin, and G. P. Stiller. Retrieval of global upper tropospheric and stratospheric formaldehyde (H_2CO) distributions from high-resolution MIPAS-Envisat spectra. *Atmospheric Chemistry and Physics*, 8(3):463–470, 2008.

[95] T. Steck and T. von Clarmann. Constrained Profile Retrieval Applied to the Observation Mode of the Michelson Interferometer for Passive Atmospheric Sounding. *Appl. Opt.*, 40:3559–3571, July 2001.

[96] G. P. Stiller, T. von Clarmann, F. Haenel, B. Funke, N. Glatthor, U. Grabowski, S. Kellmann, M. Kiefer, A. Linden, S. Lossow, et al. Observed temporal evolution of global mean age of stratospheric air for the 2002 to 2010 period. *Atmospheric Chemistry and Physics*, 12(7):3311–3331, 2012.

[97] G. P. Stiller, T. von Clarmann, B. Funke, N. Glatthor, F. Hase, M. Höpfner, and A. Linden. Sensitivity of trace gas abundances retrievals from infrared limb emission spectra to simplifying approximations in radiative transfer modelling. *Journal of Quantitative Spectroscopy and Radiative Transfer*, 72(3):249 – 280, 2002.

[98] L. L. Strow, H. E. Motteler, R.G. Benson, S.E. Hannon, and S. De Souza-Machado. Fast computation of monochromatic infrared atmospheric transmittances using compressed look-up tables. *J. Quant. Spectrosc. Radiat. Transfer*, 59:481, 1998.

[99] G. C. Toon, J.-F. Blavier, B. Sen, and B. J. Drouin. Atmospheric $COCl_2$ measured by solar occultation spectrometry. *Geophysical Research Letters*, 28(14):2835–2838, 2001.

[100] M. Valeri, F. Barbara, C. Boone, S. Ceccherini, M. Gai, G. Maucher, P. Raspollini, M. Ridolfi, L. Sgheri, G. Wetzel, and N. Zoppetti. CCl_4 distribution derived from MIPAS ESA v7 data: intercomparisons, trend, and lifetime estimation. *Atmospheric Chemistry and Physics*, 17(16):10143–10162, 2017.

[101] M. Valeri, M. Carlotti, J.-M. Flaud, P. Raspollini, M. Ridolfi, and B. M. Dinelli. Phosgene in the UTLS: seasonal and latitudinal variations from MIPAS observations. *Atmospheric Measurement Techniques*, 9(9):4655–4663, 2016.

[102] C. M. Volk, J. W. Elkins, D. W. Fahey, G. S. Dutton, J. M. Gilligan, M. Loewenstein, J. R. Podolske, K. R. Chan, and M. R. Gunson. Evaluation of source gas lifetimes from stratospheric observations. *Journal of Geophysical Research: Atmospheres*, 102(D21):25543–25564, 1997.

[103] T. von Clarmann. Validation of remotely sensed profiles of atmospheric state variables: strategies and terminology. *Atmospheric Chemistry and Physics*, 6(12):4311–4320, 2006.

[104] T. von Clarmann and G. Echle. Selection of optimized microwindows for atmospheric spectroscopy. *Appl. Opt.*, 37(33):7661–7669, Nov 1998.

[105] T. von Clarmann, N. Glatthor, M. E. Koukouli, G. P. Stiller, B. Funke, U. Grabowski, M. Höpfner, S. Kellmann, A. Linden, M. Milz, T. Steck, and H. Fischer. MIPAS measurements of upper tropospheric C_2H_6 and O_3 during the southern hemispheric biomass burning season in 2003. *Atmospheric Chemistry and Physics*, 7(22):5861–5872, 2007.

[106] G. Wetzel, H. Oelhaf, G. Berthet, A. Bracher, C. Cornacchia, D. G. Feist, H. Fischer, A. Fix, M. Iarlori, A. Kleinert, A. Lengel, M. Milz, L. Mona, S. C. Müller, J. Ovarlez, G. Pappalardo, C. Piccolo, P. Raspollini, J.-B. Renard, V. Rizi, S. Rohs, C. Schiller, G. Stiller, M. Weber, and G. Zhang. Validation of MIPAS-ENVISAT H_2O operational data collected between July 2002 and March 2004. *Atmospheric Chemistry and Physics*, 13(11):5791–5811, 2013.

[107] G. Wetzel, H. Oelhaf, F. Friedl-Vallon, A. Kleinert, G. Maucher, H. Nordmeyer, and J. Orphal. Long-term intercomparison of MIPAS additional species $ClONO_2$, N_2O_5, CFC–11, and CFC–12 with MIPAS-B measurements. *Annals of Geophysics*, 56(0), 2014.

[108] G. Wetzel, H. Oelhaf, O. Kirner, F. Friedl-Vallon, R. Ruhnke, A. Ebersoldt, A. Kleinert, G. Maucher, H. Nordmeyer, and J. Orphal. Diurnal

variations of reactive chlorine and nitrogen oxides observed by MIPAS-B inside the January 2010 Arctic vortex. *Atmospheric Chemistry and Physics*, 12(14):6581–6592, 2012.

[109] S. R. Wilson, P. J. Crutzen, G. Schuster, D. W. T. Griffith, and G. Helas. Phosgene measurements in the upper troposphere and lower stratosphere. *Nature*, 334(6184):689–691, 08 1988.

[110] World Meteorological Organization (WMO). Scientific Assessment of Ozone Depletion: 1998. Geneva, Switzerland, 1999.

[111] World Meteorological Organization (WMO). Scientific Assessment of Ozone Depletion: 2010. Global Ozone Research and Monitoring Project - Report No. 52, Geneva, Switzerland, 516 pp., 2011.